

Current Induced Magnetization Dynamics in Electrodeposited Nanostructures

THÈSE N° 4687 (2010)

PRÉSENTÉE LE 7 MAI 2010

À LA FACULTÉ SCIENCES DE BASE

LABORATOIRE DE PHYSIQUE DES MATÉRIAUX NANOSTRUCTURÉS

PROGRAMME DOCTORAL EN PHYSIQUE

ÉCOLE POLYTECHNIQUE FÉDÉRALE DE LAUSANNE

POUR L'OBTENTION DU GRADE DE DOCTEUR ÈS SCIENCES

PAR

Elena MURÈ

acceptée sur proposition du jury:

Prof. O. Schneider, président du jury
Prof. J.-Ph. Ansermet, directeur de thèse
Dr G. Bertotti, rapporteur
Dr U. Ebels, rapporteur
Prof. M. Kläui, rapporteur



ÉCOLE POLYTECHNIQUE
FÉDÉRALE DE LAUSANNE

Suisse
2010

Acknowledgements

With these pages I would like to acknowledge all the people I have met during this experience in Lausanne. Thank you to those who helped me in my work and those who made my day-to-day life more pleasant.

First of all I would like to acknowledge the members of my PhD jury who had to go through the following pages: Dr Giorgio Bertotti, Dr Ursula Ebels, Prof. Mathias Kläui and the president of the jury Prof. Olivier Schneider. The PhD exam was for me the first real opportunity to present my research work in its completeness to a group of experts of the field. It was a pleasure to do this important "exercise" in front of them and to receive their feedback. Their suggestions and comments helped me focus on a few crucial points of our experimental approach and identify interesting aspects that could be developed in a future work.

Secondly, I want to thank my thesis director, Prof. Jean-Philippe Ansermet who always encouraged me and who gave me his trust, even in the difficult periods. During my thesis he was always available for discussions and help, his office door was always opened. In these four years he had to deal with all my "last minute" emergencies (e.g. the correction of this manuscript), I know that it was not easy and I extremely appreciate his patience and his kindness. Finally, I would like to thank him for his constant support related to both my work in the group and to my future steps in the world of the research.

I arrive now to the person who shared with me the joys and the pains (a lot of pains) of the experimental and theoretical work in the last three years of this PhD: Dr Nicolas Bizière. Nicolas was more than a precious help, he constituted an essential guide and our stimulating discussions (sometimes extremely "animated") were for me an inestimable source of motivation. His arrival was absolutely fundamental for me, after a first year during which someone else (someone I do not thank at all) tried to take away from me my all the enthu-

siasm and the interest in this work. Even after his departure from Lausanne a year ago, Nicolas continued to help me in the understanding of our results and giving me his feedback and suggestions for the writing of this manuscript. It was a pleasure to work with him and I am sure that I will continue to annoy him with my questions for a long time (et oui... désolée, tu ne vas pas t'en sortir facilement Nicolas!)

I want also to thank all the other members of the research group, who made the day-to-day life more pleasant. I begin with the people who welcomed me in the group: Arnaud Comment, Sami Jannin, Fiodar Kurdzesau and Aurore Rudolf. They helped me feel home since my first days in the institute and in Lausanne. A kiss to Aurore, with whom I shared the office, a lot of chocolate and almost all the nice and bad moments of these years. In the following years other people arrived in the group and they all gave a contribution to the nice atmosphere of the labs. A special acknowledgement to Simon Granville who showed an infinite patience in correcting this thesis (Simon... you really impressed me! Your help was extremely precious, thanks a lot!). I thank also Mohamed Abid for the help he gave me in these last months and for the interesting discussions and Maria Eleni Belesi whose attitude I really appreciate. I already thanked Nicolas Bizière for his help but I want to thank him again (ou pas) for teaching me a lot of "interesting" French expressions. A thought goes to Haiming who, in about one year, become a friend to all of us. His enthusiasm, his constant smile and his irony helped us (especially Aurore, our phalaenopsis and I) in keeping a nice atmosphere even in the hard days. I arrive now to the last arrived: Elisa Papa and Tatjana Hänlen. They had to deal with me during the redaction of this thesis and I know that it was not easy. Thank you for your patience and for bringing new "energies" to the lab. A particular thought to Elisa who shared the coffee with me in this last year and who helped me in playing the role of the perfect Italian stereotype.

Je remercie tous les techniciens de l'atelier mécanique, les électroniciens et informaticiens de l'Institut ainsi que le personnel administratif. Merci à Gilles Grandjean qui, en plus d'être le "grand chef" de l'atelier, a toujours su trouver le bon mot pour me faire sourire. Un grand merci à Michel Fazan et André Schläfli, mes adorables "voisins de bureau" pendant les premières années et que je vois toujours avec grand plaisir quand ils viennent nous rendre visite à l'EPFL. Un merci particulier aussi à mon nouveau voisin, Claude Amendola qui, avec sa compétence, son efficacité et son sourire, m'a toujours aidé dans le travail et a toujours apporté de la bonne humeur. Je sais que mon regard désespéré, synonyme de "Bounik en panne", va beaucoup manquer à José Grandjean qui, grâce à moi, pourrait aisément gagner une compétition de démontage-nettoyage-montage d'alimentation haute puissance Bounik AF99069 (merci beaucoup pour ta disponibilité José!). Merci à Florence Choulat et Martial Doy qui ont toujours été très gentils et disponibles quand j'ai eu besoin d'eux. Je remercie aussi toute les autres personnes qui m'ont aidé: Claire-Lise Bandelier, Philippe Cordey et

Philippe Cuanillon ainsi que Olivier Haldimann, Philippe Guex, Philippe Zürcher, Pascal Cattin et tous les autres techniciens de l'atelier mécanique, toujours gentils et souriants. Enfin un bisou à Chantal Roulin qui a toujours été disponible pour m'écouter quand j'en avais besoin. Je remercie aussi les autres membres de l'Institut IPMC (ex-IPN), surtout ceux que j'ai eu le plaisir de connaître un peu plus, comme Giulia, Anne et Luca.

Quand je pense à ces dernières années, je ne peux pas oublier les personnes rencontrées grâce à cette expérience et qui sont devenues ma "famille adoptive" ici à Lausanne. Le premier par "apparition" est Matteo qui a aussi le grand mérite de m'avoir présenté Teresa, sa femme. Ça a été un plaisir de les connaître, de les voir construire leur vie ici à Lausanne et agrandir leur famille avec le petit Leonardo (al quale mando un grande bacio). Un grand bisou à Ilaria, en elle j'ai découvert une véritable amie avec qui j'ai partagé mes pensées et les bons et mauvais moments pendant cette dernière année. Enfin une pensée pour Marco, Celine, Gaetano, Carolina et tout le groupe qui a su rendre chaque soirée passée ensemble magnifique.

Il y a beaucoup de personnes qui font aujourd'hui partie de ma vie ou qui en ont fait partie pendant ces dernières années. Je ne veux pas oublier de remercier pour son soutien celui qui a été à mes côtés pendant plusieurs années et qui m'a encouragée au début de cette thèse. Je pourrais remplir des pages et des pages pour remercier tous ceux qui m'ont apporté quelque chose en cette période. Je ne le ferai pas, car j'espère être capable de leur montrer mon affection autrement que dans les pages de ce manuscrit.

Enfin, je remercie Rémy. Grâce à lui j'ai appris qu'on a raison d'être très curieux et optimiste quand on pense à ce qui nous attend dans le futur. En très peu de temps il a fait partie intégrante de ma vie et il a su m'aider et me soutenir dans les petites comme dans les grandes choses.

Non ringrazierò i miei genitori, né per avermi sostenuta né per essere stati sempre presenti in modo discreto e rispettoso dei miei spazi. Abbiamo la fortuna di avere un rapporto che ci permette di dirci tutto quello che ci dobbiamo e vogliamo dire ad ogni occasione, non sento il bisogno di queste pagine per farlo.

Abstract

In this thesis we make use of the Spin Transfer Torque effect from a continuous microwave current to induce and study the spin dynamics of an individual sub-100 *nm* nanostructure.

The idea that an electrical current can carry a spin angular momentum was introduced in the 1980 with the advent of Spintronics. In 1996, Slonczewski and Berger predicted that, when flowing through a metal ferromagnet, such a spin polarized current can exert a torque on the magnetization. This effect is known as Spin transfer Torque (STT) and implies the possibility to manipulate the magnetization by means of an electrical current. One of the characteristics of the STT effect is that it allows for the magnetization dynamics to be excited and detected electrically. This makes the STT a perfect tool for the investigation of spin dynamics at the nano-scale. Indeed, the intrinsic local character of transport measurements permits a single nanostructure to be addressed and studied.

This thesis is devoted to the study of the STT effect induced by a microwave current (AC STT). Our experiment focuses on two main aspects: the intrinsic dynamics of the magnetization and the role of a microwave current in assisting the magnetization reversal. We perform our measurements on Co/Cu nanowires electrodeposited in nanoporous polycarbonate templates. The electrical contact to a nanostructure is realized thanks to a home-made sample-holder, without the use of any lithographic technique. In the first part of the thesis a continuous microwave current is used to both drive and probe the magnetization dynamics of a pseudo spin valve nanostructure. Our measurements show that the magnetization dynamics in such a structure is extremely complex and arises from the excitation of both magnetic layers in the pseudo spin valve. In the dynamical spectrum we identify the fundamental modes of both magnetic layers, as confirmed by macrospin simulations. Higher frequency modes are attributed to spatially non-uniform spin wave excitations, in agreement with that observed by others in arrays of nanoelements. These results validate our technique for making samples and contacting them for AC STT-induced

dynamical studies.

The second part of this work is aimed at testing the effect of AC STT on the static switching field of magnetic nanoelements. The magnetoresistive curve of a pseudo spin valve structure is recorded with and without an additional microwave current. Our results prove the effectiveness of AC STT in assisting the magnetization reversal. We measured a reduction of the switching field up to 80 mT by injecting a microwave current of about $100\text{ }\mu\text{A}$. This experiment suggests that the range of sensitivity of magnetoresistive devices could be tuned by simply injecting a continuous microwave current. This point is particularly interesting for the prospect of technological applications such as magnetic sensors.

Keywords: spin dynamics; electrically detected FMR; electrodeposition; spin transfer torque; microwave assisted switching.

Resumé

Dans cette thèse nous avons utilisé le couple de transfert de spin, généré par un courant hyperfréquence, afin d'exciter et d'étudier la dynamique de spin de nanostructures individuelles de taille inférieure à 100 nm .

L'idée qu'un courant électrique puisse être porteur d'un moment angulaire de spin a été introduite dans les années 1980 avec l'avènement de l'électronique de spin. En 1996, Slonczewski et Berger ont prédit qu'un courant polarisé en spin traversant un métal ferromagnétique exerce un couple sur l'aimantation. Cet effet, nommé Couple de Transfert de Spin (CTS), rend possible la manipulation de l'aimantation à l'aide de courant électrique. Une des conséquences du CTS est la possibilité d'exciter et de détecter électriquement la dynamique de l'aimantation. Cela fait du CTS, un outil parfait pour l'étude de la dynamique de spin à l'échelle du nanomètre. En effet, le caractère local des mesures de transport permet d'adresser une seule nanostructure à la fois.

Cette thèse a pour but d'étudier le CTS induit par un courant hyperfréquence (AC CTS). Nos expériences sont structurées sur deux axes principaux, la dynamique intrinsèque de l'aimantation et le rôle d'un courant hyperfréquence dans le retournement de l'aimantation. Nous avons effectué nos mesures sur des nanofils Co/Cu fabriqués par dépôt électrolytique dans des membranes nano-poreuse de polycarbonate. Le contact électrique est créé sans utiliser de techniques de lithographie, à l'aide d'un porte échantillon fait maison. Dans la première partie de cette thèse, un courant hyperfréquence (en mode onde continue) est employé pour manipuler et mesurer la dynamique de l'aimantation d'une nanovanne de spin. Nos mesures montrent que la dynamique de l'aimantation dans une telle structure est extrêmement complexe. Cette complexité est due, en partie, à l'excitation simultanée des couches magnétiques de la vanne de spin. Dans le spectre de la dynamique de l'aimantation, nous avons identifié les modes fondamentaux de chacune des couches ; ce qui a été confirmé par des simulations de type macrospin. Les modes à plus haute fréquence sont supposés

être liés à une excitation non uniforme (spatialement) des ondes de spin. Ceci est en accord avec les observations réalisées, dans d'autres laboratoires, sur des matrices de nanoéléments. L'ensemble de ces résultats a permis la validation de notre processus de fabrication d'échantillon et de la méthode de création de contact pour l'étude de la dynamique de l'aimantation induite par AC CTS.

La deuxième partie de ce travail a été d'étudier l'effet de l'AC CTS sur le champ magnétique statique de retournement d'aimantation de nanoéléments. L'influence d'un courant hyperfréquence sur la magnéto-résistance a été mis en évidence. Nos résultats démontrent que l'AC CTS facilite le retournement d'aimantation. En injectant un courant hyperfréquence d'environ $100\ \mu A$, nous avons réduit le champs de retournement jusqu'à 80mT. Cette expérience suggère que la pleine échelle de mesure d'un composant magnéto-résistif peut être ajustée à l'aide d'un courant hyperfréquence. Cette conclusion ouvre des perspectives d'applications industrielles pour les capteurs magnétiques.

Mots clef : Dynamique de spin, détection électrique de résonance ferromagnétique, dépôt électrolytique, retournement d'aimantation assisté par courant hyperfréquence.

Contents

Acknowledgements	i
Abstract	v
Resumé	vii
Contents	ix
1 Introduction	1
1.1 Magnetization dynamics in nanostructures	3
1.1.1 Magnetic energies and macrospin approximation	3
1.1.2 Landau-Lifshitz equation	6
1.1.3 Uniform excitations: ferromagnetic resonance	8
1.1.4 Non-uniform excitations	10
1.1.4.1 Spin waves	10
1.1.4.2 Effects of spatial confinement	12
1.1.4.3 Micromagnetic simulations in nano-elements	14
1.2 Spin dependent transport in ferromagnets	16
1.2.1 Two current model	16
1.2.2 Ferromagnet/Normal metal interface and spin accumulation	18
1.2.3 Spin transfer torque	19
1.3 Experimental evidence of spin dependent transport phenomena	21
1.3.1 Multilayered structures: Spin Valve and GMR effect	21
1.3.2 DC Spin transfer torque	23

2	Sample synthesis, contacting and characterization	27
2.1	Sample fabrication	28
2.1.1	Single bath method: calibration and quality of deposited metals . .	29
2.1.2	Electroplating extent	32
2.2	Sample contacting: SMA adapted sample-holder	33
2.2.1	High frequency characterization	33
2.2.2	Advantages and limitations	35
2.3	Co/Cu structure design and characterization	36
2.3.1	Pseudo spin valve	37
2.3.2	250 Co/Cu bilayers	41
2.4	Conclusions	43
3	Methods for current induced FMR	45
3.1	Methods for detection of the magnetization dynamics	46
3.1.1	Inductive methods for standard FMR	46
3.1.2	Spin dynamics from micro- to nano-scaled systems: a brief overview of experiments	47
3.2	Current induced FMR	48
3.2.1	FMR excitation	49
3.2.2	Electrical detection	51
3.3	Experimental set-up	54
3.3.1	V_{DC} detection of FMR	55
3.3.2	$V_{2\omega}$ detection of FMR	55
3.3.3	V_{DC}/I_{DC} detection of resonances	56
4	Current induced spin dynamics	57
4.1	Spin dynamics in PSV2: experimental results	60
4.1.1	V_{DC} signal	60
4.1.2	Peak dispersion	63
4.2	Interpretation of the spectra: nature of the excitations	66
4.2.1	Fundamental modes: macrospin simulations	67
4.2.2	Higher order spin wave eigenmodes	72
4.2.3	Role of the Oersted field	74
4.3	Further discussions	75

4.3.1	Peaks amplitude and shape	75
4.3.2	Comparison of the spectra at $H > 0$ and $H < 0$	77
4.4	Comparison of alternative detections	80
4.4.1	$V_{2\omega}$	80
4.4.2	V_{DC}/I_{DC} measurement	81
4.5	Conclusions	82
5	Switching field modulation by means of an AC current	83
5.1	State of the art and motivations	83
5.2	Experimental protocol	86
5.2.1	Role of thermal effects	87
5.3	Experimental results	89
5.3.1	PSV4 - \mathbf{H}_0 out of plane	89
5.3.2	PSV5 - \mathbf{H}_0 in plane	93
5.4	Discussion of the results	95
5.4.1	ΔH^{SW} vs f_{AC} diagram	96
5.4.2	Nature of the excitations	97
5.4.3	STT efficiency	100
5.5	Conclusions	103
6	Conclusions and future perspectives	105
	Analytical solution of the LLG modified equation under AC STT	109
	Bibliography	113
	Curriculum Vitae	xiii

Introduction

This thesis relies on electrical currents study of magnetization dynamics in a sub-100 nm nanostructure. We make use of the exchange of angular momentum between the conduction electrons and magnetization (spin transfer torque, STT) to drive magnetization switching and precession. We study the response of the magnetization to a resonant current, showing uniform oscillations and more complex spin wave dynamics. The reduced size of our devices (nanostructures down to 30 nm in diameter) and the complex spin dynamics demonstrated are two important characteristics of the experiment. The use of a microwave current to excite the magnetization precession constitutes another original element. The second part of the thesis is devoted to another aspect of current-induced spin dynamics. We move from the study of near-equilibrium dynamics such as ferromagnetic resonance (FMR) to the excitation of large angle precessions. In particular we monitor the effectiveness of a microwave current in assisting magnetization switching. All measurements presented in this thesis have been done at room temperature (T_{room}).

In this introductory section we present the motivations for our experiment. We underline the relevance of spin dependent transport and STT for both fundamental physics and technological applications and the interest in studying spin dynamics at the nano-scale.

Spin dependent transport The electronic properties of ferromagnetic materials are characterized by a dependence on spin orientation. This is at the base of a novel science called *Spintronics* which permits information to be transferred relying on both electron charge and spin. Spintronics makes a bond between electron transport and magnetic configuration giving a powerful tool for the "reading" of magnetic information. The huge impact for technological developments is evident. One of the physical mechanisms due to spin dependent transport is the possibility to "tune" a device resistance by means of a magnetic field. This phenomenon, known as magnetoresistive (MR) effect, is at the base of numerous technological applications such as magnetic storage devices [1] and novel architectures for magnetic sensors [2], fig.1.1.

Magnetization manipulation via STT The STT effect was predicted in 1996 by Slonczewski and Berger independently [3, 4]. Since then numerous theoretical works have investigated the nature of the spin momentum exchange mechanism, spin injection and spin-dependent scattering phenomena. Notwithstanding this, there are several open questions as to the role of thermal fluctuations in spin dynamics, the diffusive vs ballistic description of spin transport phenomena and the relative weight of various channels of spin relaxation. All these elements make the study of STT effects of fundamental scientific interest. To this is added the huge relevance for technological applications. The STT effect permits an electrical current to be used as the driving force of magnetization instead of magnetic fields. The lower power consumption associated with a current-driven reversal is the first attractive point from the perspective of technological applications. To this is added the technological difficulty linked to the implementation of localized magnetic fields. For all these reasons the STT effect opens up the prospect for the realization of more reliable devices for data storage [1, 5] and microwave nano-oscillator applications [6, 7].

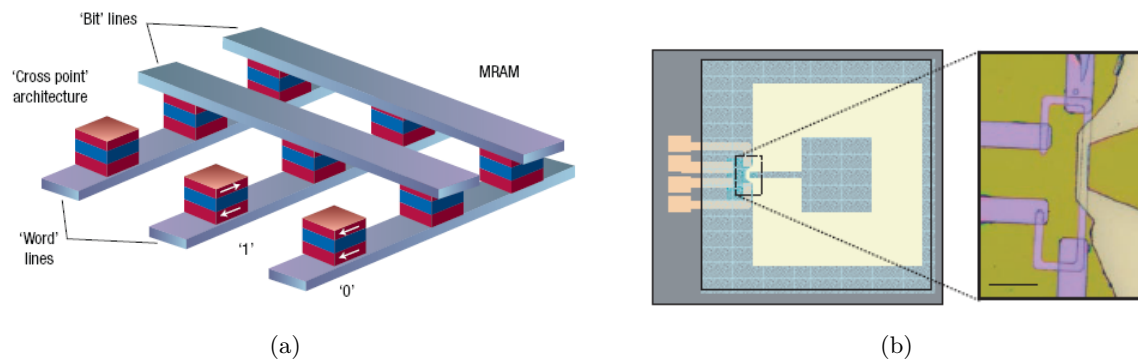


Figure 1.1 – Examples of devices exploiting the interaction between electron spins and magnetization. (a) Schematic of a magnetic random access memory (MRAM) in cross-point configuration. Information are stored in magnetic tunnel junction (MTJ) 1-bit elements. This crossed architecture permits a specific MTJ element to be addressed for local writing and reading of the information. Current pulses are injected in one channel of each line array. The magnetic field at the crossing of the two addressed lines is big enough to manipulate the MTJ magnetic configuration. The reading is performed by measuring the MTJ resistance. Image taken from reference [1]. (b) Image from optical microscopy of a mixed sensor for the detection of small magnetic fields (field applied perpendicular to the plane of the sample). The device is based on the combination of a giant MR (GMR) sensor and a superconducting loop (located above it). The zoomed image at the right is a view of the constriction area where the sensing element is located. The close view (scale bar 20 nm) shows the GMR element patterned in a yoke-like shape. The sensor allows detection of fields down to 10^{-12} T. Image taken from reference [2].

Spin dynamics in nano-sized objects Another characteristic of the STT effect is that it can constitute a local tool for the study of magnetization dynamics. It permits the investigation of dynamical phenomena (FMR and more complex spin wave magnetostatic modes) to be pushed to extremely small devices. With respect to the case of a bulk system or a thin film, the magnetization dynamics in a nano-element presents some specific points. The 3D spatial confinement, if comparable to the excitation wavelength, introduces selection rules for the spin wave wavevector and hence the onset of quantized stationary modes (sec.1.1.4.1). Moreover, in an object of reduced size, interface and edge effects are non-negligible and influence strongly the spin dynamics (e.g., the shape anisotropy implies an inhomogeneous dipolar field and becomes important in determining the frequency of magnetization eigenmodes). These aspects make the study of spin dynamics in nano-objects a hot topic for both theoretical modeling and experimental investigations, as showed by numerous recent papers [8–13]. The relevance of nano-magnets for technological applications makes the understanding of their dynamical behavior even more important (see fig.1.1). Spin dynamics plays an important role in thermal noise fluctuations, which are of central interest in devices such as magnetic memories and sensors [14, 15]. A further knowledge of non-linear phenomena such as large angle precessions and microwave assisted switching would open the prospect of future technological developments. A complete picture of linear oscillations of magnetization is at the base of the interpretation and modeling of such complex dynamical mechanisms. Presently, due to the complex inhomogeneous magnetic energy landscape of nanoelements, there is no analytical solution for this problem. However, approximated calculations [16, 17] and micromagnetic simulations [12, 18] were used to derive spin wave normal modes in several particular geometries (circular, elliptical or rectangular dots and arrays of dots).

In this chapter we review a few theoretical aspects with key roles in our experiments, notably: magnetization dynamics in confined structures (sec.1.1) and spin dependent transport in transition-metal ferromagnets (sec.1.2). We conclude with a brief section on experimental implementation of the STT effect in multilayered nanostructures 1.3.

1.1 Magnetization dynamics in nanostructures

1.1.1 Magnetic energies and macrospin approximation

When treating the magnetic properties of a ferromagnet it is convenient to define an average magnetization per unit volume. This corresponds to the average density of magnetic moment $\mathbf{M} = \langle \boldsymbol{\mu} \rangle / V_m$, with V_m volume of the magnetic sample. Any magnetic moment which

contributes to the total magnetization is coupled to other magnetic moments, external field and crystalline lattice. This happens via dipole-dipole, Zeeman, spin-spin or spin-orbit interactions. All these interactions depend on the spatial coordinates of the considered point (position with respect to other magnetic moments, to the crystalline structure etc.). It is then necessary to define a density of energy per unit volume and calculate all coupling effects locally. By integration over the whole magnetic volume we obtain the average contribution of any term to the total magnetic free energy \mathcal{F} . In particular we list here the more relevant energy contributions:

- ***Exchange energy***

This energy is a kind of spin-spin interaction, it is of quantum mechanical origin and derives from the combination of the electron-electron Coulomb interaction and the Pauli exclusion principle. It describes the coupling between electron spins (direct or indirect) which is behind magnetic order. The exchange interaction between two spins \mathbf{S}_1 and \mathbf{S}_2 can be expressed by the *Heisenberg Hamiltonian* [19]:

$$\hat{\mathcal{H}}_{1,2}^{exc} = -2 \frac{\mathcal{I}_{1,2}}{\hbar^2} \hat{\mathbf{S}}_1 \hat{\mathbf{S}}_2 \quad (1.1)$$

where $\hat{\mathbf{S}}_{1,2}$ is the *spin operator* associated with $\mathbf{S}_{1,2}$, $\mathcal{I}_{1,2}$ is the *exchange integral* and is inversely proportional to the distance between the two spins. In a ferromagnet $\mathcal{I} > 0$ therefore the exchange energy is minimized when all spins are parallel. This determines the alignment of the magnetic moment and a non-zero average magnetization. Moreover, it favors the configuration of uniform magnetization. The exchange interaction is of fundamental importance in the study of spin dynamics in magnetically ordered systems.

- ***Zeeman energy***

The Zeeman term accounts for the interaction with the external magnetic field (H_0):

$$E_Z = \int_{V_m} e_Z dV \quad (1.2)$$

$$e_Z = -\mu_0 \mathbf{M} \cdot \mathbf{H}_0$$

where \mathbf{H}_0 and \mathbf{M} represent respectively the local external field and magnetization vector on the volume element dV .

- ***Magnetostatic energy***

The magnetostatic term arises from the dipole-dipole interaction. If we define \mathbf{H}_d as the dipolar field created by all dipoles on the site of the considered magnetic moment,

we obtain:

$$E_d = \int_{V_m} e_d dV \quad (1.3)$$

$$e_d = -\frac{1}{2}\mu_0 \mathbf{M} \cdot \mathbf{H}_d$$

where the 1/2 factor is due to the fact that we are considering the energy of self-interaction and in \mathbf{H}_d we have a double count of any dipole-dipole coupling. \mathbf{H}_d depends on the system shape and is also called *demagnetizing field*. In the case of particular geometries such as a thin film or an ellipsoid the expression of \mathbf{H}_d simplifies to:

$$\mathbf{H}_d = -\overline{\overline{N}}\mathbf{M} \quad (1.4)$$

where $\overline{\overline{N}}$ is the *demagnetization tensor* which accounts for the sample shape anisotropy.

- *Magnetocrystalline energy*

This energy is due to the influence of the lattice field which deforms the electronic orbitals. The deformation of the orbitals couples with the magnetic moments through the spin-orbit interaction. It implies that a particular direction with respect to the crystal axes can be an easy axis for the magnetization. In the case of uniaxial anisotropy the magnetocrystalline energy can be written as:

$$e_k = -\frac{K_u}{M_S^2}(\mathbf{M} \cdot \mathbf{u})^2 \quad (1.5)$$

with \mathbf{u} the direction of the magnetization easy axis and K_u the constant of magnetocrystalline energy along \mathbf{u} .

The total average energy can be written as:

$$\mathcal{F} = E_Z + E_d + E_k + E_{exc} \quad (1.6)$$

Macrospin approximation If we consider the magnetization as uniform over the whole magnetic volume, each energy contribution reduces to the simple form:

$$E_i = e_i V_m$$

From the minimization of \mathcal{F} we can deduce the equilibrium direction of the average magnetization \mathbf{M} . It is equivalent to defining \mathbf{M} as a macroscopic magnetization vector which describes the magnetic configuration of the whole sample (*Macrospin approximation*). In reality it would be more appropriate to consider a spatial distribution of microscopic magnetization vectors. A way to do it is to treat the problem with finite element simulations

(*micromagnetic simulations*). In the following, both in this chapter and in the analysis of our results (chapter 4), we will treat the magnetization in the macrospin approximation. The consistency of this simplification in the different cases will be discussed.

Effective field All the listed interactions can be included in the description of magnetization equilibrium and dynamics as contributions to the global magnetic field. Each energy contribution can be associated with an *effective* field defined as:

$$\mathbf{H}_{eff}^i = -\frac{1}{\mu_0} \nabla_{\mathbf{M}} e_i \quad (1.7)$$

The sum of all these fields gives the total effective field "seen" by the magnetization \mathbf{M} :

$$\mathbf{H}_{eff} = -\frac{1}{\mu_0} \nabla_{\mathbf{M}} e_{tot} = \mathbf{H}_0 + \mathbf{H}_d - \frac{1}{\mu_0} \nabla_{\mathbf{M}} e_k - \frac{1}{\mu_0} \nabla_{\mathbf{M}} e_{exc} + \dots \quad (1.8)$$

Once again, depending on several aspects such as the crystalline and shape anisotropy of the sample, this field can be spatially uniform or strongly inhomogeneous.

1.1.2 Landau-Lifshitz equation

The magnetization dynamics in the presence of a magnetic field \mathbf{H} is described by the *Landau-Lifshitz* (LL) equation:

$$\frac{\partial \mathbf{M}(t)}{\partial t} = -\mu_0 \gamma \mathbf{M}(t) \times \mathbf{H} \quad (1.9)$$

where μ_0 is the vacuum magnetic permeability and $\gamma = 2\frac{e}{2m_e}$ is the electron gyromagnetic factor and has the value $\gamma/2\pi \simeq 28 \text{ GHz } T^{-1}$.

In analogy to the case of a single atom, the Zeeman interaction with the magnetic field resolves the spin degeneracy. The system is then able to absorb photons of energy $\Delta E_{\uparrow\downarrow} = \mu_0 |\mathbf{H}|$. In the case of an atom the Ehrenfest theorem permits us to deduce the temporal evolution of the magnetic moment $\boldsymbol{\mu} = \gamma \mathbf{S}$ associated with a single electron:

$$\frac{\partial \langle \boldsymbol{\mu} \rangle}{\partial t} = i\hbar [\mathcal{H}, \langle \boldsymbol{\mu} \rangle] = -i\hbar \mu_0 \gamma^2 [\langle \mathbf{S} \rangle \cdot \mathbf{H}, \langle \mathbf{S} \rangle] = -\mu_0 \gamma \mathbf{H} \times \langle \boldsymbol{\mu} \rangle \quad (1.10)$$

The generalization of 1.10 to the case of a bulk ferromagnet (giving equation 1.9) has been done by Landau and Lifshitz in 1935 [20]. In equation 1.9 the field \mathbf{H} is not simply the external applied field but the effective magnetic field \mathbf{H}_{eff} defined in eq.1.8. Note that in our hypothesis of uniform magnetization the exchange energy does not give any first order contribution to the LL equation. In fact the effective field deriving from e_{exc} is of the form:

$$\mathbf{H}_{exc} = \mathbf{H}_{exc0} + \mathbf{H}_{exc\sim} = \alpha \mathbf{M} + \beta \nabla^2 \mathbf{M} \quad (1.11)$$

where α and β are scalar coefficients [21]. With \mathbf{H}_{exc0} we indicate the exchange field in the case of uniform magnetization while $\mathbf{H}_{exc\sim}$ is due to the non-uniformity of \mathbf{M} . In the approximation of uniform magnetization $\mathbf{H}_{exc\sim}$ vanishes and the contribution of the exchange interaction to the LL equation is zero ($\mathbf{M} \times \mathbf{M} = 0$).

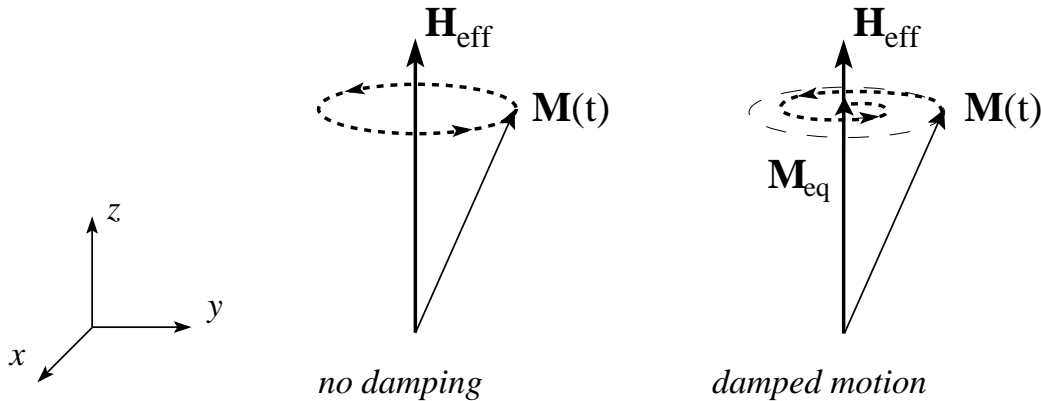


Figure 1.2 – Magnetization motion in the presence of an effective magnetic field \mathbf{H}_{eff} . The introduction of the damping term in the LLG equation determines a spiral trajectory of \mathbf{M} around \mathbf{H}_{eff} . After a certain relaxation time \mathbf{M} reaches its equilibrium position along the direction of \mathbf{H}_{eff} .

Magnetization relaxation During its precession the magnetization dissipates energy principally through the interaction with the lattice. Spins are directly coupled with surrounding ions through the spin-orbit interaction and several other mechanisms. For example, lattice vibrations modulate the distance between spins and then their coupling through the dipole-dipole interaction. Moreover, other forms of mediated interactions contribute to the magnetization relaxation, such as scattering with spin wave states (non-uniform spin excitations, see section 1.1.4.1). All these dissipative phenomena contribute to the magnetization relaxation in the direction of \mathbf{H}_{eff} . Magnetization relaxation can be included in the LL equation by adding a damping term. This term is derived phenomenologically and there is no rigorous description of it. We adopt here the *Gilbert* formulation and we describe the magnetization dynamics through the *Landau-Lifshitz-Gilbert* equation:

$$\frac{\partial \mathbf{M}}{\partial t} = -\mu_0 \gamma \mathbf{M} \times \mathbf{H}_{eff} - \underbrace{\alpha \frac{\mathbf{M}}{||\mathbf{M}||} \times \frac{\partial \mathbf{M}}{\partial t}}_{\text{damping term}} \quad (1.12)$$

where α is called the *damping coefficient*. According to the LLG equation \mathbf{M} undergoes a spiral motion around \mathbf{H}_{eff} (see fig.1.2).

1.1.3 Uniform excitations: ferromagnetic resonance

A way to excite uniform oscillation modes of the magnetization is to perturb its equilibrium by means of an oscillating magnetic field $\mathbf{h}_{rf}(t)$. The magnetization dynamics under this microwave perturbation can be described by adding an oscillating term to the LL equation 1.9:

$$\frac{\partial \mathbf{M}(t)}{\partial t} = -\mu_0 \gamma \mathbf{M}(t) \times \mathbf{H}_{eff} - \underbrace{\mu_0 \gamma \mathbf{M}(t) \times \mathbf{h}_{rf}(t)}_{\text{oscillating perturbation}} \quad (1.13)$$

It is convenient to decompose the magnetization into its static and oscillating parts, as shown in fig.1.3:

$$\mathbf{M}(t) = \mathbf{M}_{eq} + \mathbf{m}(t) = M_S \hat{z} + m_x(t) \hat{x} + m_y(t) \hat{y} \quad (1.14)$$

The magnetization response to the perturbing rf field can be written as:

$$\mathbf{m}(\omega, t) = \overline{\overline{\chi}}_{\mathbf{h}}(\omega) \mathbf{h}_{rf}(\omega, t) \quad (1.15)$$

We define in this way a magnetic susceptibility tensor $\overline{\overline{\chi}}_{\mathbf{h}}(\omega)$, called the *Polder tensor*. From the harmonic solution of equation 1.13 we can deduce the analytical expression of $\overline{\overline{\chi}}_{\mathbf{h}}(\omega)$ and the oscillation pulsation ω . We give here the expression of ω in the case of a

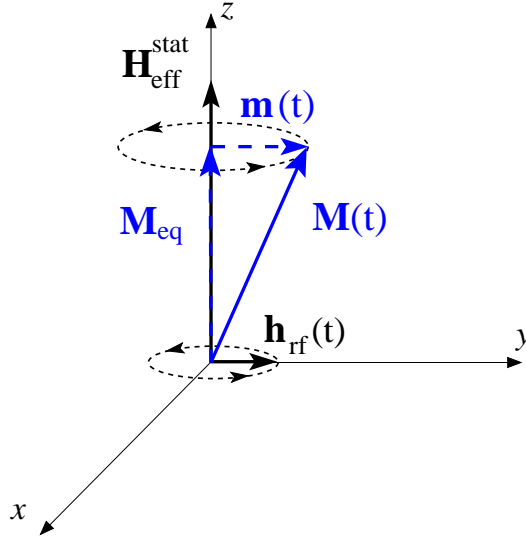


Figure 1.3 – Magnetization motion in the presence of an effective magnetic field composed of a static \mathbf{H}_{eff}^{stat} and an oscillating $\mathbf{h}_{rf}(t)$ component.

sample of ellipsoidal shape for an effective static field oriented along one of the system easy axes. We will consider the contribution of Zeeman and magnetostatic energies, neglecting any effect of crystalline anisotropy. Due to our geometric constraint, the demagnetizing

tensor is diagonal in the coordinate system O_{xyz} illustrated in fig.1.3.

$$\overline{\overline{N}} = \begin{pmatrix} N_x & 0 & 0 \\ 0 & N_y & 0 \\ 0 & 0 & N_z \end{pmatrix} \quad (1.16)$$

$$N_x + N_y + N_z = 4\pi$$

with N_i the demagnetizing factor along \hat{i} direction. The effective field is then:

$$\mathbf{H}_{eff} = \mathbf{H}_0 + \mathbf{H}_d = H_0 \hat{z} + N_x m_x(\omega) \hat{x} + N_y m_y(\omega) \hat{y} + N_z M_S \hat{z} \quad (1.17)$$

By inserting equations 1.14 and 1.17 in eq.1.13 we find:

$$\overline{\overline{\chi}}_{\mathbf{h}}(\omega) = \frac{-\mu_0 \gamma M_S}{\omega_x \omega_y - \omega^2} \begin{pmatrix} \omega_x & -i\omega \\ i\omega & \omega_y \end{pmatrix} \quad (1.18)$$

$$\omega_{x,y} = -\gamma \mu_0 M_S \left(\frac{H_0^{(z)}}{M_S} - N_z + N_{x,y} \right)$$

if we define:

$$\begin{aligned} \omega_0 &= \sqrt{\omega_x \omega_y} \\ \omega_M &= -\mu_0 \gamma M_S \\ \chi_{x,y} &= \frac{\omega_{x,y} \omega_M}{\omega_0^2 - \omega^2} \\ \mathcal{K} &= \frac{\omega \omega_M}{\omega_0^2 - \omega^2} \end{aligned} \quad (1.19)$$

we obtain the Polder tensor in its classical form:

$$\overline{\overline{\chi}}_{\mathbf{h}}(\omega) = \begin{pmatrix} \chi_x & -i\mathcal{K} \\ i\mathcal{K} & \chi_y \end{pmatrix} \quad (1.20)$$

Note that the only effect of damping on the expression of $\overline{\overline{\chi}}_{\mathbf{h}}(\omega)$ is to produce the transformation:

$$\omega_{x,y} \longrightarrow \omega_{x,y} - i\alpha\omega$$

We give now a numerical evaluation of the oscillation frequency for a nanoelement of shape and size close to one of our typical samples. We approximate our ferromagnetic layer with an ellipsoid of semi-axes:

$$a_1 = 2.5nm$$

$$b_1 = 40nm$$

$$c_1 = 45nm$$

We consider the case of \mathbf{H}_0 oriented along the shorter axis of the ellipsoid (a_1 along \hat{z} direction). The value of the demagnetizing tensor, derived from [22], is:

$$\overline{\overline{N}} = \begin{pmatrix} 0.035 & 0 & 0 \\ 0 & 0.045 & 0 \\ 0 & 0 & 0.92 \end{pmatrix} \quad (1.21)$$

For an external field of $\mu_0|\mathbf{H}_0| = 0.2T$ and $\mu_0M_S = 1.2T$ we obtain: $f = \omega_0/2\pi = 15.6GHz$.

1.1.4 Non-uniform excitations

1.1.4.1 Spin waves

In the previous subsection we treated the case of uniform spin precessions. This is appropriate when all spins contributing to the system dynamics are oscillating in phase. If we analyze the behavior of a precessing spin chain in the presence of an exchange interaction, we find that the "in phase" oscillation is only the zero eigenfunction of the *Heisenberg Hamiltonian*. Higher dynamical modes are characterized by dephased oscillations of spins. These propagating excitations, called *spin waves* (SWs), can be seen as waves traveling through the spin chain. In the case of spin precessions with wavelength larger than the distance a between adjacent spins ($\lambda \gg a$), the \mathbf{k} vector of the spin wave is approximated by [19]:

$$\omega \simeq \frac{\mathcal{I}a^2}{\hbar}k^2 \quad (1.22)$$

where \mathcal{I} is the exchange integral and ω the frequency of spin precession. We derive that $k \propto a$ hence the difference of phase $\Delta\phi$ between precessing spins increases linearly with the distance ¹, as depicted in fig.1.4.

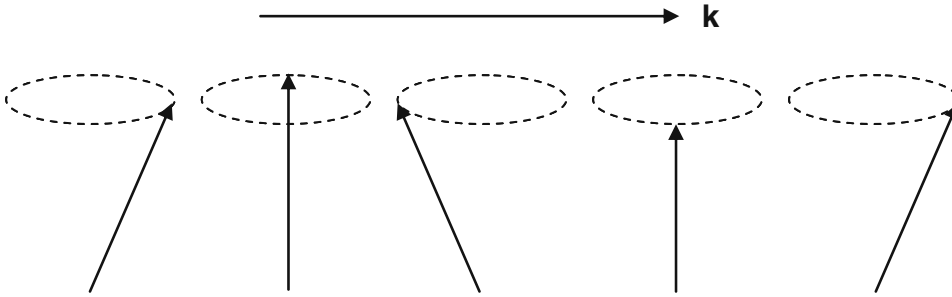


Figure 1.4 – *Spin wave: dephased precession of a unidimensional spin chain under exchange interaction between adjacent spins.*

¹With $\Delta\phi$ we indicate a difference of phase which is constant over the time and which depends only on the spatial coordinate: $\Delta\phi(\mathbf{r})$

Magnetostatic modes A magnetostatic wave is defined as the solution of the magneto-quasistatic Maxwell equations [23]:

$$\begin{aligned}\nabla \cdot \mathbf{B} &= 0 \\ \nabla \times \mathbf{H} &= 0 \\ \nabla \times \mathbf{E} &= -i\omega\mathbf{B}\end{aligned}\tag{1.23}$$

where \mathbf{H} and \mathbf{E} are respectively the magnetic and the electric field and \mathbf{B} is the magnetic induction. To this is added the constitutive equation

$$\mathbf{B} = (1 + \bar{\chi})\mathbf{H}\tag{1.24}$$

The magnetic field can be written in terms of a scalar potential ψ , defined as:

$$\mathbf{H} = -\nabla\psi$$

We consider now the case of a field \mathbf{H} oriented along the \hat{z} direction. Using the expression 1.20 of the Polder tensor we obtain that a general solution of magnetostatic Maxwell equations 1.23 satisfies [24]:

$$(1 + \chi) \left[\frac{\partial^2 \psi}{\partial x^2} + \frac{\partial^2 \psi}{\partial y^2} \right] + \frac{\partial^2 \psi}{\partial z^2} = 0\tag{1.25}$$

which is known as the *Walker equation*. We consider a plane wave $\psi \propto e^{i\mathbf{k}\cdot\mathbf{r}}$ propagating in a direction forming an angle θ_k with the axis \hat{z} . If we search for a solution of this form and we substitute the definition of χ in eq.1.25 we obtain the dispersion relation:

$$\omega = \sqrt{\omega_0 (\omega_0 + \omega_M \sin^2 \theta_k)}\tag{1.26}$$

where $\omega_0 = \sqrt{\omega_x \omega_y}$, ω_x , ω_y and ω_M are the pulsations defined in 1.19. If the dynamic magnetization in the medium is not perfectly uniform the exchange interaction enters in the expression of the Polder tensor. The term $\mathbf{H}_{exc\sim}$ in equation 1.11 is non-zero and contributes to the temporal evolution of magnetization:

$$\frac{d\mathbf{M}}{dt} = -\mu_0\gamma\mathbf{M} \times (\mathbf{H}_0 + \mathbf{H}_d + \mathbf{H}_{exc\sim})$$

It results in the transformation [23]:

$$\omega_{x,y} \longrightarrow \omega_{x,y} - \omega_M \lambda_{exc}^2 \nabla^2$$

with ω_M defined previously and $\lambda_{exc} = \sqrt{2A/(\mu_0 M_S^2)}$ the exchange length (A exchange stiffness). The dispersion relation 1.26 becomes:

$$\omega = \sqrt{(\omega_0 + \omega_M \lambda_{exc}^2 k^2) [(\omega_0 + \omega_M \lambda_{exc}^2 k^2) + \omega_M \sin^2 \theta_k]}\tag{1.27}$$

where for simplicity we assumed $\omega_x = \omega_y$ (equivalent to setting $N_x = N_y$). As $\lambda_{exc} \propto a$ we find again the proportionality $k \propto a$.

1.1.4.2 Effects of spatial confinement

The spin dynamics in confined systems is dramatically different. In a finite system it is necessary to define *boundary conditions* for the magnetization. This can determine a discrete spin wave spectrum and spatial inhomogeneities of the exchange and dipolar fields.

Effect of lateral confinement: spin wave quantization When the magnetization of the sample is tangential to the direction of the finite dimension (e.g. in plane magnetized thin film) the boundary conditions for \mathbf{M} can be defined as:

$$\left. \frac{\partial \mathbf{M}}{\partial z} \right|_{z=\pm \frac{d}{2}} = 0 \quad (1.28)$$

where \hat{z} is the direction of the confinement and d its length. If d is comparable to the wavelength of spin precession, 1.28 introduces selection rules for the SW \mathbf{k} vector and implies a quantization of the SW spectrum.

$$|\mathbf{k}_n| = \frac{n\pi}{d}$$

In fig.1.5 (a) are reported results of calculations and Brillouin light scattering (BLS) measurements of the SW spectrum in an array of wires.

Inhomogeneity of internal field The presence of a spatial boundary breaks the symmetry of the system and introduces inhomogeneity in the magnetic free energy. Surface anisotropy, especially in the case of a 2D confinement in the plane of the magnetization, is responsible for a strong non-uniformity of the magnetization distribution at the boundaries of the system. Due to magnetization inhomogeneity, the exchange field contribution to the magnetization dynamics is non-zero (see second term on right side of equation 1.11, page 6). The dipolar field cannot be expressed in the simple form 1.4 but it is necessary to introduce the tensorial Green's function of dipolar interaction ($\hat{\mathbf{G}}(\mathbf{r}, \mathbf{r}')$). The expression of \mathbf{H}_{eff} 1.8 derived in the case of uniform magnetization becomes [11]:

$$\mathbf{H}_{eff}(\mathbf{r}, t) = \mathbf{H}_0 + \underbrace{\frac{2A}{\mu_0 M_S^2} \nabla_{\mathbf{r}}^2 \mathbf{M}(\mathbf{r}, t)}_{\text{exchange contribution}} + \underbrace{4\pi \int \hat{\mathbf{G}}(\mathbf{r}, \mathbf{r}') \cdot \mathbf{M}(\mathbf{r}, t) d\mathbf{r}}_{\text{dipolar contribution}} \quad (1.29)$$

The inhomogeneity of \mathbf{H}_{eff} changes the spin wave dispersion relation and influences the dynamics of the system.

The introduction of a one dimensional confinement, as in the case of a thin film geometry, determines the first effects of SW quantification. When we pass from a thin film to a system with a 2D or 3D confinement, as in a nanowire or a nanodot, the system becomes even more complex. The definition of boundary conditions for the magnetization become more complex and it is necessary to take into account the strong inhomogeneity of the

exchange and dipolar interactions [10, 11, 17]. The internal field inhomogeneity is stronger in a nanoelement with a non-elliptical cross section (eg. a rectangular platelet with in plane magnetization or a transversally magnetized wire). In the case of samples with a magnetization pointing perpendicularly to the surface of confinement (see the scheme in the inset of fig.1.5 (b), magnetization vector aligned with the external field \mathbf{H}_e), this field inhomogeneity induces an interesting phenomenon. At the edges of the sample the magnetization undergoes a rotation to satisfy the boundary condition 1.28. The effective field, uniform at the center of the sample, drops to zero in the zone of magnetization rotation determining wells for SW (SWW) (see Ref.[11], chapter 1). It results in a *localization* of dynamical modes (edge or core modes) [25–27]. The wave vector of these modes can be approximated by:

$$|\mathbf{k}_{\text{nz}}| = \frac{n\pi}{\Delta z_n}$$

where Δz_n is the localization length of the mode n . Due to the low value of \mathbf{H}_{eff} in the wells the edge modes can be characterized by a frequency lower than that of the fundamental mode ($n=0$) (see spectrum in fig.1.5 (b)). In a recent work on STT induced spin dynamics on point contacted thin films Slavin *et al.* has shown by Brillouin light spectroscopy (BLS) how the STT effect can stabilize SWW [28].

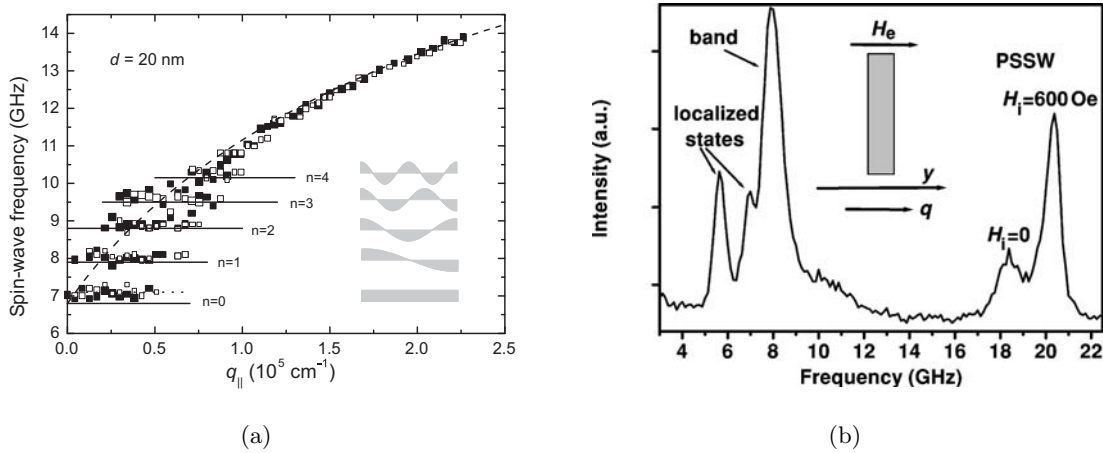


Figure 1.5 – Spin wave modes in laterally confined systems: (a) spin wave mode quantization in an array of wires (wires 20 nm thick and 1.8 μm wide, separation between wires of 0.7 μm (open symbols) and 2.2 μm (solid symbols)). q_{\parallel} indicates the wavevector perpendicular to the wire axis. The external field applied along the wire axis is 500 Oe. The solid horizontal lines indicate the results of a calculation done with quantized values of q_{\parallel} , the dashed line indicates the dispersion of spin wave continuous modes in a thin film geometry. The equivalence of open and solid symbols indicate that the distance between wires does not play any crucial role and the quantization effect derives from the finite width of the wires (after [29]). (b) spin wave mode localization or spin wave wells (SWW). BLS spectrum of spin wave modes in a transversally magnetized strip. In the spectrum arrows indicate the two low frequency modes corresponding to a spin excitation at the lateral edges of the strip (after [26])

1.1.4.3 Micromagnetic simulations in nano-elements

We report here about a few micromagnetic simulations on nanoelements of shape and size close to that of our samples which are relevant in the interpretation of our results.

Ground state of Co circular dots Buda *et al.* used finite element simulations to derive the ground state of circular Co dots, as a function of the element diameter [30]. The free energy is derived from the integration of the LLG equation including crystal, magnetostatic, exchange and Zeeman interaction. The magnetization is excited and the final state after relaxation is observed. Two different final configurations are identified: single domain uniform magnetization (SD) and flux closure state (FC-corresponding to a vortex state). The transition from the SD to FC states is due to the relative weight of the exchange and dipolar energies. In the SD state the free energy is dominated by the dipolar interaction arising from the charge imbalance at the edges of the dot. In the FC state the flux closure minimizes the demagnetizing field while the exchange energy at the vortex core is prevalent. For disk diameters approaching the vortex core size (about 30nm in Co(0001)) the exchange interaction become more important and the free energy is minimized for the SD state. The results of simulations are shown in fig.1.6.

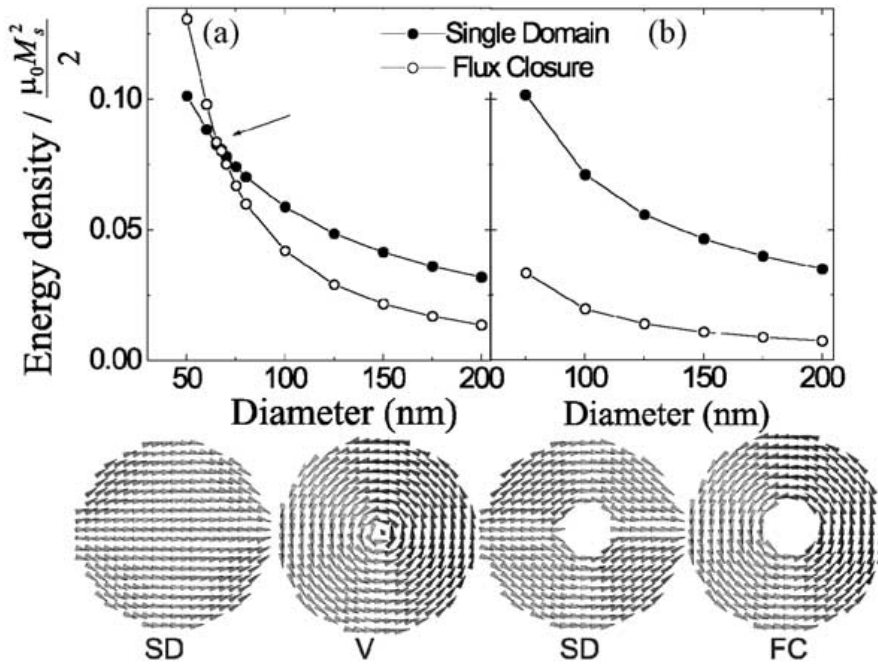


Figure 1.6 – Micromagnetic simulation of the ground state for circular Co(0001) dots (left panel) and nanorings (right panel) [30]. Plot of the free energy associated with single domain (SD) and flux closure (FC) states as a function of the dot(ring) diameter. Note that the SD state becomes the ground state for dots of diameter below 60 nm.

Dynamical modes of Py ellipses and Co cylinders McMichael *et al.* performed micromagnetic simulations of spin dynamics in non ellipsoidal nanoelements [18]. They investigated two different species, Py thin ellipses (350nm \times 160nm \times 15nm thick) with in plane magnetization and perpendicularly magnetized Co cylinders ($\varnothing=50$ nm and 5 nm thick). The magnetization dynamics is excited by field pulses of several different symmetries and its temporal evolution is registered at regular time intervals. Interesting effects evidenced by these simulations are:

Py thin ellipse: the excitation of a low frequency mode localized at the ends of the ellipse, not predicted by analytical calculations (mode in fig.1.8).

Co cylinder: the excitation of both even and odd modes in the direction parallel to the cylinder axis ((a) and (b) panel in fig.1.7).

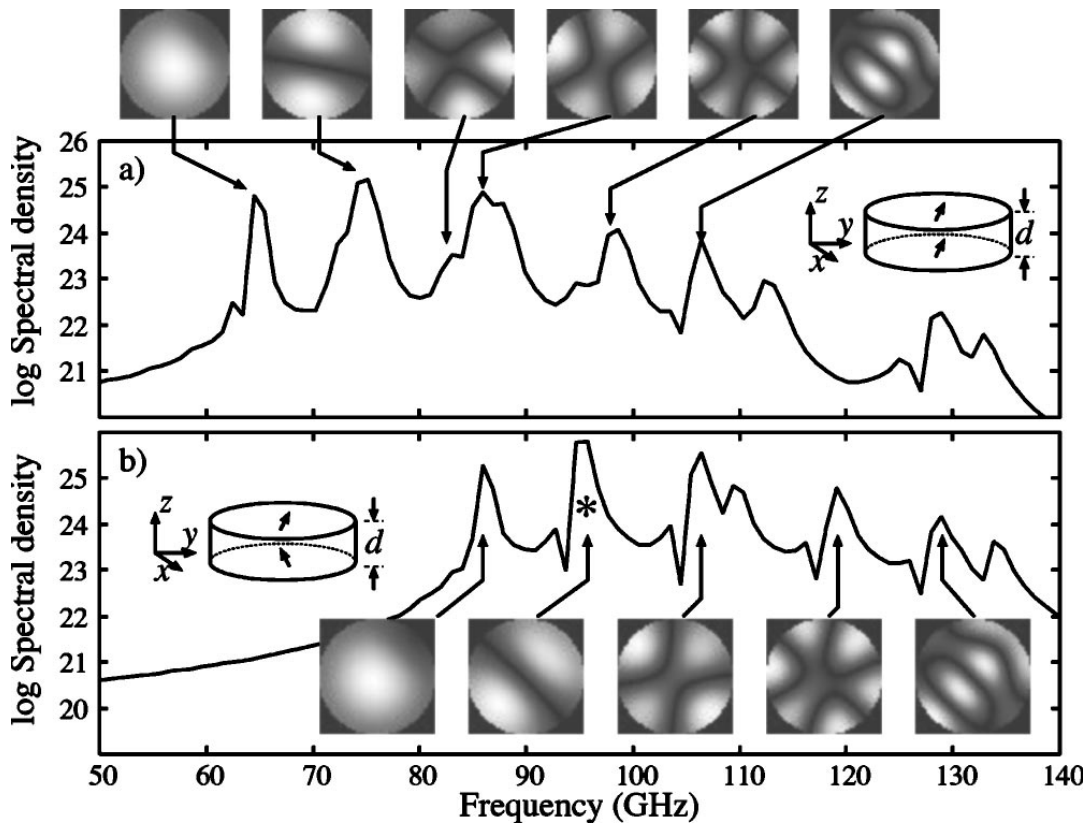


Figure 1.7 – Micromagnetic simulations of magnetization dynamics in a perpendicularly polarized Co disk ($\varnothing=50$ nm and 5 nm thick) in zero applied field. (a) and (b) panel report the spectra of modes with even and odd symmetry in the z direction (see insets in the panels) (after [18]).

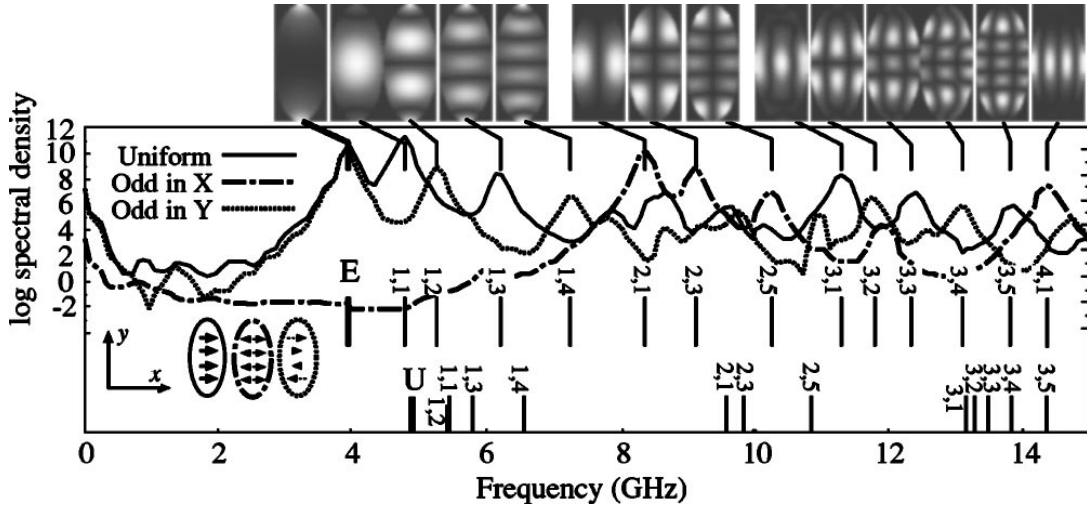


Figure 1.8 – Micromagnetic simulation of the magnetization dynamics in a thin Py ellipse ($350\text{nm} \times 160\text{nm} \times 15\text{nm}$ thick) in zero field. Note the localized mode at about 4GHz in the upper spectrum. Its frequency is considerably lower than the one simulated (second peak in the upper spectrum) and calculated (mode labeled with "U" in the spectrum at the bottom) for the uniform excitation (after [18]).

1.2 Spin dependent transport in ferromagnets

We adopt here a semiclassical description of transport phenomena in ferromagnetic materials. The spin dependent conductivity of transition ferromagnets is described by means of the *Mott two current model*. Then the case of a current flowing through a ferromagnet/normal metal (F/N) interface is treated. Finally, we review the concept of spin transfer torque and its influence on magnetization temporal evolution.

1.2.1 Two current model

This model, proposed by Mott in 1936 [31], gives a semiclassical picture of spin dependent transport in ferromagnets. It is based on two fundamental assumptions:

- **Independence of the two spin channels** The conduction is assumed to take place in two parallel channels that correspond to spin up and spin down electrons. This hypothesis is valid if we assume the time scale of spin-flip scattering to be much longer than other scattering phenomena. In that case we can neglect any spin mixing process between spin up and spin down and consider the two spin channels as decoupled.

- **Spin asymmetry in magnetic transition metals** Due to the exchange interaction the spins of unfilled bands tend to align parallel to each other, creating a *minority* and a *majority* spin orientation. This results in a net average magnetic moment and in an asymmetry of the density of states for the two spin channels ($D_{\uparrow}(E) \neq D_{\downarrow}(E)$) (see fig.1.10 (a)). An example of calculated bands for Co is given in fig.1.9 [32].

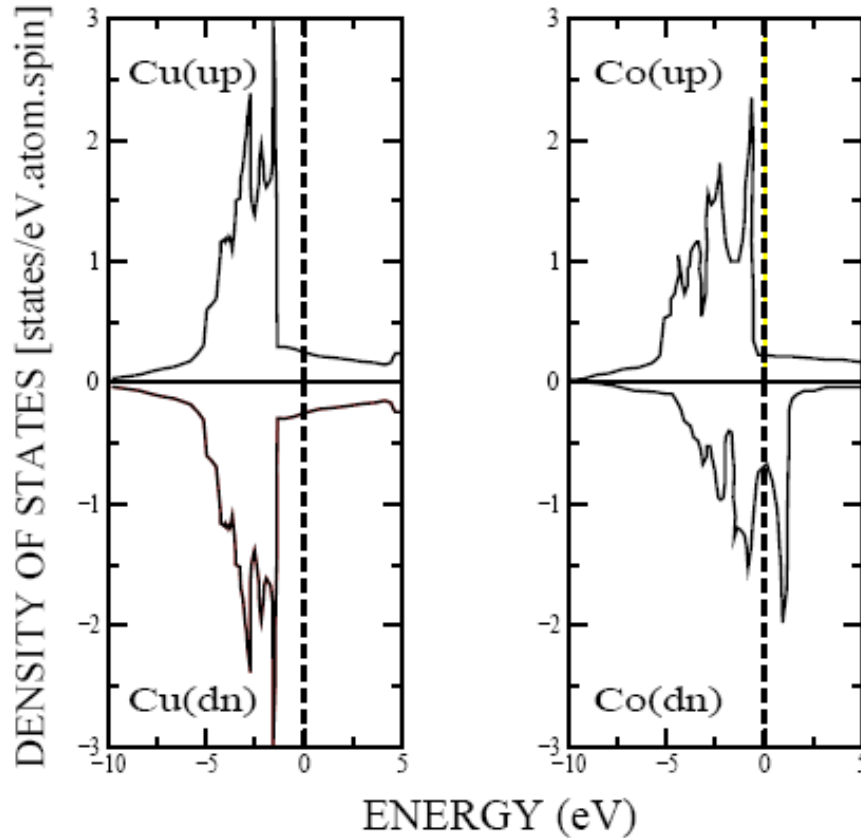


Figure 1.9 – Calculated band structure in the proximity of Fermi level for Cu and cubic Co (face centered cubic -fcc- phase) [32]. Dotted lines indicate the position of the Fermi energy E_F . Cu presents a symmetric density of states with respect to spin orientation. It implies identical transport properties for the two spin channels and a balance of up-down magnetic moments in the crystal. In the case of Co the strong asymmetry of $D(E)$ at E_F is responsible for a different scattering cross section for up and down electrons at the Fermi level. This determines the different mobility of the two species and the spin-dependent conductivity of Co. The imbalance between $D_{\uparrow}(E)$ and $D_{\downarrow}(E)$ is also responsible for a non-zero net magnetic moment. These are features typical of all transition ferromagnets (e.g. Co, Fe, Ni). Note that in Co the average density of states at E_F is quite high with respect to that of Cu or other metals, accounting for the non-optimal conductivity of transition ferromagnets.

Transition metals such as Fe, Co or Ni, due to the s-d band overlap, have an electronic structure of the $3d^{x-y} 4s^y$ kind ($x = \text{total } n^\circ \text{ of electrons in the s-d hybrid band}$). A cartoon of a typical band structure in the proximity of the Fermi level is given in fig.1.10 (a).

Both d-holes and s-electrons can contribute to charge transport and scattering processes. Because of the higher effective mass of d-holes ($m_{d\text{-holes}}^* \gg m_{s\text{-el}}^*$), the conductivity is mainly due to s-electrons.

On the other hand, the density of states of the d-bands at E_F is typically higher than that of the s-bands. It implies that the main source of scattering processes is the localization of s-electrons on unoccupied d-states. The difference between $D_{\uparrow}(E_F)$ and $D_{\downarrow}(E_F)$ determines a different scattering cross section for up and down conduction electrons ($\tau_{e\uparrow} \neq \tau_{e\downarrow}$, τ_i time of relaxation of the carrier i) and therefore a different conductivity for the two spin channels (as schematized in fig.1.10 (b)). This results in the selection of the spin channel carrying the charge current and induces a *spin polarization* of the electrical current. In the specific case of Co the region of high density of states for the *majority* spin channel lies completely below the Fermi energy (*d-like* component of the s-d hybridized band). For *minority* spins the Fermi level crosses a region of large $D(E)$ implying a higher scattering probability and a lower mobility for s-electrons parallel to this spin channel (fig.1.9, Co band structure). This determines a polarization of the current along the direction of *majority* spins, therefore parallel to the magnetization vector of the sample.

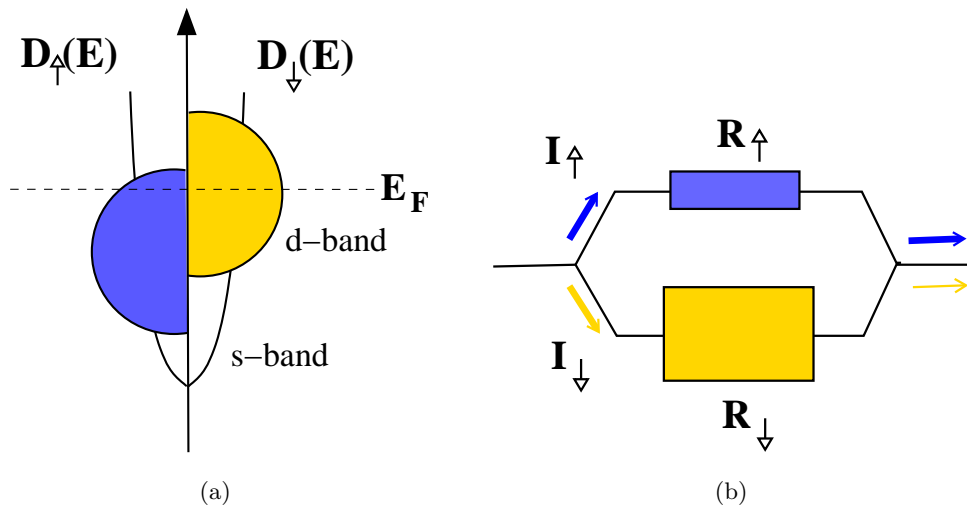


Figure 1.10 – (a) Cartoon of the density of states for the s-like and d-like components of the unfilled band in a transition ferromagnet. The imbalance between $D_{\uparrow}^d(E)$ and $D_{\downarrow}^d(E)$ determines a non-zero net magnetic moment. It is responsible as well for a spin dependent conductivity of the material. (b) Electrical circuit equivalent to the two current model description of a ferromagnet.

1.2.2 Ferromagnet/Normal metal interface and spin accumulation

In real devices we have to deal with elements of finite dimensions and boundaries between different materials. It is then relevant to analyze what happens at the interface between a ferromagnet and a normal metal (F/NM interface). If we apply a difference of potential

ΔV the current flowing from the normal metal to the ferromagnet is at the same time a charge and spin current. It results in a net injection of spins into the normal metal. In the normal metal the two spin channels have the same scattering probability and mobility (see as an example the Cu band structure in fig.1.9). It implies that *majority spins* coming from the ferromagnet accumulate at the F/NM interface. Spin-flip scattering re-equilibrates the spin channels and the current progressively loses its spin polarization. This happens on a length scale which is the *spin diffusion length* λ_{sd} . This length determines the extension of the *spin accumulation* region, as showed in fig.1.11.

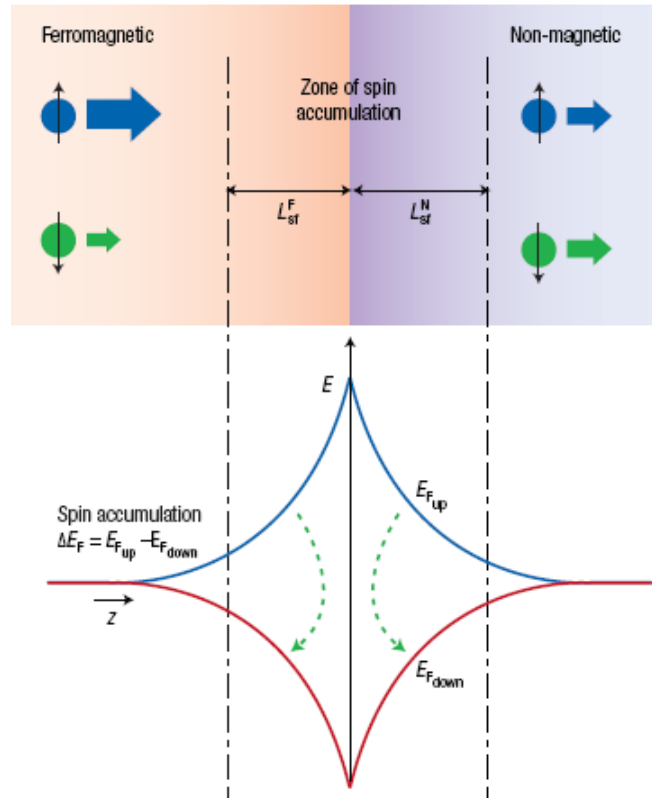


Figure 1.11 – Cartoon of the spin accumulation region at a ferromagnet/normal metal interface. At the bottom is shown the trend of the chemical potential for the two spin channels. Green dotted arrows indicate electrons passing from one channel to the other through spin-flip scattering processes (after [1]).

1.2.3 Spin transfer torque

Through the s-d scattering we have an exchange of spin angular momentum between d-electrons and conduction electrons. In transition metal ferromagnets the magnetization transfers a net momentum to s-electrons which determines the polarization of the current. On the contrary, a normal charge current cannot have any effect on d-electrons as the average angular momentum transferred by s-electrons is null. This is not true anymore when

the transport is due only to one spin channel (spin polarized current). In that case there is a well defined angular momentum associated with the current that can be transferred to d-electrons. In particular, if the spin orientation of the current is not aligned with \mathbf{M} , this momentum exchange results in a tilt of the magnetization. This torque is proportional to the current amplitude I and perpendicular to \mathbf{M} . We define:

$$\begin{aligned} \mathbf{p} & \text{ unit vector parallel to the spin polarization of } I, \\ \mathbf{m} & = \mathbf{M}/\|\mathbf{M}\|. \end{aligned}$$

We deduce the torque vector:

$$\mathbf{T}_{STT} \propto I \mathbf{m}(t) \times (\mathbf{p} \times \mathbf{m}(t))$$

This effect, called *Spin Transfer Torque* (STT), was predicted independently by Slonczewski and Berger in 1996 [3, 4].

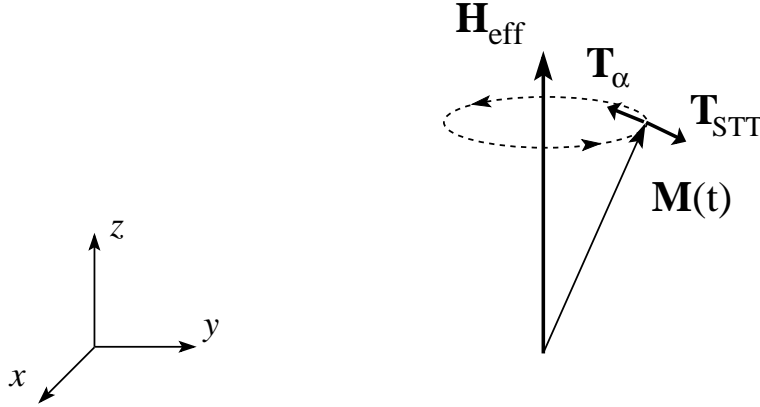


Figure 1.12 – Magnetization temporal evolution in the presence of both relaxation and the STT effect. Depending on the sign of the injected current, the STT torque \mathbf{T}_{STT} can balance the effect of the damping torque \mathbf{T}_α . In that case we assist a stable precessional state.

In order to include it in the description of magnetization dynamics, the LLG equation can be re-written in the form:

$$\frac{\partial \mathbf{m}(t)}{\partial t} = -\mu_0 \gamma \mathbf{m}(t) \times \mathbf{H}_{eff} + \alpha \mathbf{m}(t) \times \frac{\partial \mathbf{m}(t)}{\partial t} + \underbrace{\frac{\gamma \hbar}{2eV_m} \frac{\mathcal{P}}{M_s} I \mathbf{m}(t) \times (\mathbf{p} \times \mathbf{m}(t))}_{\text{Spin-Transfer term}} \quad (1.30)$$

where all terms of the LLG equation have been divided by $\|\mathbf{M}\|$ and e is the electron charge. \mathcal{P} is a dimensionless quantity called *polarization function* [3]. \mathcal{P} depends on the geometry of the device and on the relative orientation of \mathbf{M} and \mathbf{p} :

$$\begin{aligned} \mathcal{P} & = \left[(1 + P)^3 \frac{3 + \mathbf{m} \cdot \mathbf{p}}{4P^{3/2}} - 4 \right]^{-1} \\ P & = \frac{n_\uparrow - n_\downarrow}{n_\uparrow + n_\downarrow} \end{aligned} \quad (1.31)$$

where P is the *polarizing factor*. Low temperature measurements ($T = 4 K$) gave the values of $P = 0.4, 0.35, 0.23$ for Fe, Co and Ni respectively. Therefore, the polarization function \mathcal{P} has the order of magnitude of a damping coefficient ($\mathcal{P} \sim 0.1 - 0.2$). The effect of the STT can be to induce magnetization switching from one equilibrium position to another. Depending on the sign of I the STT term can oppose the damping term and, possibly, balance it. In that case it can induce a stable precession of magnetization around \mathbf{H}_{eff} (see fig.1.12). The current density necessary for the excitation of an observable effect on \mathbf{M} is estimated to be about $10^8 A \cdot cm^{-2}$.

1.3 Experimental evidence of spin dependent transport phenomena

For the experimental implementation of STT effects we need samples containing interfaces between ferromagnetic (F) and non-magnetic (NM) metals. This can be realized by the introduction of ferromagnetic grains into a non-magnetic matrix (granular samples) or by the superposition of F and NM metallic layers. The high current density needed can be achieved by reducing the cross-section of the current injection area. This can be done by the use of a point contact technique on thin film samples. Otherwise, we can reduce the cross-section of the sample itself. This can be done in several ways, e.g., patterning of thin films in pillar-shaped elements or direct deposition/evaporation in templates (nanoporous membranes or patterned substrates). All these solutions can lead to a constriction of current injection area to the order of $100 \times 100 nm^2$.

In this section we give a brief overview of experiments on the STT-effect in multilayered nanostructures. We concentrate here on the STT effect induced by a continuous current (DC STT). In chapter 3 we will introduce the STT effect induced by an oscillating current (AC STT). We will show how STT can become a useful tool for FMR studies in individual nanostructures.

1.3.1 Multilayered structures: Spin Valve and GMR effect

The simpler multilayered device we can conceive is the *spin valve* (SV). This consists of a sandwich of two ferromagnetic layers separated by a non-magnetic spacer (schematic picture in fig.1.13). One of the F layers is usually thicker than the other one (and/or pinned by antiferromagnetic coupling) and consequently less sensitive to the STT effect ($\mathbf{T}_{STT} \propto V_m^{-1}$). In order to conserve the spin information (negligible spin-flip scattering) all layers have to be thinner than the λ_{sd} in the specific material. For the following description we refer to fig.1.13. In a current perpendicular to the plane (CPP) configuration the current

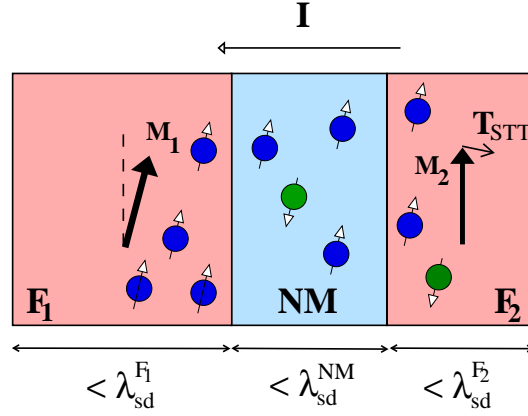


Figure 1.13 – Cartoon of a spin valve device with misaligned magnetizations. The thicker magnetic layer F_1 acts as a current polarizer, selecting the spin orientation. The non-metallic spacer is thin enough to conserve the spin information, therefore the current injected in F_2 is still spin polarized along the \mathbf{M}_1 direction. The net momentum transfer from the conducting electrons results in a torque \mathbf{T}_{STT} on the magnetization \mathbf{M}_2 . This 2D-cartoon does not consider the relaxation of the transverse spin momentum.

flowing through F_1 gets a spin polarization along \mathbf{M}_1 . The NM spacer is thin enough to conserve the spin information and when I passes through F_2 it exerts a torque on its magnetization \mathbf{M}_2 .

Giant magnetoresistance effect In this device we observe a phenomenon called the *giant magneto resistance* effect (GMR), first observed experimentally in 1988 by two different research group [33, 34]. Due to the spin dependent conductivity of the F layers the resistance of the SV depends on the relative orientation of \mathbf{M}_1 and \mathbf{M}_2 . This can be explained starting from the Mott two current model (as depicted in fig.1.14). Let us consider the case of parallel magnetizations due, for example, to the action of an external magnetic field. The majority spins of the two layers have the same orientation and this implies a higher mobility in the whole device for one of the spin channels (fig.1.14 (a)). In the case of antiparallel magnetizations (e.g., due to dipolar coupling between layers) the spin conduction channel favored in one layer encounters a higher scattering probability in the other one and vice versa (fig.1.14 (b)). This determines an average lower conductivity of the device, hence a higher resistance. The magnetoresistance of the device can be described as follows:

$$R_{GMR} = R_0 - \frac{\Delta R_{PA}}{2} \frac{\mathbf{M}_1 \cdot \mathbf{M}_2}{\|\mathbf{M}_1\| \|\mathbf{M}_2\|} \quad (1.32)$$

where a term depending on the relative orientation of the two F layers is added to the classical term R_0 . ΔR_{PA} indicates the difference of resistance between parallel and antiparallel configurations.

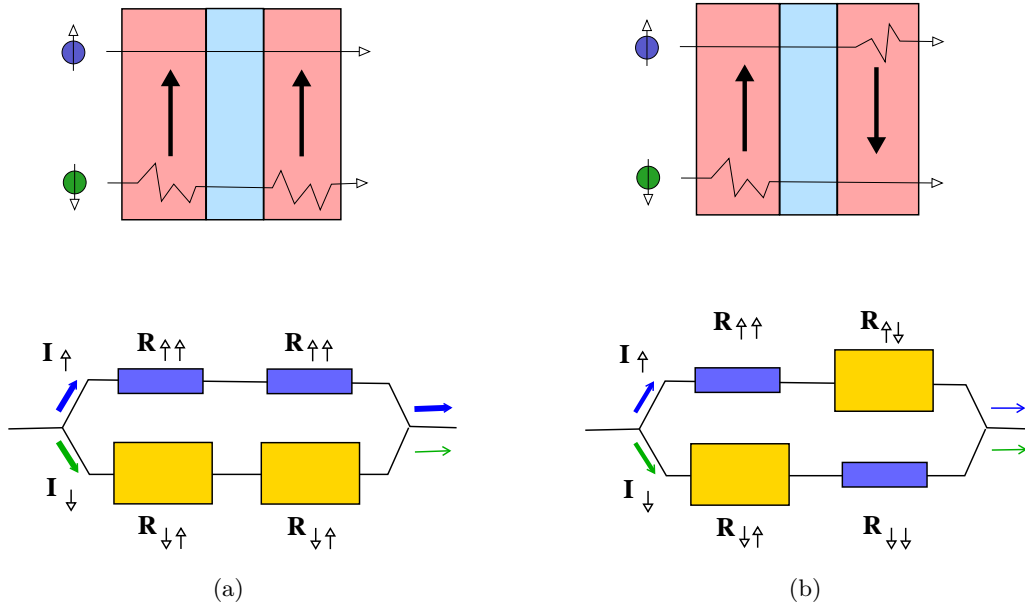


Figure 1.14 – Schematic representation of GMR effect in a SV device. (a) Parallel configuration. (b) Antiparallel configuration.

1.3.2 DC Spin transfer torque

The effect of a DC spin polarized current on the magnetization equilibrium position and dynamics has been the subject of many experimental studies. The variety of samples and geometries investigated is huge. They consist mainly of SV and magnetic tunnel junction (MTJ) structures in the shape of patterned nanopillars, electrodeposited nanowires or evaporated thin film in a point contact geometry. We give here a few examples of STT experiments on multilayered nanostructures in the current perpendicular to plane (CPP) geometry.

STT driven magnetization switching The first evidence of STT effects was given by Maxime Tsoi *et al.* in 1998 [35]. Tsoi's group studied the effect of a high density current (j_{DC} up to $10^9 A/cm^2$) on a multilayered thin film contacted in point contact geometry (contact area $\sim 10^2 nm^2$). The current was injected in the CPP configuration and all measurements were done at helium temperature (4.2 K). The magnetic configuration was monitored by measuring the DC voltage across the contact. Variations in the sample magnetoresistance were evidenced by the derivative of this voltage (dV/dI signal). The results were plotted as a function of the bias voltage across the contact and repeated for different values of an external magnetic field \mathbf{H} . The dV/dI spectra evidence magnetization switching for only one direction of the current and at critical bias values which shift with the external magnetic field (see fig.1.15).

Analogous measurements were performed by Katine *et al.* and Grollier *et al.* on patterned SV nanopillars contacted in the CPP geometry [36, 37]. The simple geometry of the samples

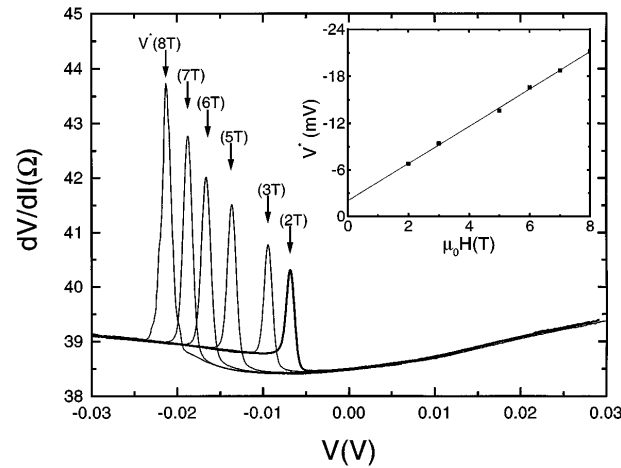


Figure 1.15 – STT-induced magnetization switching in a point contacted thin film. dV/dI spectra as a function of the bias voltage V applied across the contact. Magnetization switching is evidenced by a clear peak appearing for a certain critical voltage. Inset: dependence of the critical voltage on the external magnetic field (after [35]).

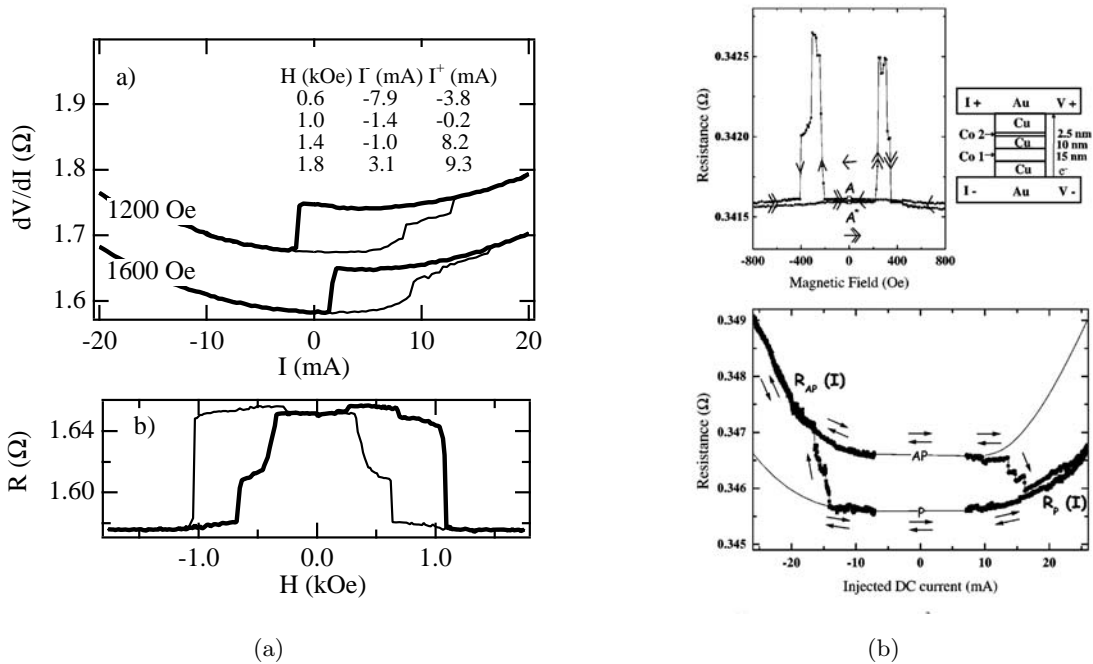


Figure 1.16 – STT-induced magnetization switching in Co/Cu SV patterned in a nanopillar shape. Results from: (a) Katine *et al.* (measurements at room temperature) [36] and (b) Grollier *et al.* ($T=30$ K) [37].

(two Co/Cu bilayers, with an additional Pt/Au pinning bilayer in the case of the Cornell group, see fig.1.16 (a) and (b)) made possible a deeper analysis of the STT effect. Both groups observed a dependence of the sign of the resistance variation on the direction of the

injected current, coherently with what is expected in the specific geometry of the sample. The inversion of ΔR with the injected current is a clear signature of the STT effect and allows a distinction to be made between the STT and field-induced switching phenomena.

STT driven magnetic dynamics The first measurements of STT-induced dynamics were realized in an indirect way. As for the detection of magnetization switching, the device resistance is used as a probe of magnetic configuration. Any change in the magnetic configuration would result in a peak in the dV/dI spectrum. The difference between peaks arising from magnetization reversal or precession can be inferred from the evolution of dV/dI spectra with the external magnetic field. Experiments concentrate on the analysis of critical currents (or bias voltage) for which peaks appear and to their field-dispersion.

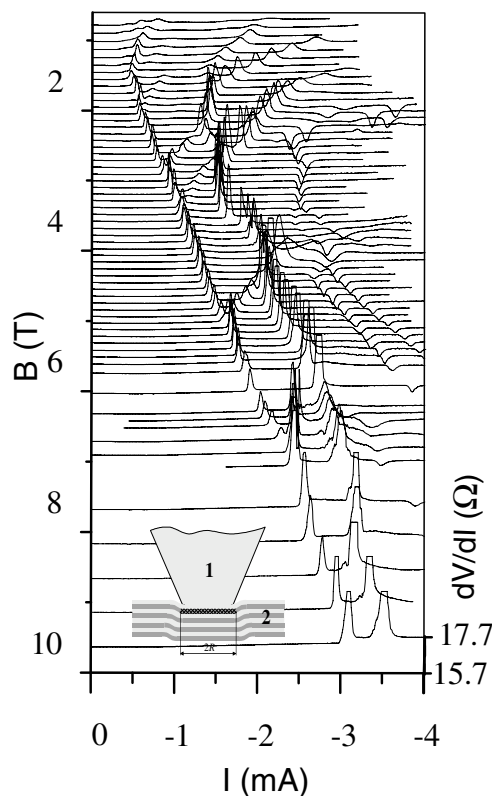


Figure 1.17 – Indirect measurements of STT-induced magnetization dynamics: $dV/dI(I)$ spectra show the "field-dispersion" of magnetization excitations. Measurements performed on Co/Cu multilayers in a point contact geometry (inset) (after [38]).

Tsoi *et al.* used this technique to evidence magnetization excitations in a thin Co/Cu multilayered film [38]; an extract of data is shown in fig.1.18 (measurements realized at helium temperature). Others realized equivalent experiments but the first direct measurements of STT-induced dynamics were due to Kisilev *et al.* in 2003 [6]. The magnetization precession was proven by recording the microwave spectrum of a SV nanopillar under a high density DC current (see fig.1.18 (a)). Measurements were performed at room temperature and the

sign of the current was fixed as positive for conduction electrons flowing from the thick to the free layer of the SV. Rippard *et al.* performed analogous measurements on multilayered thin films in a point contact geometry [39], fig.1.18 (b).

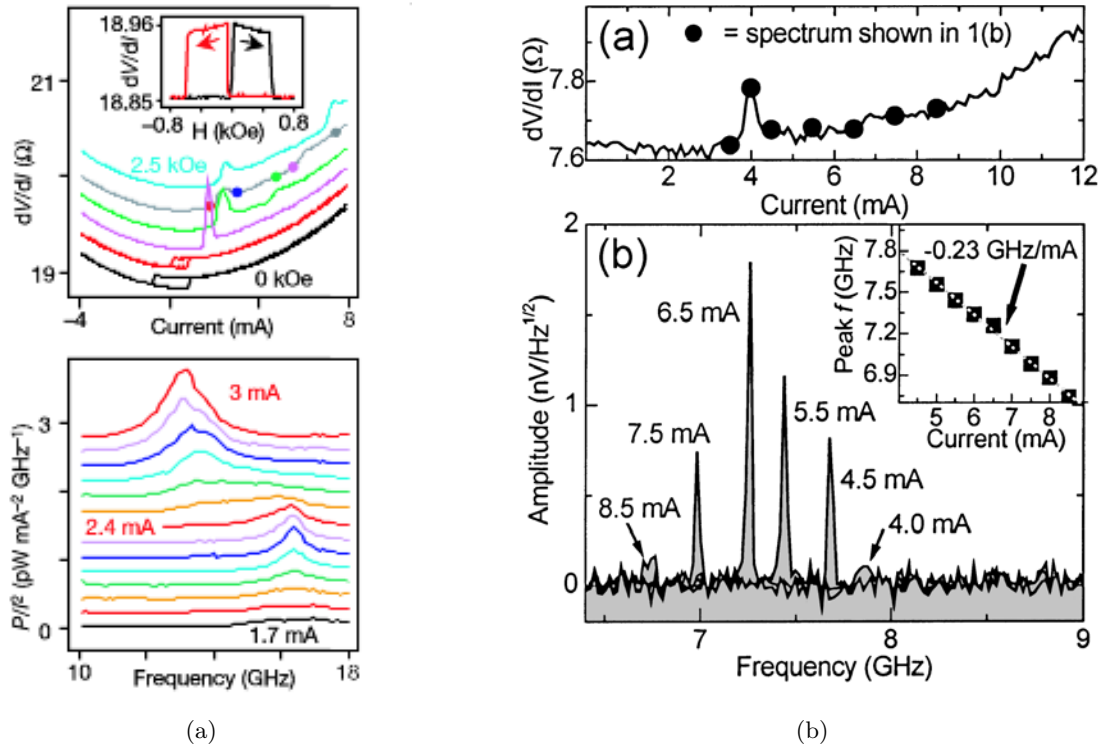


Figure 1.18 – Direct measurements of STT-induced magnetization dynamics in (a) SV patterned nanopillars [6] and (b) point contact geometry [39]. Both experiments provide evidence for spin wave excitations by recording the microwave spectrum under high DC. Measurements are repeated for several values of an external magnetic field, showing the dependence of the phenomenon on the magnetic configuration of the sample.

Sample synthesis, contacting and characterization

The current density required for STT excitation is as high as $10^7 A/cm^2$. These densities are easily attainable by using nanoscaled devices (in a sample with a cross section of the order of $100 \times 100 nm^2$ we reach the current density $j = 10^7 A/cm^2$ by the injection of a few mA). There are two main experimental solutions: to reduce the dimension of the electrical contact to the sample or to decrease the size of the sample itself. In the first category of solutions is the use of point contact geometries on evaporated films [35]. A well established technique for nanopillar fabrication is the sputtering process followed by e-beam lithography [6, 40–42]. This procedure allows high quality nanopillars to be patterned and electrically contacted in the current-perpendicular-to-plane (CPP) configuration. Nevertheless the use of ultra-high vacuum techniques and lithography makes the sample synthesis a complicated and expensive process. An alternative technique is template synthesis. Here the electrical contact is typically made by a nanoindenter [43].

For the work of this PhD thesis we used an original technique for STT experiments on multilayered nanostructures. In this chapter we describe in details our procedure for sample synthesis, contacting and characterization. We will focus on the two main steps of the sample preparation: the nanostructure fabrication (sec.2.1) and the realization of electrical contacts (sec.2.2). Co/Cu multilayered nanowires are synthesized by *in situ* electrodeposition. The electrical contact is realized thanks to a home made sample-holder, without the use of any lithography processing or the point contact technique. The suitability of the system for microwave transport measurements is verified by the high frequency characterization of the set-up. We show examples of GMR measurements on different samples (sec.2.3). The results show the effectiveness of the technique for synthesizing magnetic nanostructures with customizable thickness and number of layers. The capability of the set-up for DC STT experiments is shown in Ref. [44] by recording dV/dI spectra as a function of the DC current amplitude.

2.1 Sample fabrication

Co/Cu multilayers are grown by electrodeposition in commercial ion-track-etched polycarbonate membranes, of $6\ \mu\text{m}$ in thickness [45, 46]. These templates present sub-micron sized pores with a density of $6 \times 10^6\ \text{pores}/\text{cm}^2$ and diameters ranging from 30 to 200 nm. The electroplating is performed by the conventional three electrode method. The metal reduction occurs at a so-called *working electrode*. An inert *counter electrode* acts as the anode, allowing the ions to oxidize and balancing the charge flow into the electrolyte. A saturated Ag/AgCl electrode (*reference electrode*) permits the potential V_{Cell} of the electrochemical cell (voltage between cathode and anode) to be stabilized. The voltage is applied by an AMEL potentiostat, used to keep constant V_{Cell} and to monitor the current flowing between counter and working electrodes (I_{Cell}). In our electrochemical cell the working electrode

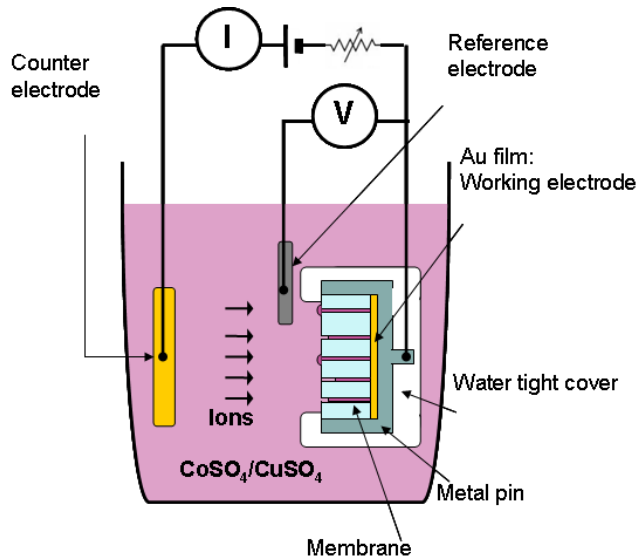


Figure 2.1 – Standard three electrode technique for electrodeposition. The gold layer sputtered at the bottom of the nanoporous membrane is used as working electrode, forcing the ions to deposit into pores. The electrodeposition is stopped as metal bumps form at the surface of the membrane

consists of a gold layer sputtered on one side of the nanoporous membrane (thickness of about $300 - 400\text{nm}$). A template disk of $1.5\ \text{mm}$ in diameter is cut and mounted on a metal pin, designed to fit a standard SMA connector. The membrane is kept in place by a teflon cup, which also protects the metal parts from the electrolyte. The metallic side of the template, in contact with the metal pin, is connected to the potentiostat. A gold electrode is used as the counter electrode. When we apply the appropriate potential ions

reduce at the metallic side of the membrane and deposit into the pores. A schematic of the experimental set-up is given in fig.2.1.

2.1.1 Single bath method: calibration and quality of deposited metals

Cu reduction can be performed at a cell voltage V_{Cu} lower than the one needed for Co deposition (V_{Co}). This permits our structures to be deposited from a single electrolyte composed of both Co and Cu sulfates. For a certain range of voltages $V_{Cu} < V_{Cell} < V_{Co}$ only the Cu reduction occurs. At $V_{Cell} > V_{Co}$ the two metals are deposited simultaneously in a percentage which depends on their concentration in the electrolytic bath. By putting an extremely small concentration of Cu into the electrolyte we can reduce the amount of Cu impurities in the electrodeposited Co [47]. For the deposition of our multilayered structures we used a bath composed of: 0.5M/l $CoSO_4$, 0.01M/l $CuSO_4$ and 0.7M/l H_3BO_3 . A cyclic voltammogram of the electrolyte yields the optimized potentials $V_{Cu} = -0.3V$ and $V_{Co} = -1.0V$ (curves not shown here). The electroplating is monitored through the current I_{Cell} flowing between counter and working electrodes. A rapid increase of I_{Cell} indicates that the ions can easily deposit on the top of the filled pores, therefore directly on the membrane surface.

Characterization of the deposited Co

Notwithstanding the small Cu concentration, the electrodeposited Co was found to contain 15% of Cu [48]. The presence of impurities in the Co layers can affect their magnetic and magnetotransport properties and influence the crystalline anisotropy. We give here some properties of the Co electrodeposited from the Co/Cu electrolyte. A superconducting quantum interference device magnetometer (SQUID) was used to measure the saturation magnetization (M_S) of a template filled from the single bath at the potential V_{Co} . The resulting $\mu_0 M_S$ of about 1 T is in good agreement with previous measurements of our group [48] (data not shown here). This value is smaller than the typical M_S of pure Co ($\mu_0 M_S^{(Co\ pure)} \simeq 1.6T$). The discrepancy can be attributed to two different factors: the lower filling rate of the pores in the template and the presence of Cu impurities. Magnetotransport measurements evidenced a maximum anisotropic magnetoresistance (AMR) of about 1.7% (fig.2.2, see sec.2.2 for details about the electrical connection of nanowires). The AMR dependence on the field orientation and its percentage corresponds to that usually observed for Co deposited from pure-metal electrolytes [49]. This proves that the presence of Cu impurities does not much affect the spin dependent properties of the deposited Co. An alternate characterization is given by nuclear magnetic resonance (NMR), performed by Aurore Rudolf. Bulk Co can present two phases: hexagonal close packed (hcp) or face centered cubic (fcc). In Co/Cu multilayers we can expect the fcc phase to be stabilized by the presence of Cu (fcc crystalline structure) [50]. Due to the different hyperfine field of

the hcp and fcc lattices, NMR permits us to discriminate between the two lattice structures. NMR spectra of Co/Cu multilayered nanowires confirmed that the electrodeposited Co crystallizes in the fcc phase [51].

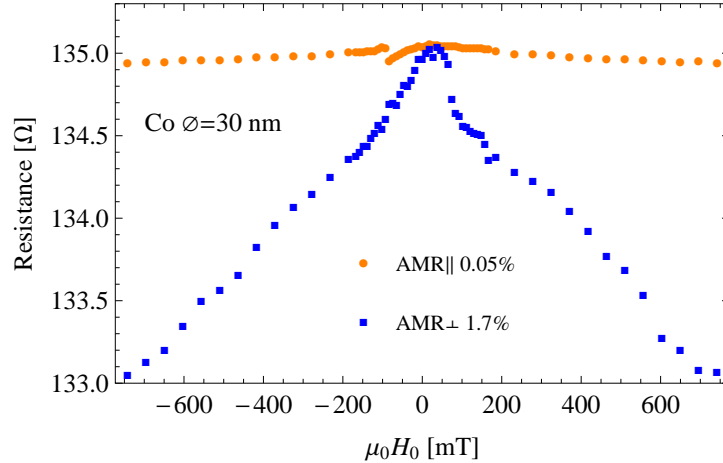


Figure 2.2 – Anisotropic magnetoresistance of electrodeposited Co. Nanowire made of $Cu_{0.5\mu m}/Co_{0.5\mu m}/Cu_{0.5\mu m}$, $\varnothing = 30\text{ nm}$. Resistance recorded with a standard lock-in technique. **Blue squares**: H_0 perpendicular to the nanowire axis. $AMR_{\perp} \sim 1.7\%$; **Orange circles**: H_0 parallel to the nanowire axis. $AMR_{\parallel} \sim 0.05\%$

Co/Cu multilayer deposition: advantages of the single bath

The deposition of alternating layers of Co and Cu can be performed by a modulation of V_{Cell} . The advantages of this method are:

- Co and Cu are deposited without extracting the template from the electrolyte. This prevents interlayer oxidation, enhancing the quality of the Co/Cu interfaces.
- The selection of the depositing metal is done remotely, without the need of any mechanical operation. This allows the layer number to be easily increased up to a few hundred, without any additional technical difficulty.

The control of layer thicknesses is done thanks to a *calibration* of the bath. Co and Cu rates of growth are determined by measuring the average time to fill the membrane at the potentials V_{Co} and V_{Cu} respectively. This constitutes only the first step of the calibration process. At $V_{Cell} = V_{Cu}$ the Co already deposited can be re-dissolved into the electrolyte. This effect is compensated for by multiplying the Co deposition time by a factor f . The determination of f constitutes the second step of the calibration. A membrane is filled with Co_{10nm}/Cu_{10nm} bilayers, using the Co rate of growth determined at the first stage of the

calibration. We expect the pores to contain, on average, 300 bilayers of this thickness. All discrepancies in the number of layers are attributed to a wrong Co calibration. The factor f is introduced and adjusted in order to reach the expected value of 300 Co/Cu bilayers. We found $f \simeq 1.8$. Due to possible changes in the bath chemical properties, this calibration procedure is repeated for each set of electrodeposited samples.

Layer shape and orientation

Electron microscopy images evidence the regular multilayered structure of Co/Cu nanowires (fig.2.3). For a layer thickness inferior to 5nm the quality of layer interfaces decreases and the structure starts to lose its periodicity.

Due to a peculiarity of the ion track-etching process, the pores are not perfectly aligned with the normal to the template. Typically the pore axis stays in a cone around the normal with an aperture angle of about $\pi/6$, as specified by the membrane manufacturer [52]. It implies that pores can have a slightly variable length. This results in a lower filling rate and constitutes an advantage for our contacting procedure (see sec.2.2). On the other hand, it introduces an uncertainty about the external field orientation with respect to the magnetic layers. Moreover, electron microscopy images show that layers can deposit at a canted angle ($< \pi/6$) with respect to the pore axis. This results in a slight ellipticity breaking the circular symmetry and introducing an easy axis for the magnetization in the plane of the layer. We will see in chapter 4 how these aspects can influence the dynamics of the system and how they have been included in our data interpretation. In fig.2.3 is an example of TEM image of a Co/Cu multilayered structure.

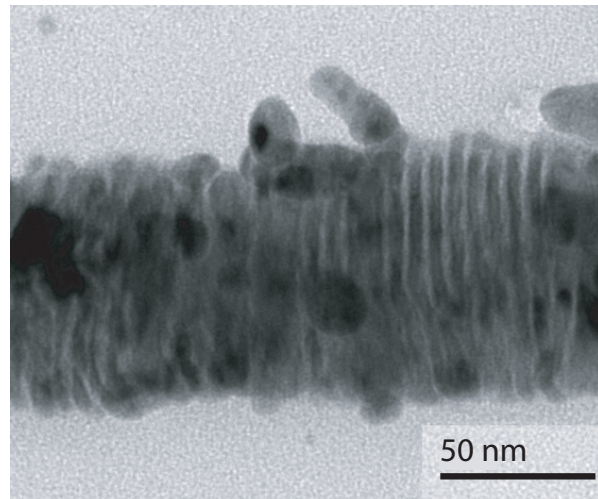


Figure 2.3 – TEM micrograph evidencing the multilayered structure of a Co/Cu nanowire deposited from a single bath. The sample has a diameter of 60nm and is made of series of Co_{5nm}/Cu_{5nm} bilayers. For layer thicknesses inferior to 5nm TEM images show that the structure periodicity is lost. Sample deposited and imaged by Aurore Rudolf [51].

2.1.2 Electroplating extent

After the pore filling the electrodeposition is continued for a few tens of seconds, in order to form micron-sized bumps on the surface of the membrane (fig.2.4 (a)). This permits us to contact a nano-sized object by working on the micron length scale, with a relatively simple procedure (see sec.2.2). The average distance between two adjacent pores is of the order of a μm (deduced from the nominal pore density). The pore separation is then comparable to the expected diameter of the metal bumps (dimensions deduced from electrical and optical microscopy, fig.2.4 (b) and 2.5). It implies that bumps grown on different nanowires could touch each other. This would result in the electrical connection of a few nanowires in parallel, while we are searching for an individual nanostructure. Then the electrodeposition extent becomes an extremely crucial point. In Fig. 2.5 (b) we show an example of an over-filled sample, in comparison with a sample suitable for our experiment (no interconnection between nanowires and Cu bumps big enough for our contacting procedure, fig. 2.5 (a)).

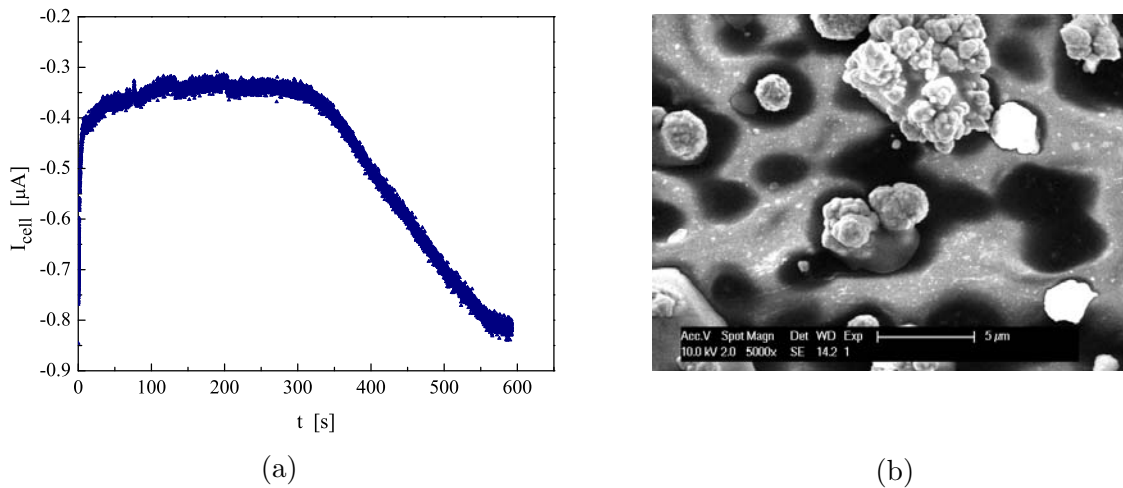


Figure 2.4 – *Electrodeposition extent: (a) example of I_{Cell} graph. The electrodeposition is stopped after a few tens of seconds from the pore fulfill (jump in the I_{Cell} curve). (b) TEM image of a filled membrane. Metal bumps are clearly visible on the template surface. Image taken by Mohamed Abid.*

Regardless of the specific multilayered structure we are depositing, we always finish the growth with Cu deposition. This prevents the presence of a magnetic element of unknown shape and anisotropy, in the form of a Co bump on the surface of the membrane.

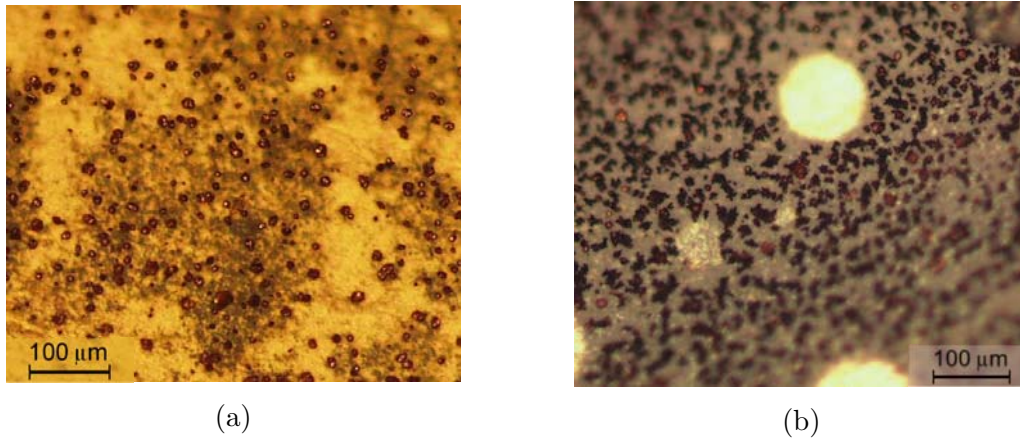


Figure 2.5 – *Top view of two examples of a filled membrane: (a) Typical aspect of a filled membrane. Nanowires end with micron-sized Cu bumps, easily visible with an optical microscope; (b) Example of a template with overgrown nanowires. Cu bumps on the membrane surface touch each other forming extended metallic islands and creating electrical connections between several nanowires.*

2.2 Sample contacting: SMA adapted sample-holder

We designed an original system for the contact of an individual nanowire, without the use of any lithographic technique. A cartoon of the sample-holder is given in fig.2.6. The filled membrane, mounted on the metal pin and held by the teflon cup, is plugged into a standard SMA female connector and sealed by a metallic cup. This cup, directly connected to the SMA ground, holds a screw with a gold wire ($25\ \mu\text{m}$ in diameter) soldered on its tip. By screwing in we approach the sample surface with the gold wire. The electrical contact is established as the wire, connected to the SMA ground, touches a metal bump on the filled membrane. The procedure is monitored by measuring the global resistance of the system. By displacing the gold wire we can approach a different area of the sample which allows us to study several nanowires in the same electrodeposited template. The fact that the membrane is sealed by a metal cup prevents any optical characterization of the contact. The quality of the electrical connection and of the magnetic structure is checked by a GMR measurement. For the magnetic characterization of samples we refer to subsection 2.3.

2.2.1 High frequency characterization

The goal of our experiment is to study magnetization dynamics in nanostructures, by means of the STT effect. Fundamental FMR modes have oscillation frequencies in the range of microwaves (see sec.1.1.3). At these frequencies the wavelength has the same scale as typical mechanical parts of a circuit. The wave propagation can be affected by absorption

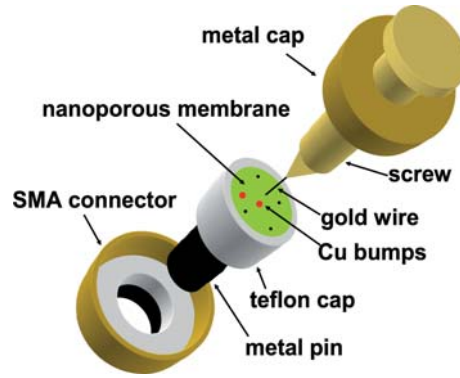


Figure 2.6 – *Cartoon of our home made sample-holder. The filled membrane is fixed on an SMA connector and its surface scanned by a micro-sized gold wire. The contacting procedure is monitored by measuring the resistance of the global system.*

and reflection, decreasing dramatically the power injected into the nanowire. The classical description of electrical circuits becomes inadequate and we have to consider the frequency dependence of each impedance element ($Z(\omega)$). A sample-holder should be designed with a global impedance well adapted for microwave signal transmission ($Z_L(\omega) \sim 50 \Omega$ for $\omega/2\pi$ in the working frequency range). This is not trivial, especially considering that our nanowire itself has a resistance ranging from 160 to 300 Ω . Impedance matching can be realized by adding inductive and/or capacitive elements to compensate the mismatch of $Z_L(\omega)$. Unfortunately our sample-holder closes any access to the sample. Moreover, its reduced dimension does not allow us to introduce any circuit element to the interior of the metal cup (internal diameter $\varnothing_{int} \simeq 2 \text{ mm}$). These considerations make standard techniques for impedance matching compensation unsuitable. The adopted experimental method allows us to avoid the microwave transmission problem at the stage of the signal detection (see sec.3.2.2). The remaining issue is the injection of microwave current into the nanostructure.

This can be partially addressed by adjusting the microwave source power. It becomes of central importance to estimate the transmittivity of the global system in the frequency range of interest. Moreover, when dealing with STT effects the current density in the nanowire has to be known. We used a simple procedure to calibrate the amplitude of I_{AC} effectively injected into a nanowire. In order to do so we relied on Joule heating. First we recorded a dV_{DC}/dI_{DC} spectrum in order to calibrate the current-induced change of resistance. We obtained a correspondence between the induced Joule heating and the current density circulating in the nanowire. Then we monitored the sample resistance with a small I_{DC} while a large I_{AC} was injected simultaneously. Data were recorded scanning the frequency f_{AC} of I_{AC} from 2 to 18 GHz, at a constant applied power delivered by the microwave source. The microwave current density was then deduced by comparing this increase in resistance to that obtained by the DC measurement. This procedure leads to an estimate of the effective I_{AC} circulating in the nanowire as a function of its frequency. Measured

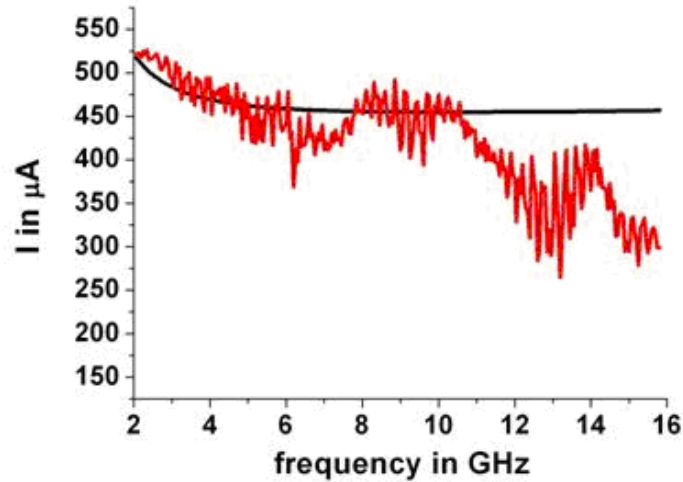


Figure 2.7 – Amplitude of the effective current injected in the device (red) and expected current calculated with the equivalent electrical circuit model (black). The circuit mismatch implies a frequency-dependent transmittivity which results in an oscillation of the injected power and in a global decrease of the current amplitude at higher frequencies.

values are presented in fig. 2.7. The signal transmission decreases with an increase in the current frequency, as predicted by a simple equivalent circuit model (black curve in fig.2.7). The system allows a high AC current density to be injected into the nanostructure, making it suitable for AC STT experiments. The remaining issue is the frequency dependence of the microwave power in the nanostructure. When needed, we compensate for this effect by adjusting the power delivered by the microwave source as a function of I_{AC} frequency. In order to do so, we again rely on Joule heating (see chapter 5 sec.5.2 on page 86).

2.2.2 Advantages and limitations

Our sample-holder permits us to contact nanowires of extremely reduced dimensions ($I = 1 \text{ mA} \implies$ current density into the wire $j \simeq 0.5 - 3.6 \cdot 10^7 \text{ A/cm}^2$, for nanowires of $\varnothing = 30 - 80 \text{ nm}$ respectively). Several different examples of nanostructures can be contacted and studied in a single electrodeposited sample (filled membrane). The setup geometry ensures the CPP configuration. All these points make our technique a good candidate for performing STT studies at the nanoscale. Its main limit is the mechanical instability. The electrical connection is ensured by mechanical contact between the gold wire and the Cu bump on the top of a nanowire. The gold wire can be easily displaced by a vibration leading to a change in the contact resistance or to the contact breaking. For an understanding of the mechanisms behind magnetization excitation a deep study of our nanostructure dynamics is necessary. In order to do so we need a nanowire to stay in place for about one or two weeks. Therefore contact stability constitutes one of the main issues of our experiment.

Another crucial point is that we want to study an individual nanostructure. The electrical connection is made by touching micron-sized metal bumps on top of the nanowires. As seen in section 2.1 such a metal bump could cover several nanowires. Moreover, the gold wire used for contacting can bend and touch several bumps. An indirect control of the number of connected nanostructures is done by checking the value of the resistance. In our group it is well established the use of another technique for in situ nanowires electrodeposition and contacting (single contact technique) is well established. A gold layer is sputtered on both sides of a polycarbonate membrane. The top layer is thin enough not to block the pores ($\sim 50\text{ nm}$ thick). The electroplating is performed as explained in section 2.1. When a nanowire reaches the membrane surface it touches the top gold layer. This metal layer is set to the potential of the working electrode and the deposition of ions into the pores stops. This technique ensures the growth and contact of an individual nanostructure [53]. Unfortunately it is not ideal for our experiment because of the high capacitance due to the two parallel sputtered gold layers. Proper adaptations of the system have permitted the transmission of a current up to 2 GHz , a frequency far below that needed in our experiments [53]. Moreover, it would allow us to study only one nanostructure for each electrodeposited sample. Nevertheless, this technique gives us an idea of the average resistance of an individual electrodeposited nanowire. Comparison with this method and the shape of GMR curve (see section 2.3) permits us to infer information about the quality of our contact.

2.3 Co/Cu structure design and characterization

Our deposition technique permits us to fabricate nanowires with customizable dimensions and magnetic structure. The layer thickness can be varied starting from a minimum value of about 5 nm (see sec.2.1.1 fig.2.3). The goal of our experiment is to manipulate the magnetization by means of a spin polarized current. In order to do so conduction electrons do not have to lose their spin information when traveling through metallic layers. Therefore the layer thickness should be below the electron *spin diffusion length* l_{sf} . As a reference we take the tabulated values of $l_{sd}^{Co} \sim 60\text{ nm}$ and $l_{sd}^{Cu} \sim 0.5\mu\text{m}$, for Co and Cu respectively. The number of layers was varied starting from two Co/Cu bilayers (spin valve-like structure) up to a few hundreds. We used two different templates having pore diameters of 30 and 80 nm. We report here about a few examples of electrodeposited samples:

- **Pseudo Spin Valve:** one $Co_{xnm}/Cu/Co_{ynm}$ unit with $x \neq y$ embedded into a Cu nanowire.
- **Cu/Co multilayers:** nanowire made of a few hundred of identical Co/Cu bilayers.

The quality of the magnetic structures and electrical contacts is verified by measuring the resistance as a function of an external magnetic field \mathbf{H}_0 . A field up to 7 kOe is produced by an electromagnet and controlled remotely. The orientation of \mathbf{H}_0 with respect to the plane of the magnetic layers is adjusted manually, by turning the sample-holder in the poles of the electromagnet. Once an electrical contact to a nanowire is established, its mechanical weakness makes the orientation of the sample a delicate procedure. For this reason it has been possible only in a few cases to characterize a nanostructure for different field orientations (see fig. 2.9 (a) and (b)). All measurements were performed in CPP configuration. The GMR was recorded with a conventional lock-in technique by injecting a current of $10\ \mu\text{A}$ at a frequency of $413\ \text{Hz}$.

2.3.1 Pseudo spin valve

The spin valve (SV) is the simplest multilayered structure suitable for STT studies. In SV devices one of the two magnetic layers is usually pinned by antiferromagnetic coupling. This simplifies the study of spin dynamics as only the magnetization of one layer is free to rotate and subjected to the STT effect. In our SV-like structures there is no pinning. We imitate the SV-behavior by making one Co layer (l_{Tk}) considerably thicker than the other one (l_{th}). Typically l_{Tk} is between 4 and 8 times thicker than l_{th} . Because of the inverse dependence of STT on the magnetic volume (see page 51 the coefficient β in eq.3.4), the magnetization of the thick Co layer is supposed to be less affected by STT. In the following we will refer to these structures as pseudo spin valves (PSVs).

We report here three examples of PSVs structures:

- PSV1: $\varnothing = 80\ \text{nm}$ $\text{Co}_{40\text{nm}}/\text{Cu}_{7\text{nm}}/\text{Co}_{5\text{nm}}$, \mathbf{H}_0 at an angle $\theta_H \sim 30^\circ$ with respect to the plane of layers.
- PSV2: $\varnothing = 30\ \text{nm}$ $\text{Co}_{20\text{nm}}/\text{Cu}_{5\text{nm}}/\text{Co}_{5\text{nm}}$, \mathbf{H}_0 approximately in-plane ($\theta_H \sim -20^\circ$) and out-of-plane $\theta_H \sim 122^\circ$ with respect to the Co layers ¹.
- PSV3: $\varnothing = 30\ \text{nm}$ $\text{Co}_{20\text{nm}}/\text{Cu}_{5\text{nm}}/\text{Co}_{5\text{nm}}$, \mathbf{H}_0 approximately in the plane of Co layers.

PSV1 and PSV2 are two samples measured in the frame of FMR studies (see chapter 4). The sample PSV3 has the same structure as PSV2 and was chosen to show the variety of behaviors observable for the same magnetic structure. GMR curves of the samples are shown in fig.2.8, 2.9 and 2.10. H_0 corresponds to the field value projected onto the direction $\hat{H}_0 = \mathbf{H}_0/|\mathbf{H}_0|$. We indicate with H_1^{SW} and H_2^{SW} the value of H_0 corresponding to the first and second GMR jumps respectively. Our assumptions about the field orientation are

¹The geometry of our samples induces a possible misalignment of the field from the real "in-plane" and "out-of-plane" configurations. The effective orientation of \mathbf{H}_0 is deduced from macrospin simulations (see chapter 4 sec.4.2.1)

supported by macrospin simulations, not shown here (see chapter 4 sec.4.2.1 on page 67 for details about the simulations). The field H_0 is swept from negative to positive values first (R_{up} , blue circles) and then back to negative saturation (R_{down} , purple squares). In the analysis of the GMR curve we can distinguish three regions. Depending on the value of H_0 with respect to H_1^{SW} and H_2^{SW} , we have:

Zone I Nearly saturated regime: $|H_0| > H_{1,2}^{SW}$, the magnetizations of the two Co layers are almost aligned with \mathbf{H}_0 and the resistance attains its minimum value R_P . In this region the magnetization in the layer can be considered as almost uniform, due to the effect of the strong external field;

Zone II Transient regime: $|H_0| \sim H_{1,2}^{SW}$ is the zone of stronger variation of the magnetoresistance and hence of the magnetic configuration. The larger this area the more gradual the magnetization switching;

Zone III Dipolar regime: $H_1^{SW} < H_0 < H_2^{SW}$. In this zone dipolar and exchange energy dominate on the uniform external field and could imply an inhomogeneous magnetization distribution. The magnetic energy is minimized by the antiparallel alignment of the magnetizations of the two layers. The resistance reaches here its higher value ($R = R_{AP}$).

The attribution of net boundaries between this zones is only an indication but it is still of help in the analysis of the magnetic configuration. We have to notice that the main contribution to the resistance is given by the Cu nanowire, which does not have any effect on the magnetoresistive signal. In order to compare the GMR percentage to that of standard Co/Cu SV nanopillars the value has to be re-scaled. The GMR of 250 Co/Cu multilayers is a better indicator of the transport properties of our electrodeposited samples. In the following discussions the magnetizations of the thick and the thin Co layers are indicated with \mathbf{M}_{Thick} and \mathbf{M}_{thin} respectively.

PSV1 The GMR of the sample is shown in fig.2.8. The average resistance is about 219Ω . This corresponds to what is expected for an electrodeposited Cu nanowire with $\varnothing = 80nm$. The GMR curve, fig.2.8, shows that the first layer switches before H_0 inverses its sign, which is an indication of dipolar coupling between layers. We assume this jump is due to the switching of the thin layer, driven by the dipolar coupling with the thick layer. The GMR is slightly asymmetric, with $|H_1^{SW}| < |H_2^{SW}|$. The maximum ΔR is 0.5Ω which corresponds to a GMR $\simeq 0.2\%$. We have to consider that the PSV volume is less than 1/100th that of the whole nanowire. It is reasonable to associate to the PSV an average resistance of 2.19Ω . The *equivalent* GMR percentage is of about 23%. In the following we will refer to the R_{up} curve (blue circles in fig.2.8).

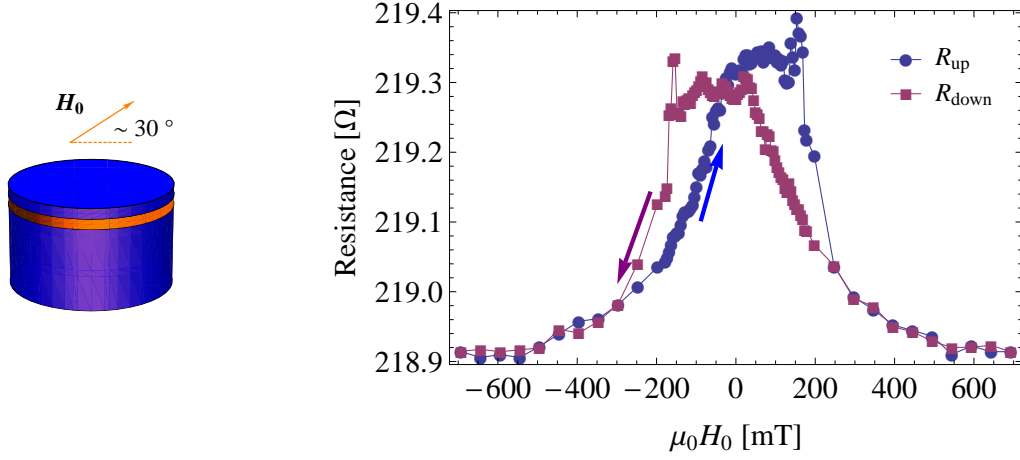


Figure 2.8 – PSV1: GMR curve recorded with \mathbf{H}_0 forming an angle $\alpha \sim 30^\circ$ with the plane of layers. **On the left:** cartoon of the sample structure and field configuration. **On the right:** GMR curve recorded with a standard lock-in technique. H_0 is swept from negative to positive values (blue circles) and back to negative saturation (purple squares).

Zone I corresponds to $|\mu_0 H_0| > 500mT$. Zone II is located at $-500 < \mu_0 H_0 < -50mT$ and $150 < \mu_0 H_0 < 500mT$. Its large extent indicates that the magnetization switches gradually. The zone of antiparallel alignment (Zone III) corresponds to the GMR plateau at $-50 < \mu_0 H_0 < 150mT$. We observe a positive peak of resistance at the end of the plateau. This could arise from the competition of \mathbf{H}_0 with the dipolar coupling between layers. When H_0 exceeds the thick layer coercive field \mathbf{M}_{Thick} rotates. As a consequence the resistance start to decrease. Simultaneously the dipolar field on \mathbf{M}_{thin} changes. The magnetic energy in the thin layer varies and forces the magnetization to switch, restoring the antiparallel alignment. At $H_0 > H_2^{SW}$ the field is big enough to overcome the dipolar coupling and set \mathbf{M}_{thin} parallel to \mathbf{M}_{Thick} . This picture is supported by the results of macrospin simulations (for details about the simulations see chapter 4). However, the agreement of our simulations is only qualitative and a more complex model is required to reproduce the exact GMR shape. Indeed, there are several elements that we do not consider in our model, such as magnetocrystalline anisotropy and possible defects in the crystalline structure and in the layer shape.

PSV2 The GMR of the sample recorded for \mathbf{H}_0 in-plane and out-of-plane are shown in fig.2.9 (a) and (c) respectively. The average resistance is about $R_0 = 136\Omega$. This value is inferior to that expected for an individual nanowire with $\varnothing = 30nm$ and closer to that of two nanowires connected in parallel. The maximum ΔR is of 0.7Ω , which gives a GMR

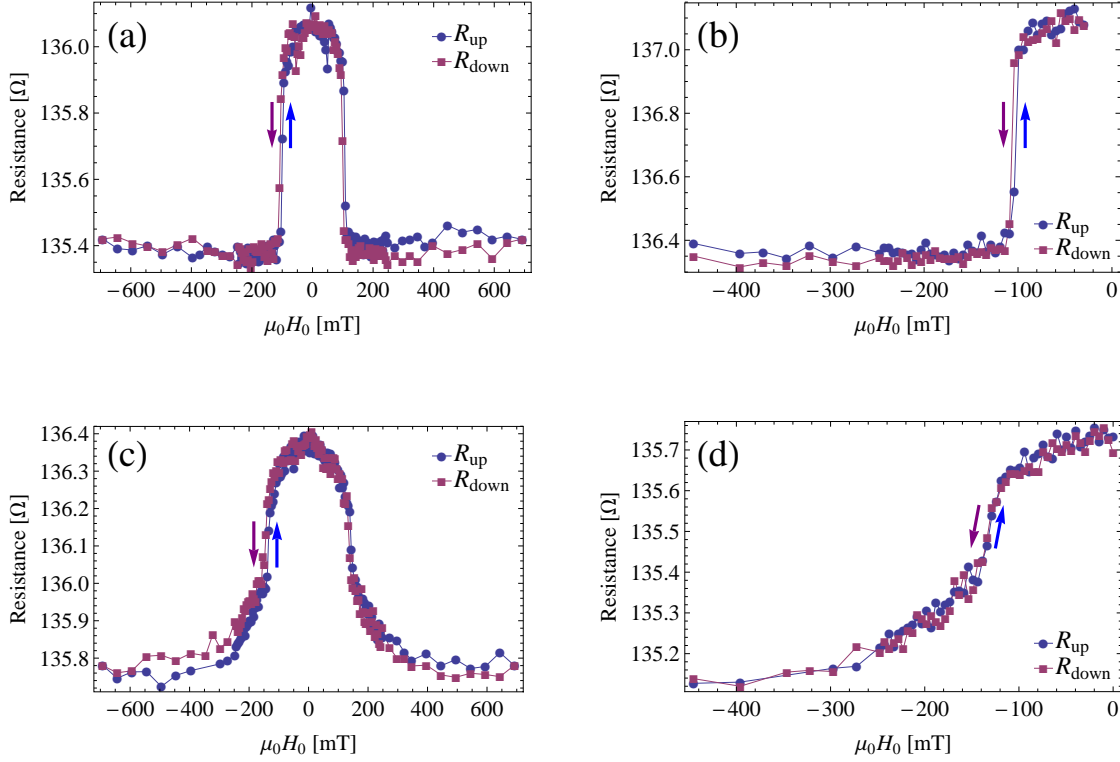


Figure 2.9 – PSV2 GMR curves. H_0 swept from negative to positive values (blue circles) and back to negative saturation (purple squares). Field in-plane: complete GMR (a) and minor loop (b). Field out-of-plane: complete GMR (c) and minor loop (d).

of about 0.5%. Due to the unusual low resistance of this sample we do not judge the value of the equivalent GMR to be significant. As for PSV1, the dipolar coupling between layers causes the switching of one magnetic layer before field inversion occurs ($H_1^{SW} < 0$). The GMR is symmetric and centered at zero field for both \mathbf{H}_0 configurations. We will indicate fields H_1^{SW} and H_2^{SW} with the general term H^{SW} . For H_0 in plane the passage from the antiparallel to the parallel alignment of layers is extremely abrupt (switching field: $\mu_0 H_{\parallel}^{SW} = 100 \text{ mT}$). This is an indication that, notwithstanding the low average resistance of this contact, we are probably measuring a single nanostructure. In fact, electrodeposited layers present a broad distribution of switching fields [54]. It is extremely improbable that two identical magnetic layers have exactly the same coercive field. Therefore, we interpret abrupt jumps in the GMR to the switching of a single layer. The absence of intermediate steps between R_P and R_{AP} suggest the presence of only two magnetic layers, indicating that we are measuring a single nanostructure. **Zone III** presents similar features to those of PSV1. On the resistance plateau we identify a narrow dip at $\mu_0 H_0 = 50 \text{ mT}$ and a

subsequent increase of resistance (back to the full R_{AP} value). As in the sample PSV1 we explain this feature due to competition between the dipolar and external fields on the thin layer magnetization.

In the out of plane configuration the passage from parallel R_P to antiparallel R_{AP} alignment is smooth. Here **zone II** covers a large interval of fields and it is difficult to attribute a precise value to the switching field ($150\text{ mT} < \mu_0 H_{\perp}^{SW} < 250\text{ mT}$). It indicates that magnetization undergoes an almost coherent rotation.

We observe that the discrepancy between $H_{\parallel}^{SW}/H_{\perp}^{SW}$ and the abrupt/coherent switching are typical features of in-plane and out-of-plane configurations. Indeed, in the out-of-plane configuration the strong in plane anisotropy of the thin layer contrasts with the effect of the external field and we expect a higher switching field for \mathbf{M}_{thin} . Finally we observe that the minor loops in both in-plane and out-of-plane configurations does not present an hysteretic behavior (see fig.2.9 (c) and (d)). This indicates that the reversal of the magnetization is reversible.

PSV3 This sample was electrodeposited with the same protocol as PSV2 and it should present the same magnetic structure. In fig.2.10 (a) and (b) we show the complete and minor loops of GMR recorder for \mathbf{H}_0 out-of-plane. The average resistance of the sample is about $132\ \Omega$. $\Delta R_{Max} \simeq 0.7\ \Omega$, which corresponds to a GMR of about 0.6%. All these values are in good agreement with that observed for PSV2. On the contrary, the GMR shape is completely different and strongly asymmetric (fig.2.10 (a)). Moreover, the minor GMR loop is strongly hysteretic. In the R_{up} curve we identify two abrupt jumps at $\mu_0 H_1^{SW} = -60\text{ mT}$ and $\mu_0 H_2^{SW} = 120\text{ mT}$. The field geometry and the stronger dipolar coupling acting on the thin layer indicate that this layer should switch first. Therefore we associate the thin layer to H_1^{SW} and the thick layer to H_2^{SW} . The discrepancy of behavior between PSV2 and PSV3 shows that the interpretation of GMR curves is far from trivial. Numerous unknown parameters such as the exact field orientation, layer shape and crystalline anisotropy can make a significant difference between the two samples. The uncertainty about these elements constitutes the main limitation of our synthesis technique.

2.3.2 250 Co/Cu bilayers

GMR is recorded for \mathbf{H}_0 applied in the plane of layers. The resulting GMR curve is shown in fig.2.11. It presents a characteristic *bell shape* and a total GMR percentage of about 17%. This value is very good if compared with the typical GMR of Co/Cu nanowires or patterned nanopillars [36]. This proves good magnetotransport properties of electrodeposited Co/Cu bilayers. The acquisition is repeated for different field orientations and GMR always presents a bell shape (data not shown here). The nanowires are made of

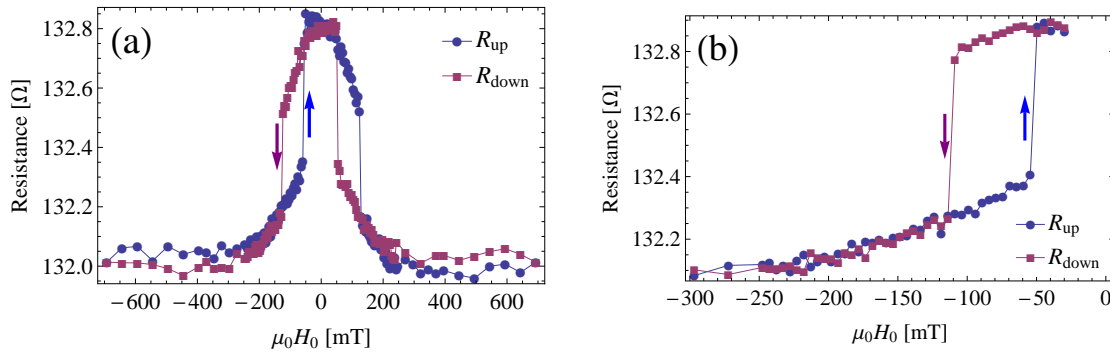


Figure 2.10 – *PSV3 Complete GMR (a) and minor loop (b). Curves recorded with H_0 applied in the plane of the magnetic layers. H_0 swept from negative to positive values (blue circles) and back to negative saturation (purple squares).*

hundreds of Co layers. It implies a range of possible magnetic configurations, corresponding to intermediate values of the resistance. The broad distribution of switching fields of the layers [54] determines the characteristic bell shape. The first Co layers reverse at $H_0 \simeq 400$ mT and, due to the progressive switching of the other layers, the resistance keeps increasing until $H_0 = 0$. This generates the characteristic bell shape observed in the GMR curves.

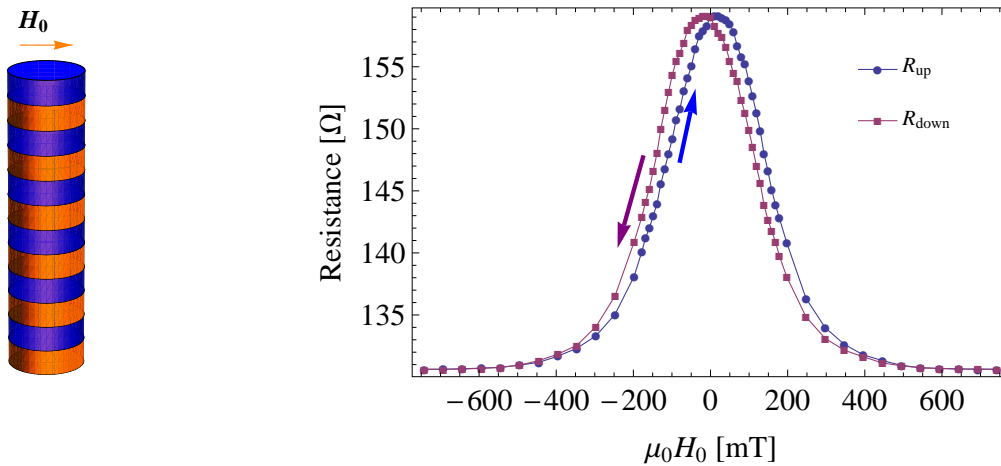


Figure 2.11 – *250 bilayers of Co_{10nm}/Cu_{10nm} . On the left: schematic picture of the magnetic structure. On the right: magnetoresistive curve for a magnetic field applied in the plane of Co/Cu bilayers. H_0 swept from negative to positive values (blue circles) and back to negative saturation (purple squares).*

2.4 Conclusions

Template synthesis in commercial materials is used to grow sub-100 nm multilayered nanostructures. The electrical contact to a nanowire is established with a home-made sample holder, without the use of any lithographic process. The system permits measurements of an individual nanowire of extremely reduced dimensions (diameters down to 30 nm). Moreover, it gives the possibility to contact and study several examples of nanostructures in the same template. All these characteristics make our technique low cost and flexible. Moreover, electroplating permits us to control quite easily several parameters of deposited magnetic structures. This was stressed by showing a few examples of multilayered nanowires (different diameters, layer number and thicknesses). The quality of deposited structures is verified by characterization of the Co properties and magneto-transport measurements. We observe GMR percentages of about 20 – 25% in PSVs (equivalent GMR) and 14 – 18% in multilayers. These values are comparable with those observed elsewhere on Co/Cu nanopillars realized by sputtering and patterned by lithographic techniques [36]. A calibration of the set-up transmittivity in the microwave range assures its suitability for STT excitation of the magnetization dynamics. Its effectiveness for STT experiments is shown in Ref. [44] by recording the voltage across a sample under I_{DC} injection.

Methods for current induced FMR

In this chapter we will introduce our experiment for the study of magnetization dynamics in an individual nanostructure.

The first characteristic of the experiment resides in the extremely reduced size of our nano-magnets. The technique of fabrication and making contacts to the samples allows us to study an individual nanostructure in a membrane template. Our goal is to investigate dynamical modes of the thin Co layer in a PSV structure (typically 30-80 nm in diameter and 5 to 7 nm in thickness, see chapter 2 fig.2.8 and 2.9). The reduced size of the device requires a local technique for the excitation and detection of magnetization dynamics and a good sensitivity to small magnetic volumes. In order to overcome these issues we performed transport measurements for both driving and probing magnetization oscillations, by means of the STT effect. An AC current induces a periodic torque on the magnetization and the device GMR acts as a probe of the magnetization dynamics. At the same time, this technique permits us to investigate the physics of spin momentum transfer between electrons and the magnetic moment of an ion and constitutes a local tool for FMR studies at the nano-scale. The achieved experimental results will prove the effectiveness of STT in showing uniform modes and spin wave excitations in our nanostructures. The use of AC STT as a probe for FMR investigation is itself an original aspect as only a few papers report analogous studies in SV devices [55–57] or magnetic tunnel junctions (MTJ) [41]. Moreover, we will see in chapter 4 that our measurements give an insight into interesting physics showing an extremely rich dynamic behavior (FMR of both magnetic layers and spin wave excitations of higher order).

The first part of the chapter is dedicated to the description of the physical mechanism behind excitation and detection of Current Induced FMR (CIFMR). In sec.3.1 we introduce a few experimental techniques for standard FMR. Then we focus on CIFMR (sec.3.2) evidencing how the AC STT can be used as a probe of the equilibrium magnetization dynamics. We also show, starting from very general assumptions, that current induced resonances lead to a direct voltage across the device (sec.3.2.2). The second part of the chapter is devoted to

the description of the experimental apparatus and procedures adopted in the experiment (sec.3.3).

3.1 Methods for detection of the magnetization dynamics

There are several methods for exciting and detecting magnetization dynamics in bulk systems and thin films. In general the magnetization equilibrium is perturbed by means of an oscillating magnetic field $\mathbf{h}_{rf}(\omega)$. The system response can be detected by monitoring its magnetic susceptibility (inductive methods) or by imaging techniques (optical or x-ray spectroscopy or scanning probe methods). We illustrate here the most common inductive methods for FMR studies, underlining their limits for the study of small objects (sec.3.1.1). In the following we give an overview of technical developments of imaging techniques for spin dynamics studies at the micro- and nano-scale (sec.3.1.2).

3.1.1 Inductive methods for standard FMR

In chapter 1 (see sec.1.1.3) we treated the problem of a magnetic body under a resonant perturbation. In particular we considered its response to an oscillating magnetic field $\mathbf{h}_{rf}(\omega)$:

$$\mathbf{m}_d(\omega, t) = \overline{\overline{\chi}}_{\mathbf{h}}(\omega) \mathbf{h}_{rf}(\omega, t) \quad (3.1)$$

where \mathbf{m}_d is the dynamic magnetization normalized with respect to the value at saturation $\mathbf{m} = \mathbf{M}/M_S = \mathbf{m}_{eq} + \mathbf{m}_d$. The analytical expression of the Polder tensor $\overline{\overline{\chi}}_{\mathbf{h}}(\omega)$, in the case of a simple geometry, is given in eq.1.18 (page 9). Equation 1.18 shows that $\overline{\overline{\chi}}_{\mathbf{h}}(\omega)$ changes abruptly when ω matches a system fundamental mode ($\omega = \omega_{res}$). Therefore the magnetic susceptibility can be monitored experimentally and used as a probe of magnetization dynamics.

The typical frequencies of magnetization dynamics in thin films or nano-objects are a few GHz. The first experimental issue is the realization of an oscillating magnetic field at such a high frequency. A convenient way to do so is to induce $\mathbf{h}_{rf}(\omega)$ by means of an AC current circulating in coil inductors or waveguides, adapted for high frequency transmission. In both cases the FMR is detected thanks to the coupling between the circuit and the magnetic flux induced by the sample. The variation of the magnetic flux reflects the magnetic configuration of the sample and then its dynamical behavior ($\Delta\Phi_h \sim \langle \mathbf{m}(t) \rangle S_{\perp}$, where S_{\perp} is the sample cross section perpendicular to the magnetic field). An alternative

is to induce a rf field in a resonant cavity containing the magnetic sample and to monitor the power of the reflected rf signal. The resonances are identified with the frequencies for which the sample absorbs more power and the rf signal at the output of the cavity decreases ($\Delta P(\omega) \propto \overline{\chi}_{\mathbf{h}}(\omega)$). In all these examples the adaptation of the global system to high frequency is a crucial point for the propagation and the detection of this AC response. Inductive elements and resonant cavities can be designed in order to have a good matching of the circuit for a well defined working frequency. The main technical issue is to ensure a broad-band detection. When using a resonant cavity the working frequency is determined by the fundamental modes of the cavity itself. The abrupt decrease of the quality factor at other frequencies does not allow for wide-band measurements. In the case of detection via inductive coupling the use of adapted coplanar wave-guides can supply a high quality matching for a broad-band spectrum ($> 10GHz$ with an increasing attenuation for higher frequencies up to $20GHz$). The small magnetic volume of nano-objects requires a high sensitivity to flux variations, as the magnetic flux induced by the sample is proportional to its cross section. We can make a quantitative evaluation of the signal induced by a device with dimensions in the range of $5 - 20 nm$ and $\mu_0 M_S \sim 1 T$, typical for the samples studied in our experiment. If the current injected into the circuit is $I_0 \simeq 100 \mu A$, a magnetization precession with an angle of aperture of about $5 - 10^\circ$ would induce a change of the total inductance $\Delta L = \frac{\Delta \Phi}{I}$ of a fraction of a *pico Henri*. Therefore the main problem of these techniques is the volume of magnetic material needed in order to have a detectable signal.

3.1.2 Spin dynamics from micro- to nano-scaled systems: a brief overview of experiments

In the study of magnetization dynamics the passage from a bulk system to nano-scaled objects implies a few technical issues. Notably, the reduced size of the device requires a local investigation technique with a precision of a few nm and that is able to detect the signal produced by a magnetic volume of a few hundred nm^3 . In recent years different experimental solution for spatially resolved FMR have been proposed and implemented.

One is the use of scanning probe techniques as magnetic resonance force microscopy (MRFM) [58–60] or scanning tunneling microscopy (STM) [61] to make a map of the magnetization with a sub- μm resolution. Another way to image the magnetization distribution with a high spatial resolution is to profit from the interaction between the polarization of photons and magnetic moments. In this perspective Brillouin light spectroscopy (BLS) is the more widely used technique. Several articles report on BLS studies of quantized and localized spin wave eigenmodes in micro- and nano-scaled samples with different geometries (eg. thin films, nanowires and arrays of nanodots) [12, 13, 62–64]. Another possibility is to profit from the magneto-optical Kerr effect (MOKE). Time resolved MOKE spectroscopy has been used to show uniform oscillations of the magnetization and stationary spin waves in sub-100

μm devices [65–67]. In optical spectroscopy the spatial resolution is determined by the laser spot size, intrinsically limited by the radiation wavelength to a few hundred nm. For this spatial limitation these techniques are frequently used to study arrays of nanostructured elements and not individual nanostructures (eg. arrays of regularly spaced nanodots [68] or strips [69]). The measurement of x-ray magnetic circular dichroism (XMCD) is a good alternative to the use of visible photons. It is usually employed for time-domain measurements in thin films down to a few tens of nm in thickness [70]. The recent development of a frequency-domain x-ray spectroscopy permits spatially resolved FMR to be performed and the magnetization dynamics in micron-sized elements to be studied [71]. This technique in principle can give a lateral spatial resolution of about 20 nm. The main complication of this technique is the need for advanced equipment which makes these measurements more difficult to realize.

The introduction of STT-driven FMR allows the study of devices smaller than those recently achieved with other techniques. The intrinsic local character of transport measurements makes it a perfect tool for FMR at a nano-scale. Moreover, it does not require the employment of sophisticated equipments or particularly delicate experimental procedures to be adopted.

3.2 Current induced FMR

In current induced FMR (CIFMR) the magnetization dynamics of a magnetoresistive (MR) device is excited by means of a continuous microwave current I_{AC} . I_{AC} has the double role of inducing and probing the magnetization dynamics. Thanks to the STT effect, the oscillating current results in a periodic torque on the magnetic moment of the device. This permits the use of transport measurements to induce the resonant rf perturbation, which is needed to excite the magnetization dynamics (see chapter 1 sec.1.1.3 at page 8). The precession of the spins is monitored by detecting the voltage which arises from the combination of I_{AC} and the MR of the sample. In contrast with inductive techniques seen in sec.3.1.1, here the sensitivity is mainly linked to the MR percentage of the device and not to its volume. All these aspects make the AC STT a perfectly suitable tool for FMR at nano-scale. The delicate point of this experiment is, once again, the impedance matching of the circuit. We will see that our technique allows the detection of the FMR by measuring a DC voltage (sec.3.2.2). This solves the problem of the circuit matching at the stage of the detection. The remaining issue is the injection of the microwave current into the sample. This point is less critical and can in part be overcome by adjusting the microwave source power, as we will see in section 3.3.

3.2.1 FMR excitation

In this section we deduce the temporal evolution of magnetization under AC STT by following the approach of Kovalev *et al.* [72]. We have already shown how, in presence of a spin polarized current, the magnetization dynamics can be described through the modified LLG equation (eq.1.30, page 20). If we consider the torque arising from an AC current $I(\omega)$, the STT acts as an oscillating perturbation, in analogy to $\mathbf{h}_{rf}(\omega)$ in standard FMR. The temporal evolution of magnetization can be written as:

$$\frac{\partial \mathbf{m}(t)}{\partial t} = LLG_{Stat} + \underbrace{\frac{\gamma \hbar}{2eV_m} \frac{\mathcal{P}}{M_S} I(t) [\mathbf{m}(t) \times (\mathbf{p} \times \mathbf{m}(t))]}_{\text{oscillating STT perturbation}} \quad (3.2)$$

where V_m is the volume of the considered magnetic layer, M_s the magnetization at saturation, \mathcal{P} the polarization function and \mathbf{p} the unit vector parallel to the polarization of the current. In order to solve eq.3.2 we can proceed as in the case of a field induced excitation (eq.1.13 at page 8). We linearize the equation and we deduce the analytical expression of $\mathbf{m}(t)$ in the case of a harmonic response to the STT perturbation. It is convenient to write the magnetization isolating the *equilibrium* and *dynamic* contribution:

$$\mathbf{m}(t) = \mathbf{m}_{eq} + \mathbf{m}_d(t)$$

where $\mathbf{m}_{eq} = \mathbf{m}(t=0)$ is the direction of the magnetization at equilibrium. The temporal evolution of magnetization can be written in terms of the response to the "zero" perturbation " $\mathbf{p} \times \mathbf{m}_{eq}$ ". In analogy to eq.3.1, we introduce a *torque susceptibility tensor* $\overline{\overline{\chi}}_{\mathbf{I}_{SP}}$. We define the vectorial quantity \mathbf{I}_{SP} which has the amplitude of the injected charge current I_{AC} and is oriented along the direction $\mathbf{p} \times \mathbf{m}_{eq}$. With this formalism, the linear response of magnetization to the oscillating perturbation can be written as follows:

$$\mathbf{m}_d(\omega, t) = \overline{\overline{\chi}}_{\mathbf{I}_{SP}}(\omega) \mathbf{I}_{SP}(\omega, t) \quad (3.3)$$

$$\mathbf{I}_{SP}(\omega, t) = I_0 e^{-i\omega t} \mathbf{p} \times \mathbf{m}_{eq}$$

The analytical expression of $\overline{\overline{\chi}}_{\mathbf{I}_{SP}}(\omega)$ is deduced by solving eq.3.2. We consider the magnetization as uniform in the whole layer and subjected to Zeeman and magnetostatic energies, neglecting the contribution of magnetocrystalline anisotropy (the exchange energy does not contribute to the effective field as \mathbf{m} is supposed to be spatially uniform). The magnetic layer is approximated with an ellipsoidal element. We look for the harmonic response of the magnetization to $I_{AC}(\omega)$. For ease of calculation we choose a coordinate system having the \hat{z} axis parallel to \mathbf{m}_{eq} (see cartoon in fig.3.1). We solve the LLG equation in the approximation of small angle precessions, which implies $m_{dx}(t) \simeq m_{dy}(t) \ll m_{eq} \simeq M_S$.

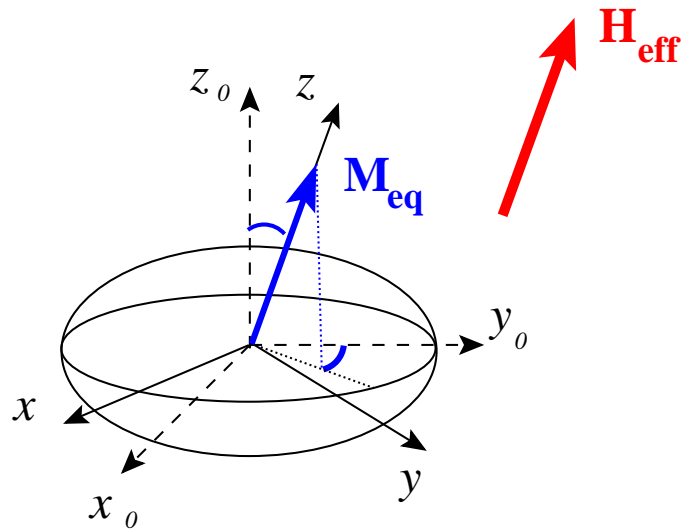


Figure 3.1 – Coordinate system adopted for the analytical solution of the LLG equation in the presence of STT.

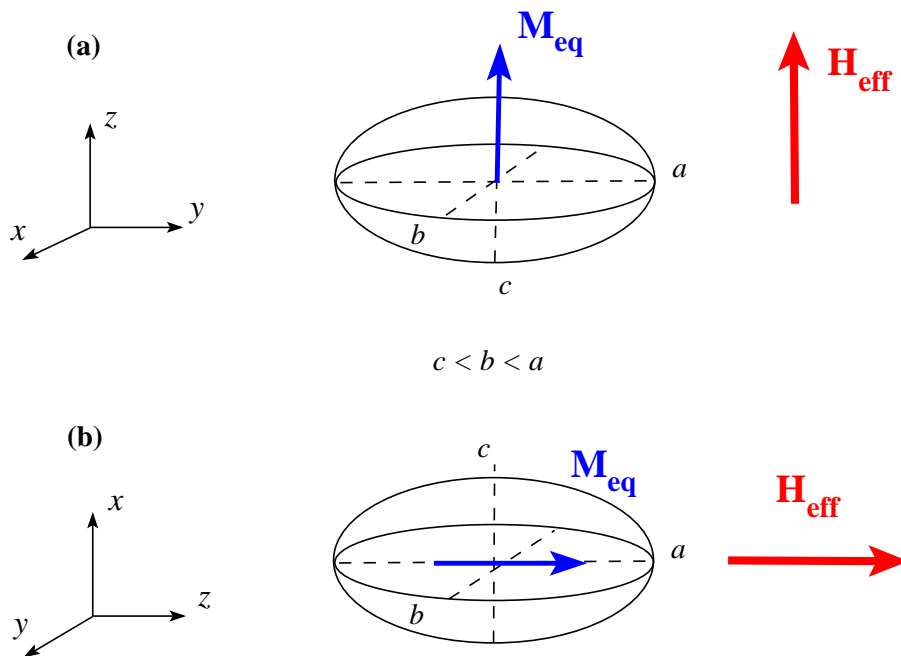


Figure 3.2 – Particular cases of effective field aligned with one of the system symmetry axes: (a) out of plane and (b) in plane.

In the simple case of an effective magnetic field aligned along one of the system easy axes, the system of coordinates O_{xyz} coincides with the easy axes of the ellipsoid, as shown in the two examples of fig.3.2.

In this simplified geometry we find:

$$\overline{\chi}_{\mathbf{I}SP}(\omega) = \frac{\beta \mathcal{P}}{(\omega_x - i\alpha\omega)(\omega_y - i\alpha\omega) - \omega^2} \begin{pmatrix} \omega_y - i\alpha\omega & i\omega \\ -i\omega & \omega_x - i\alpha\omega \end{pmatrix} \quad (3.4)$$

$$\beta = \frac{\gamma \hbar}{2eV_m M_S}$$

$$\omega_{x,y} = -\gamma_0 M_S \left(\frac{H_0^{(z)}}{M_S} - N_z + N_{x,y} \right)$$

α is the *damping* coefficient and \mathcal{P} the *polarization function*, $H_0^{(z)}$ is the component of the external magnetic field along \mathbf{m}_{eq} . With N_i we indicate the i -diagonal component of the demagnetizing tensor $\overline{\overline{N}}$, expressed in the coordinate system O_{xyz} . ω_x and ω_y correspond to the pulsations of the fundamental FMR modes along the two axes \hat{x} and \hat{y} . We find that the system resonates when ω matches $\sqrt{\omega_x \omega_y}$. We observe that expression 3.4 as well as the resonant pulsations are perfectly equivalent to the one of the Polder tensor (eq.1.18 on page 9). This shows how the AC STT excites the equilibrium dynamics of the system and can be a useful tool for FMR studies. The general expression of $\overline{\chi}_{\mathbf{I}SP}(\omega)$ for \mathbf{m}_{eq} oriented along an arbitrary direction is given in appendix A (eq.A.5). Symmetry breaking introduces additional terms linked to the off-diagonal components of the demagnetizing tensor and shifts the resonant frequency. The characteristic behavior of $\overline{\chi}_{\mathbf{I}SP}(\omega)$ remains unchanged.

3.2.2 Electrical detection

In a device presenting a MR (such as a SV), the precession of one magnetization vector induces a synchronous variation of the value of the resistance ($\Delta R_{MR} \propto \mathbf{M}_1 \cdot \mathbf{M}_2$). We will call the magnetizations of the thicker and thinner layers \mathbf{M}_{Thick} and \mathbf{M} respectively (corresponding to the unit vectors \mathbf{m}_{Thick} and \mathbf{m}). In a first approximation we consider that \mathbf{m}_{Thick} has no time dependence and \mathbf{m} is the magnetization subjected to the torque. The polarization of the current is aligned to \mathbf{m}_{Thick} (i.e. $\mathbf{p} = \mathbf{m}_{Thick}$). We note that, the torque being perpendicular to \mathbf{m}_{eq} ($= \mathbf{m}(t=0)$), it does not act on the modulus of \mathbf{m} but it only changes its orientation. With this observation and considering the harmonic response of $\mathbf{m}(t)$ we can write the total voltage across the device. We start from the general expression of the GMR (see chapter 1 eq.1.32 at page 22) and from eq.3.3. We define $\mathbf{t}_0 = \mathbf{p} \times \mathbf{m}_{eq}$.

We deduce:

$$\begin{aligned}
V(t) &= \left[R_0 + \frac{\Delta R_{max}}{2} \frac{\mathbf{M}_{Thick} \cdot \mathbf{M}(t)}{M_S^2} \right] I_0 \cos \omega t \\
&= \underbrace{R_0 I_0 \cos \omega t + \frac{\Delta R_{max}}{2} \mathbf{m}_{Thick} \cdot \mathbf{m}_{eq} I_0 \cos \omega t}_{V_\omega(t)} + \frac{\Delta R_{max}}{2} \mathbf{m}_{Thick} \cdot \mathbf{m}_d I_0 \cos \omega t \\
&= V_\omega(t) + \frac{\Delta R_{max}}{2} \mathbf{m}_{Thick} \cdot \Re \left\{ \overline{\overline{\chi}}_{\mathbf{I}_{SP}}(\omega) I_0 e^{i\omega t} \mathbf{t}_0 \right\} I_0 \cos \omega t \\
&= V_\omega(t) + \frac{\Delta R_{max}}{2} I_0^2 \mathbf{m}_{Thick} \cdot \mathbf{t}_0 \left[(\cos 2\omega t + 1) \Re \left\{ \overline{\overline{\chi}}_{\mathbf{I}_{SP}}(\omega) \right\} - \sin 2\omega t \Im \left\{ \overline{\overline{\chi}}_{\mathbf{I}_{SP}}(\omega) \right\} \right] \\
&= V_\omega(t) + V_{DC} + V_{2\omega}(t) \tag{3.5}
\end{aligned}$$

Apart from the term V_ω there are also zero and second harmonic components (V_{DC} and $V_{2\omega}$).

$$V_{DC} \propto \Re \left\{ \overline{\overline{\chi}}_{\mathbf{I}_{SP}} \right\}$$

$$V_{2\omega}(t) \propto \cos 2\omega t \Re \left\{ \overline{\overline{\chi}}_{\mathbf{I}_{SP}} \right\} - \sin 2\omega t \Im \left\{ \overline{\overline{\chi}}_{\mathbf{I}_{SP}} \right\}$$

We saw at the beginning of section 3.2 that the tensor $\overline{\overline{\chi}}_{\mathbf{I}_{SP}}(\omega)$ varies abruptly around a resonant frequency. As a consequence, we expect V_{DC} and $V_{2\omega}$ to change dramatically in the presence of a resonant excitation (I_{AC} at $\omega \simeq \sqrt{\omega_x \omega_y}$). It is by monitoring one of these two voltages as a function of ω that we can reveal the FMR. In particular, the detection of the V_{DC} term is extremely convenient as it permits the issues of circuit matching at high frequencies to be overcome.

Amplitude and shape of the V_{DC} signal

We consider the specific case of a spin valve where $\mathbf{I}_{SP}(\omega)$ is polarized by passing through the thicker magnetic layer ($\mathbf{p} = \mathbf{m}_{Thick}$). We identify the direction of \mathbf{m}_{Thick} with the angles θ_m and ϕ_m defined as shown in fig.3.3. The angle θ_m accounts for the relative orientation of layers and it is responsible for the GMR amplitude. ϕ_m is relevant only in determining the misalignment of \mathbf{M}_{Tk} with the easy axes of the magnetic layer. By introducing expression A.5 in eq.3.5 and isolating the V_{DC} term we obtain:

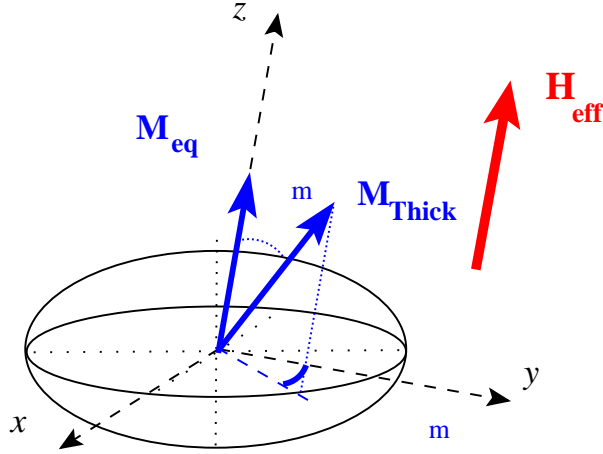


Figure 3.3 – Relative orientation of the two magnetizations of the SV device. The coordinate system is chosen to have the \hat{z} direction aligned with the equilibrium magnetization of the thin layer: \mathbf{M}_{eq} . The angles θ_m and ϕ_m indicate the direction of the thick layer magnetization (\mathbf{M}_{Thick}) with respect to this coordinate system. Note that θ_m is the angle relevant for the GMR while ϕ_m changes the orientation of the torque with respect to the layer easy axes ($\mathbf{t} = \mathbf{m} \times \mathbf{m}_{Thick} \times \mathbf{m}$).

$$\begin{aligned}
 V_{DC} &= \frac{\Delta R_{max}}{4} \beta \mathcal{P} I^2 \sin^2 \theta_m \\
 &= \frac{\omega^2 \alpha (\omega_x + \omega_y) + [\omega^2 (1 + \alpha^2) - \omega_{res}^2] [(\omega_x - \omega_y) \sin \phi_m \cos \phi_m + \omega_m (\cos^2 \phi_m - \sin^2 \phi_m)]}{[\omega^2 (1 + \alpha^2) - \omega_{res}^2]^2 + \omega^2 \alpha^2 (\omega_x + \omega_y)^2} \\
 &\stackrel{(1+\alpha^2 \rightarrow 1)}{\simeq} \frac{\Delta R_{max}}{4} \beta \mathcal{P} I^2 \sin^2 \theta_m \frac{A \omega^2 + B (\omega^2 - \omega_{res}^2)}{[\omega^2 - \omega_{res}^2]^2 + \omega^2 \alpha^2 (\omega_x + \omega_y)^2}
 \end{aligned} \tag{3.6}$$

$$\omega_m = -\mu_0 \gamma M_S N_{xy}$$

$$\omega_{res} = \sqrt{\omega_x \omega_y - \omega_m^2}$$

$$A = \alpha (\omega_x + \omega_y)$$

$$B = (\omega_x - \omega_y) \sin \phi_m \cos \phi_m + \omega_m (\cos^2 \phi_m - \sin^2 \phi_m)$$

The coefficients N_i and N_{xy} are diagonal and off-diagonal terms of the demagnetizing tensor in the system of coordinates $Oxyz$ (see fig.3.1) and then depend on the demagnetizing tensor and on the direction of \mathbf{m}_{eq} with respect to the layer easy axes. From eq.3.6 we see that in V_{DC} there are contributions from two different terms. The predominant term is A and it gives a signal with a Lorentzian shape. The coefficient B arises from a breaking of symmetry in the problem (displacement of \mathbf{m}_{eq} and \mathbf{m}_{Thick} from the easy axes of the layer). As the

B term has the shape of a dispersive-like signal (derivative of a Lorentzian curve) the effect of all asymmetries included in B is to distort the V_{DC} signal. B vanishes as \mathbf{m}_{Thick} aligns with one of the system easy axes and/or the layer ellipticity is reduced ($\omega_x = \omega_y$, so we are in a case of higher symmetry). In the particular case of \mathbf{m}_{eq} aligned with one of the system easy axes (as depicted in fig.3.2) we have:

$$\begin{aligned}\omega_m &\Rightarrow 0 \\ \omega_{res} &\Rightarrow \omega_0 = \sqrt{\omega_x \omega_y} \\ B &\Rightarrow B_0 = (\omega_x - \omega_y) \sin \phi_m \cos \phi_m\end{aligned}$$

The term B_0 is usually very small and the signal reduces to a simple Lorentzian curve. We note that the angle θ_m determines the amplitude of the V_{DC} , while ϕ_m only has the role of distorting the signal. The direction of \mathbf{m}_{eq} (angles θ and ϕ) determines the resonant frequencies and influences the shape of the signal as well (coefficient N_{xy} in B). From a rough numerical evaluation of expression 3.6 we deduce the high sensitivity of this detection technique. We take the typical parameters of our samples: $V_m \simeq 10^3 nm^3$, $I(\omega) \simeq 500 \mu A$, $\mu_0 M_S \simeq 1 T$, $\Delta R_{max} \simeq 0.4 \Omega$. We consider a polarization $P = 0.35$ and a relative angle between the magnetizations of $\theta_m = 5^\circ$ (we take $\phi_m = 0$), which gives $\mathcal{P} = 0.127$. The layer is approximated with a thin ellipsoid with a slight in-plane ellipticity ($c \ll b \lesssim a$), and the values of the demagnetizing coefficients are taken from [22]. For an external field $\mu_0 H_0 = 350 mT$ out of plane (see fig.3.2 (a)) we obtain a maximum V_{DC} of about $6 \mu V$.

It has to be noticed that this detection method is sensitive to magnetization excitations having a particular symmetry. In fact only magnetization precessions inducing a $\Delta R(t) \propto \cos \omega t$ give rise to a V_{DC} . The uniform oscillation modes of magnetization fit this requirement, assuring that the technique is perfectly suitable for FMR detection.

3.3 Experimental set-up

In this section we describe the experimental apparatus used for CIFRM in electrodeposited nanowires. In fig.3.4 is shown a schematic of the experimental set-up. The detection of the FMR is realized by both V_{DC} and $V_{2\omega}$ voltages. An additional proof of the resonances is given by recording the total V_{DC} under AC excitation in the presence of a small DC current (see subsec.3.3.3). The Co/Cu multilayered nanostructures are synthesized and electrically connected as explained in the previous chapter (chapter 2, sec.2.1 and 2.2). The sample holder is placed between the poles of an electromagnet allowing different field orientations by manual adjustment. The field amplitude can be swept between $-7 kOe$ and $7 kOe$. A bias-T allows the injection of AC and DC currents into the nanowire simultaneously. The DC output of the bias-T is connected either to a lock-in amplifier or to a voltmeter for GMR

or FMR electrical detection respectively. The AC channel is used to inject the microwave signal generated by an Agilent high frequency (HF) source. The frequency bandwidth of the HF source is $250\text{ kHz} - 20\text{ GHz}$ and the delivered power is between -20 and 20 dBm . For the detection of the $V_{2\omega}$ voltage we employ an Agilent Spectrum Analyzer (SA) having a nominal working range of $9\text{ kHz} - 26.5\text{ GHz}$. The microwave signal coming from the sample is decoupled from the injected microwave current through a directional coupler and sent to the SA. The directional coupler is mounted in such a way as to obtain a -20 dBm attenuation of the injected current and not to lower the amplitude of the signal produced by the nanostructure itself. The bandwidth of the $V_{2\omega}$ detection system is limited by the bandwidth of the directional coupler ($2 - 18\text{ GHz}$).

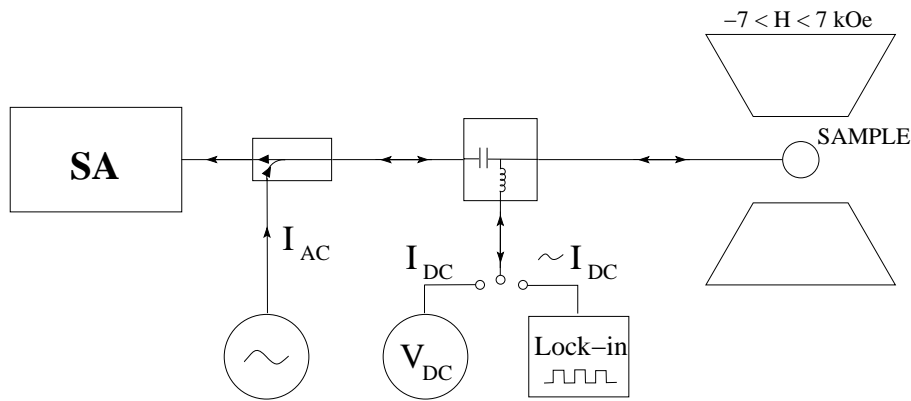


Figure 3.4 – *Experimental set-up for current induced FMR.*

3.3.1 V_{DC} detection of FMR

Once the sample GMR for a certain \mathbf{H}_0 geometry has been measured, the external field is set at a fixed value and a microwave current is injected into the nanowire. The $I_{AC}(\omega)$ frequency is swept typically from 1 to 16-18 GHz. The DC voltage across the nanostructure is monitored by a voltmeter. As we do not have any DC current, the V_{DC} signal is uniquely due to the demodulation effect presented in sec.3.2.2. The recorded voltage is plotted as a function of the $I_{AC}(\omega)$ frequency ($V_{DC}(\omega)$ spectra). The amplitude of the signal is of the order of tens of μV . This is in good agreement with what is expected from a numerical evaluation of equation 3.6 (see sec.3.2.2). Spectra are recorded at different values of H_0 . Examples of $V_{DC}(\omega)$ signal vs $\omega/2\pi$ are shown in the next chapter (sec.4.1, page 60).

3.3.2 $V_{2\omega}$ detection of FMR

The FMR is also detected via the $V_{2\omega}$ voltage (see eq. 3.5). The microwave voltage across the sample is measured with a spectrum analyzer, as explained at the beginning of this section. We perform a simultaneous detection of the $V_{2\omega}$ and V_{DC} voltages, in order to

make a direct comparison of the two detection methods. The numerical solution of equation 3.5 gives the same order of magnitude for the two voltage amplitudes. On the contrary, we observe that $V_{2\omega}$ is typically a few nV , so three orders of magnitude smaller than the V_{DC} voltage (fig.4.13 on page 80). This is completely due to the impedance mismatch between our sample-holder (nanowire + contact system) and the 50Ω input impedance of the spectrum analyzer. By reducing the frequency span of the measurement ($\sim 100\text{ KHz}$) and increasing the number of averages we obtain a good signal to noise ratio (see fig.4.13). The consequence is a long recording time. Unfortunately the mechanical instability of the electrical contact to a nanowire and its short average life-time make a long measurement an inadequate tool for our experiment. Moreover, our set-up allows for the measurement of microwave signals up to 18 GHz , which makes possible the $V_{2\omega}$ detection only for resonance modes up to 9 GHz . For these reasons the $V_{2\omega}$ spectrum was recorded only in a few cases. This measurement was used mainly as a proof of our technique and to validate the set-up as a tool for FMR studies.

3.3.3 V_{DC}/I_{DC} detection of resonances

The V_{DC} across a sample is detected while a small I_{DC} is injected into the nanowire. At the same time, a microwave current at a fixed frequency is passed through the sample. The total voltage measured by the voltmeter is:

$$V_{DC} = R_0 I_{DC} + R_{GMR}(\omega) I_\omega \quad (3.7)$$

When ω matches a resonance of the system, the V_{DC} signal increases and this ΔV_{DC} adds to the classical GMR signal. In the final plot of V_{DC} vs \mathbf{H}_0 , magnetization resonances appear as peaks superposed on the GMR curve (see in the next chapter fig.4.14 at page 81), as observed for the V_{DC} spectra. An interesting point of this detection method is that it permits a direct correlation to be found between the resonance and the relative orientation of the two magnetizations in the PSV. This gives information about the equilibrium configuration preceding and following the precession.

Current induced spin dynamics

In this chapter we present a study of the magnetization dynamics in an individual spin-valve structure of extremely reduced dimensions. We use a continuous microwave current to induce the dynamics of both magnetic layers in the nanostructure. Our results prove the excitation of spin waves of zero and higher order in nanomagnets smaller than what commonly found in the literature on experimental dynamical studies (30 nm in diameter and 5 and 20 nm in thickness).

Samples studied

Our technique for sample synthesis permitted several example of nanostructures to be studied, varying the thickness and the cross-section area of the magnetic layers. In this chapter we will focus on the results obtained for two different Pseudo-Spin-Valve structures referred to as PSV1 ($\varnothing = 80 \text{ nm}$ $Co_{(40nm)}/Cu_{(5nm)}/Co_{(5nm)}$) and PSV2 ($\varnothing = 30 \text{ nm}$ $Co_{(20nm)}/Cu_{(5nm)}/Co_{(5nm)}$). We present here the following results:

- **PSV1:**
Comparison of the different detection techniques developed in our set-up (V_{DC} and $V_{2\omega}$ voltages and V_{DC}/I_{DC} measurement);
- **PSV2:** study of the magnetization dynamics and of its evolution with the external magnetic field. The measurements are repeated in two different geometries:
 - \mathbf{H}_{\parallel} : field applied in the plane of the template.
 - \mathbf{H}_{\perp} : field applied perpendicular to the sample template.

The good stability of the electrical contact to the nanowire PSV1 permitted all characterization and detection measurements to be performed on it (GMR and static measurement of DC STT effect plus all our detection methods for current-induced magnetization dynamics). We present here some of the results from this sample aimed to the comparison of the different detection techniques (sec.4.4). For a deeper study of the spin dynamics

we concentrate here on the results obtained from the smaller of our samples, PSV2. Buda *et al.* have shown with 3D micromagnetic simulations that in cylindric nanoelements the eigenstate of the magnetization at zero field depends strongly on the radius of the dot [30]. For Co nanomagnets with a thickness ranging from 5 to 20 *nm* and a radii inferior to 30 *nm* it has been shown that the magnetization eigenstate is the uniform state. Starting from this result, we hoped that, due to its reduced size, this sample could present a dynamical behavior of easier interpretation. Our measurements show that this is only true in part and the dynamical behavior of the sample is in fact extremely complex. We detected several spin wave excitations of different index and spanning the whole frequency bandwidth of our measurements. However, we do not have any clear evidence of non-uniformity of the magnetization eigenstate at zero field in this sample and, different from what we observed on nanostructure PSV1, in this smaller sample we do not detect localized spin wave excitations. We follow the macrospin approach to interpret the lower frequency excitations and we propose a qualitative description of the higher frequency modes. The possibility of comparing the dynamical behavior of the sample in two different field configurations helps in determining the different geometrical parameters needed in our simulations and validates our results.

Preliminary characterization

GMR curves of both samples are shown and discussed in chapter 2 (fig.2.8 on page 39 and fig. 2.9 on page 40). We recall here that sample PSV2 does not present an hysteretic behavior (see minor loops recorded for the two field configurations). This implies that the switching is made through intermediate equilibrium positions and it is a reversible phenomenon. This point is particularly important from the prospect of our experiment as we want here to study the intrinsic dynamics of the two Co layers. We aim to perturb the magnetization equilibrium with a resonant microwave current and not to induce irreversible phenomena which would alter its dynamics (e.g. assisted switching).

The effect of a high density DC current on PSV1 was observed by monitoring the static voltage across the sample. The response of the resistance of the sample is shown by plotting the dV/dI signal vs the current (fig.4.1). This measurement can be used as an indication of STT effect [35] and thus as a validation of our technique of growing samples and contacting them for STT experiments. Indeed, in the late '90, when the concept of STT was first tested experimentally, several groups, including the one that provided the first experimental evidence (Tsoi *et al.* [35]), used this kind of characterization. An example of a recorded trace is given in fig.4.1. The sign of the current is defined as positive for conduction electrons traveling from the thin to the thick layer. We observe abrupt variations of the resistance for certain values of I_{DC} above a critical current I_{cri} of about 500(600) μA , for positive(negative) I_{DC} (values equivalent to a current density of the order of $10^7 A/cm^2$). The discrepancy between I_{cri} at positive and negative currents is due to the asymmetry

of the PSV (different thickness of the two Co layers), which could imply a different STT efficiency for the two current directions. The inversion of the resistance variation with the sign of I_{DC} is consistent with the hypothesis of STT effect and excludes the possibility of a field-induced effect.

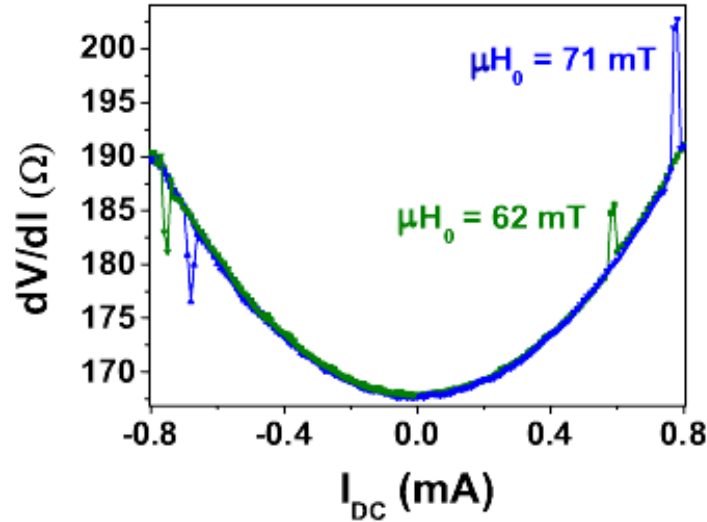


Figure 4.1 – dV/dI as a function of an injected high density current ($j \sim 10^7 \text{ A/cm}^2$). The dV/dI curves acquired are superimposed for two different values of the external field \mathbf{H}_0 (green curve $\mu_0 H_0 = 62 \text{ mT}$, blue curve $\mu_0 H_0 = 71 \text{ mT}$). The positive peak at positive current (electrons traveling from the thin to the thick layer) indicates a switching of the resistance from a lower to a higher value (misalignment of the magnetizations). Negative peaks at negative values of I_{DC} indicate an alignment of the magnetizations. The dependence of the critical current on the value of the magnetic field shows the relevance of the initial magnetic configuration.

Measurement parameters

The frequency f_{AC} of the microwave current is swept typically from 2 to 16 – 18 GHz by steps of 50 MHz. The amplitude of I_{AC} effectively transmitted into the nanowire is in the range of 100 – 400 μA , depending on the specific sample. The current amplitude is roughly constant for f_{AC} between 2 and 10 GHz and then decreases almost linearly at higher frequencies. The amplitude of I_{AC} at 18 GHz is reduced by about 20% (in the following I_{AC} indicates the current amplitude into the nanostructure and not the one delivered by the source). The procedure adopted for the calibration of the amplitude of I_{AC} is described in chapter 2, sec.2.2 on page 33. The amplitude H_0 of the external magnetic field can be varied between -700 and 700 mT . All measurements are done with the test structure at room temperature.

4.1 Spin dynamics in PSV2: experimental results

The V_{DC} spectra evidence numerous spin wave excitations in both the in-plane and out-of-plane configuration. We show here some of the recorded spectra and we comment on the variable shape and amplitude of the signals. The spin dynamics of the sample are summarized by plotting the frequency of each peak(dip) as a function of the external magnetic field. This permits us to identify some characteristic features of the dynamical modes as analyzed within the macrospin approximation.

4.1.1 V_{DC} signal

In figure 4.2 we show the V_{DC} spectrum (i.e. V_{DC} vs frequency of I_{AC}) acquired for an external field $\mu_0 H_0 = 73.7 \text{ mT}$ applied in the plane of the layers. The spectrum presents three distinct peaks of different shape and amplitude. The amplitude of the V_{DC} peaks

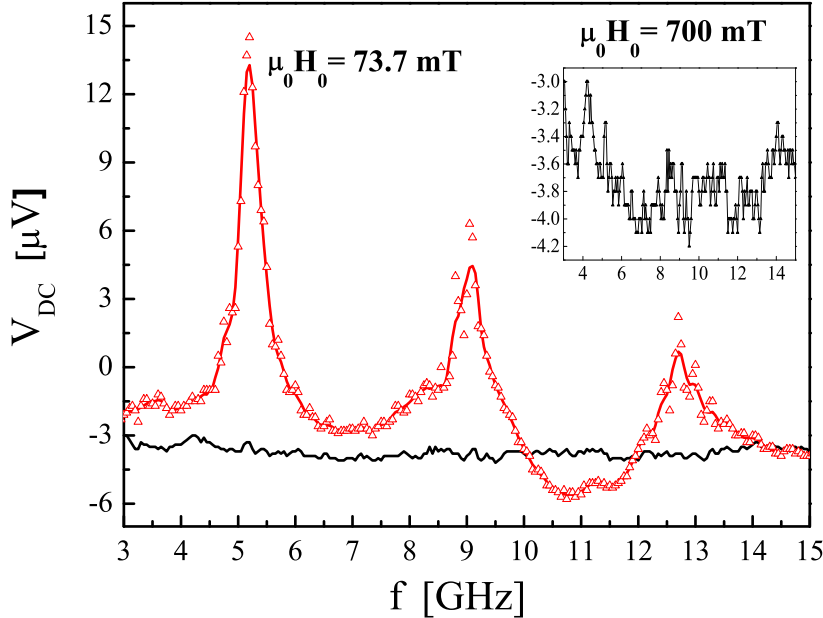


Figure 4.2 – V_{DC} signal vs frequency of excitation, signal acquired on sample PSV2. With the red scatter we show the spectrum acquired at $\mu_0 H_0 = 73.7 \text{ mT}$, almost in the plane of the layers. The black line represents the baseline of the signal, acquired in the same field configuration at $\mu_0 H_0 = 700 \text{ mT}$. Inset: zoom of the baseline signal.

depends on the angle of aperture of the magnetization precession and also on the spatial uniformity of the excitation. Indeed, our detection is based on the magnetoresistive effect of the sample and uniform excitations are more efficient in varying the average magnetoresistance. Therefore we expect the more intense excitations to correspond to the uniform precession of the magnetization (e.g. the peak at 5.3 GHz in fig.4.2). The low amplitude and the highly distorted V_{DC} signals could be associated to spatial non-uniform excitations (see sec.4.3.1 for a further discussion of the signal amplitude and shape). The black curve in the plot represents the V_{DC} signal in absence of any spin excitation (signal rescaled in the inset of fig.4.2). This "baseline" signal is typically recorded at high magnetic field (i.e. $\mu_0 H_0 \sim 700\text{ mT}$) applied approximately in the plane of the layers. We observe a weak frequency dependence of the V_{DC} baseline. We attribute this to changes of the current amplitude injected into the nanostructure, due to the frequency-dependent transmittivity of the circuit (electronic circuit+sample holder+metal bumps+nanowire).

The acquisition of $V_{DC}(\omega)$ spectra is repeated varying the value of the external field \mathbf{H}_0 . Examples of recorded spectra are given in fig.4.4 and 4.5 for the out-of-plane and in-plane configuration respectively. In fig.4.3 we show a close view of the spectra in the region of low field.

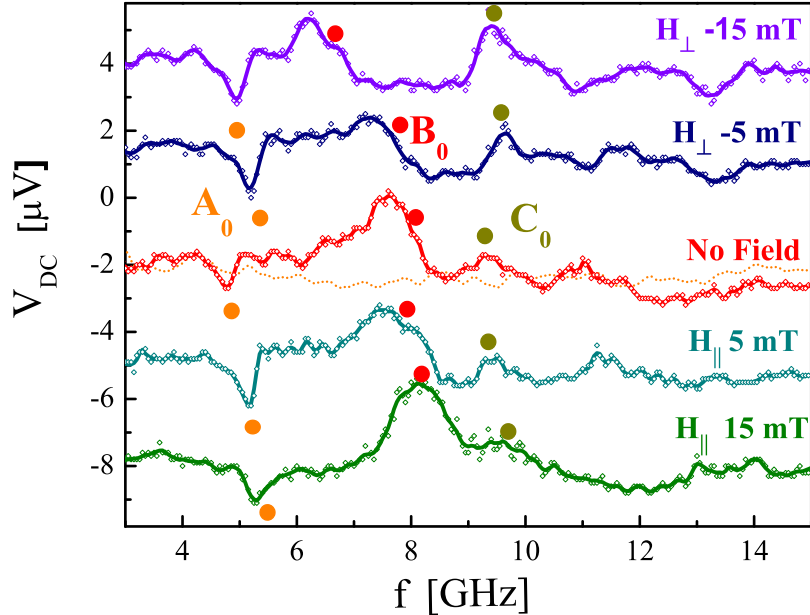


Figure 4.3 – PSV2: V_{DC} spectra at low magnetic field. In the center is shown the spectrum recorded at zero magnetic field. With \mathbf{H}_\perp and \mathbf{H}_\parallel we indicate a magnetic field applied in the plane or out of the plane of the magnetic layers. In the spectrum at $H_0 = 0$ we identify three modes (A_0 , B_0 , C_0) which evolve in a different way depending on the direction of H_0 .

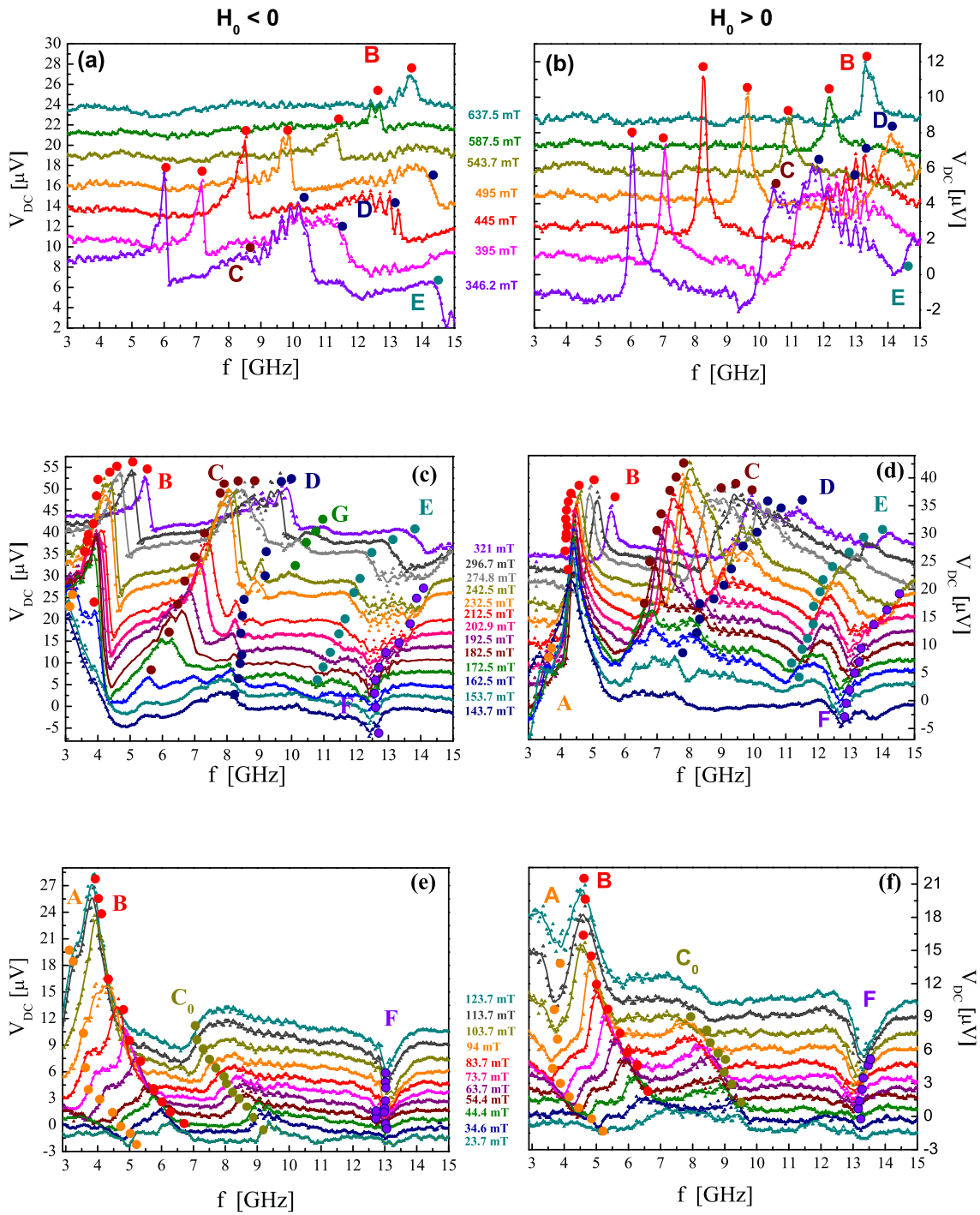


Figure 4.4 – PSV2: V_{DC} signal vs frequency in the H_{\perp} configuration. The spectra are acquired for different values of the external field H_0 . The signals are shifted along the vertical scale to make the data more legible. On the left (a, c, e) and right (b, d, f) panels we show the data for the two opposite directions of the field ($H_0 < 0$ and $H_0 > 0$). The dots in the graph indicate the different signals identified as dynamical modes.

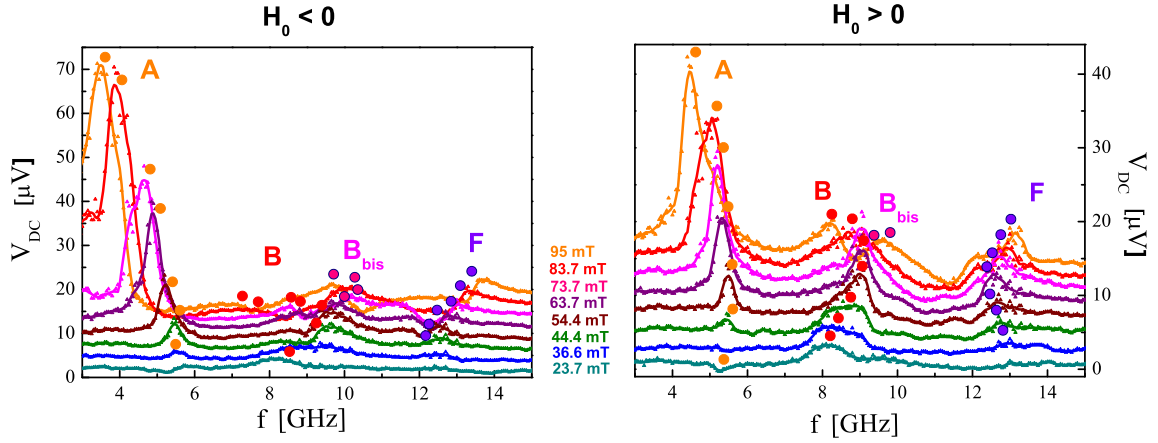


Figure 4.5 – PSV2: V_{DC} signal vs frequency in the \mathbf{H}_{\parallel} configuration, spectra acquired for different values of H_0 . The signals are shifted along the vertical scale to make the data more legible. On the left (a) and right (b) panels we show the data for the two opposite directions of the field ($H_0 < 0$ and $H_0 > 0$). The dots in the graph indicate the different signals identified as dynamical modes.

4.1.2 Peak dispersion

In fig.4.6 we plot the frequency of each peak(dip) as a function of the external field H_0 . The data for the field applied out-of-plane and in-plane are shown in panels (a) and (b) respectively. Due to the variable shape of the V_{DC} signal it is difficult to attribute to each excitation a well defined frequency. Case by case, we evaluated the shape of the signal in order to identify the resonant frequency (e.g., frequency corresponding to the max, the min or the average value of the V_{DC}). See the solid dots associated to the modes in fig.4.4 and 4.5). In some cases it is particularly difficult to distinguish the shape of the signal and the attribution of the frequency is in some part arbitrary. This is particularly true when two distinct excitations converge to the same interval of frequencies and superpose, i.e. the two magnetic layers resonate at the same frequency (e.g. see in fig.4.4 peaks A and B for $\mu_0 H_0$ between 80 and 160 mT). We have to consider that our measurement consists of the detection of the oscillating magnetoresistance:

$$R(t) \propto \mathbf{M}_1 \cdot \mathbf{M}_2$$

where \mathbf{M}_1 and \mathbf{M}_2 are the magnetizations associated to the two layers. When the two layers are precessing simultaneously the resulting $R(t)$ depends on the relative phase and amplitude of the two precessions. Even if the frequency of the two oscillations is slightly different it is difficult to distinguish the contributions of the two dynamical modes to the V_{DC} signal. In the cases which look ambiguous we mark the modes with small crosses in the diagram of fig.4.6. Peaks identified as belonging to a single evolving mode are indicated with dots of the same color and shape. The modes corresponding to the more intense peaks

in the V_{DC} spectra are represented with solid symbols. In the following we will indicate with a " \perp " and " \parallel " subscript the modes for the out-of-plane and in-plane field configurations.

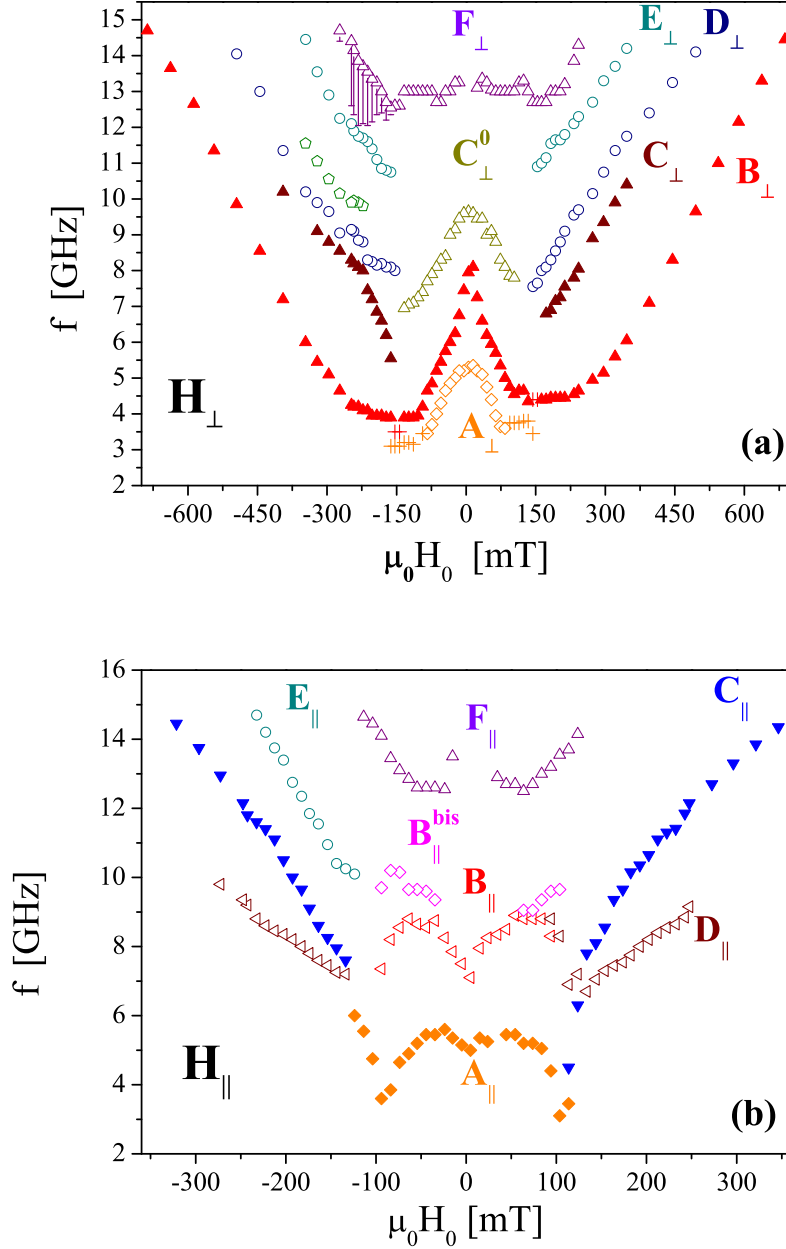


Figure 4.6 – Spin dynamics in sample PSV2 for (a) H_0 out-of-plane and (b) H_0 in-plane. The frequency of the excitations is determined from the V_{DC} spectra and then plotted as a function of the external field H_0 . We represent with solid symbols the excitations corresponding to the more intense V_{DC} signals. All the other excitations are indicated with open symbols. The small crosses correspond to the modes which superpose on each other and which are difficult to distinguish.

The $f(H_0)$ diagrams of fig.4.6 reflect the presence of several spin wave excitations of different order. The GMR curves of the sample are shown in fig.2.9 on page 40 (panel (a) for H_0 in-plane and (c) for H_0 out-of-plane). We observe that at low magnetic field ($|\mu_0 H_0| < 100 \text{ mT}$) the spectra are more complex and the dynamical behavior in the two field configurations is considerably different. When the field ramp goes through a field value at which a jump occurs in the GMR curves, several dynamical modes invert their slope. For \mathbf{H}_0 in-plane the $f(H_0)$ curves pass abruptly from a negative to a positive slope. In the case of \mathbf{H}_0 out-of-plane this inversion of trend is smoother. This is especially true for mode B_\perp which has a constant frequency for a large interval of fields past the switching field. These features are in good agreement with the sharp and smooth jumps in the GMR curves recorded for \mathbf{H}_0 in-plane and out-of-plane respectively. At high magnetic field we detect fewer modes and the frequency of all dynamical modes increases almost linearly with H_0 . The fact that the STT effect is still efficient means that the two magnetic layers are not perfectly aligned ($\mathbf{T}_{STT} \propto \mathbf{M}_1 \times (\mathbf{M}_2 \times \mathbf{M}_1)$). However, the magnetic configuration is quite stable and the increase of H_0 has only the effect of changing the effective field in the magnetic layers, without inducing a significant displacement of the magnetizations (i.e. inducing a relevant change of the free energy due to the variation of magnetostatic energy and the dipolar coupling between layers).

Finally, we observe that in the case of in-plane magnetic field we do not detect any magnetization excitations above $\mu_0 H_0 \simeq 350 \text{ mT}$. This can be due to two different reasons. Firstly, the resonant frequencies in this field configuration are considerably higher and it could be that some of the excited modes move out of the frequency bandwidth of our detection (e.g. mode C_\parallel). Secondly, we can presume that in the in-plane configuration the saturation of the layer magnetizations along the direction of the external field happens at lower field values. The closer we are to the perfect alignment of the magnetizations the less efficient the STT effect.

4.2 Interpretation of the spectra: nature of the excitations

The spin dynamics emerging from the dispersion diagrams (fig.4.6) is extremely complex. We distinguish numerous excitations which cover the whole frequency bandwidth of our setup. We interpret the dynamical modes at lower frequency as the fundamental eigenmodes of the two Co layers (spin wave excitations with $n=0$). The modes at higher frequencies are identified with spatially non-uniform excitations (high order spin waves). In order to support our assumptions we performed macrospin simulations of the fundamental modes of both magnetic layers. The comparison of the simulated curves with the experimental data is shown in fig.4.9. The possibility of comparing our simulations of the dynamical behavior

of the sample in two field configurations helps in determining the numerous parameters of our simulation (exact direction of the field and degree of ellipticity of the layers). The reduced dimensions of our nanomagnets make both dipolar and exchange interactions non-negligible. Moreover, the aspect ratio of our nanomagnets prevents us from using any simple approximation in the calculation of the dispersion of high order spin waves. Therefore, the discussion of the high frequency excitation is limited to some symmetry considerations and to comparison with results that exist in the literature.

4.2.1 Fundamental modes: macrospin simulations

We approximate each magnetic layer with a macrospin placed in the "magnetic environment" of the spin valve structure. In the calculation of the free magnetic energy of each macrospin we consider the contribution of Zeeman and magnetostatic interaction. We have:

$$\mathcal{F} = -\mathbf{M} \cdot (\mathbf{H}_0 + \mathbf{H}_{dip}) + E_{dem} \quad (4.1)$$

where \mathbf{M} is the magnetization vector, \mathbf{H}_0 the external magnetic field, \mathbf{H}_{dip} the dipolar field induced by the other layer and E_{dem} the demagnetizing energy. We start our simulation at high magnetic field ($\mu_0 H_0 \sim 800 \text{ mT}$) and we fix the initial equilibrium position of the two magnetizations parallel to the external field. Then we calculate the free energy in each layer and from its minimization we deduce the new equilibrium position of each magnetization. The pulsation ω_{FMR} of the fundamental mode of each layer is determined by solving the general equation [73]:

$$\frac{\omega_{FMR}}{2\pi} = \frac{\gamma}{M_S \sin(\theta_{eq})} \sqrt{\mathcal{F}_{\theta\theta} \mathcal{F}_{\varphi\varphi} - \mathcal{F}_{\theta\varphi}^2} \quad (4.2)$$

where M_S is the value of the magnetization at saturation, γ is the gyromagnetic ratio (28 GHz/T) and θ and φ are the angles formed by the magnetization with the plane of the layer, as defined in fig.3.1 (page 50). All derivatives are calculated at the equilibrium position of \mathbf{M} ($\theta = \theta_{eq}$, $\varphi = \varphi_{eq}$). This calculation is repeated for the two field configurations of our experiment and sweeping the value of the field from -700 to 700 mT . Note that this equation is solved for each layer independently, therefore all the possible mechanisms of dynamical coupling between the layers are neglected.

Demagnetizing energy The magnetic layers are approximated with flattened ellipsoidal elements of slight in-plane ellipticity. The approximation of ellipsoidal elements permits the magnetostatic energy to be written in the simple form:

$$E_{dem} = \frac{1}{2} \mathbf{M} \cdot \overline{\overline{N}} \mathbf{M} \quad (4.3)$$

with $\overline{\overline{N}}$ the demagnetizing tensor. The aspect ratio of the ellipsoid is fundamental in the determination of the demagnetizing coefficients and hence of the FMR frequencies (see

chapter 1 sec.1.1.3). Previous studies in our group evidenced that the metals can deposit into the pores at a canted angle, inducing a slight ellipticity of the magnetic layers (see fig.4.7). We determined the degree of ellipticity of the layers from the comparison of the simulations and the experimental data. We found that the best fit corresponds to an angle $\psi = 30^\circ$ between the layers and the plane of the template (see fig.4.7). This implies semi axes of the values: $a = 15 \text{ nm}$, $b = 17.3 \text{ nm}$, $c_t = 2.5 \text{ nm}$ and $c_{Tk} = 10 \text{ nm}$ (c_t and c_{Tk} correspond to the "half thickness" of the thin and thick layers respectively). The values of the demagnetizing coefficients are deduced from [22].

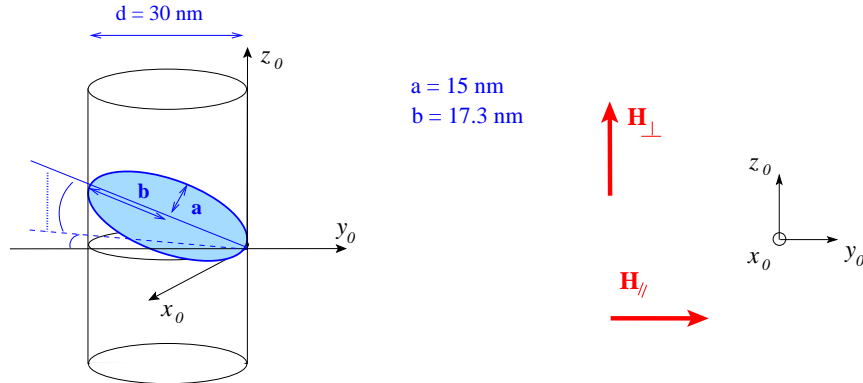


Figure 4.7 – Schematic representing the orientation of the magnetic layer in the nanowire. $O_{x_0y_0z_0}$ is the coordinate system of the laboratory, in which the field is applied on a well defined direction. The coordinate system of our calculation is that parallel to the easy axes of the ellipsoidal layer (see fig.4.8). We observe that the inclination of the layer does not result necessarily in the same canted angle for in-plane and out-of-plane field. Note that the effective orientation of the external field is also influenced by the possible inclination of the nanowire in the template, which is not considered in this simplified schematic.

Coupling between layers The interaction between the two magnetizations is approximated by a static dipolar coupling. The strength and the direction of the dipolar field are deduced from a finite element simulation. We divide the magnetic layers into elemental cells of $0.5 \times 0.5 \times 0.5 \text{ nm}^3$ and we calculate the contribution of each cell to the dipolar field induced in the center of the other magnetic layer. The orientation of the magnetic moments in the cells is derived from the minimization of the free energy. For the field induced by the thick layer on the thin one we find values of about $50 - 100 \text{ mT}$, depending on the relative orientation of the magnetizations. Due to the asymmetry of the volumes of the two layers the dipolar field on the thick layer is about 4 times smaller.

Parameters of the simulations

The value adopted for the magnetization at saturation is $\mu_0 M_s = 1.3 \text{ T}$. This value of M_s is between the tabulated value of pure Co ($\mu_0 M_s^{\text{pure}} = 1.6 \text{ T}$) and the value measured

for some examples of electrodeposited Co (see chapter 2, section 2.1.1 at page 29). This low value of M_S is not surprising for electrodeposited Co and can be explained due to the presence of Cu impurities in the Co layers. We have already mentioned the uncertainty in the real field orientation with respect to the plane of the layers. In the simulations we considered a canted angle with respect to the perfect in-plane and out-of-plane directions (see fig.4.8. The best fit of the data corresponds to the field orientations:

$$\begin{array}{ll} \mathbf{H}_\perp & \mathbf{H}_\parallel \\ \theta_H = 122^\circ & \theta_H = 20^\circ \\ \varphi_H = -25^\circ & \varphi_H = -45^\circ \end{array}$$

The displacement of the field orientation from a "real" in plane/out of plane configuration is then of the order of $20 - 30^\circ$. The two values of θ_H are coherent with a rotation of 90° between \mathbf{H}_\perp and \mathbf{H}_\parallel (note that we do not expect exactly the same canted angle for the two field configurations, as showed in the example of fig.4.7).

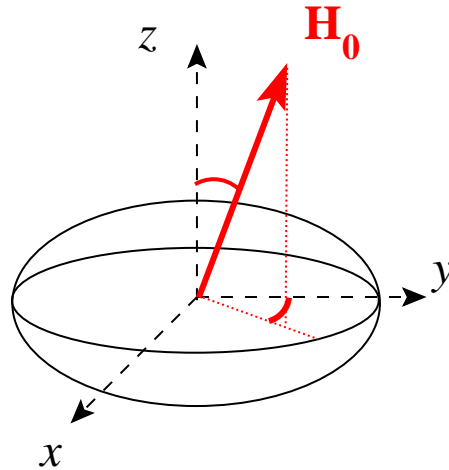


Figure 4.8 – Orientation of the magnetic field \mathbf{H}_0 with respect to the ellipsoidal layer. All the vectorial quantities in the Macrospin simulation are expressed in the coordinate system O_{xyz} .

Discussion of the results

The results of the "best fits" obtained from the macrospin simulation are given in fig.4.9 (a) for \mathbf{H}_0 out-of-plane and (b) for \mathbf{H}_0 in-plane. In the out-of-plane configuration we identify modes B_\perp and C_\perp as the FMR modes of the thick and the thin layer respectively. For the in-plane field the FMR excitations are associated to modes $A_\parallel + D_\parallel$ for the thin layer and C_\parallel for the thick layer. We observe that in general the excitations identified with the fundamental modes correspond to higher ΔV_{DC} in the spectra (modes indicated with solid symbols in fig.4.9 (a) and (b)).

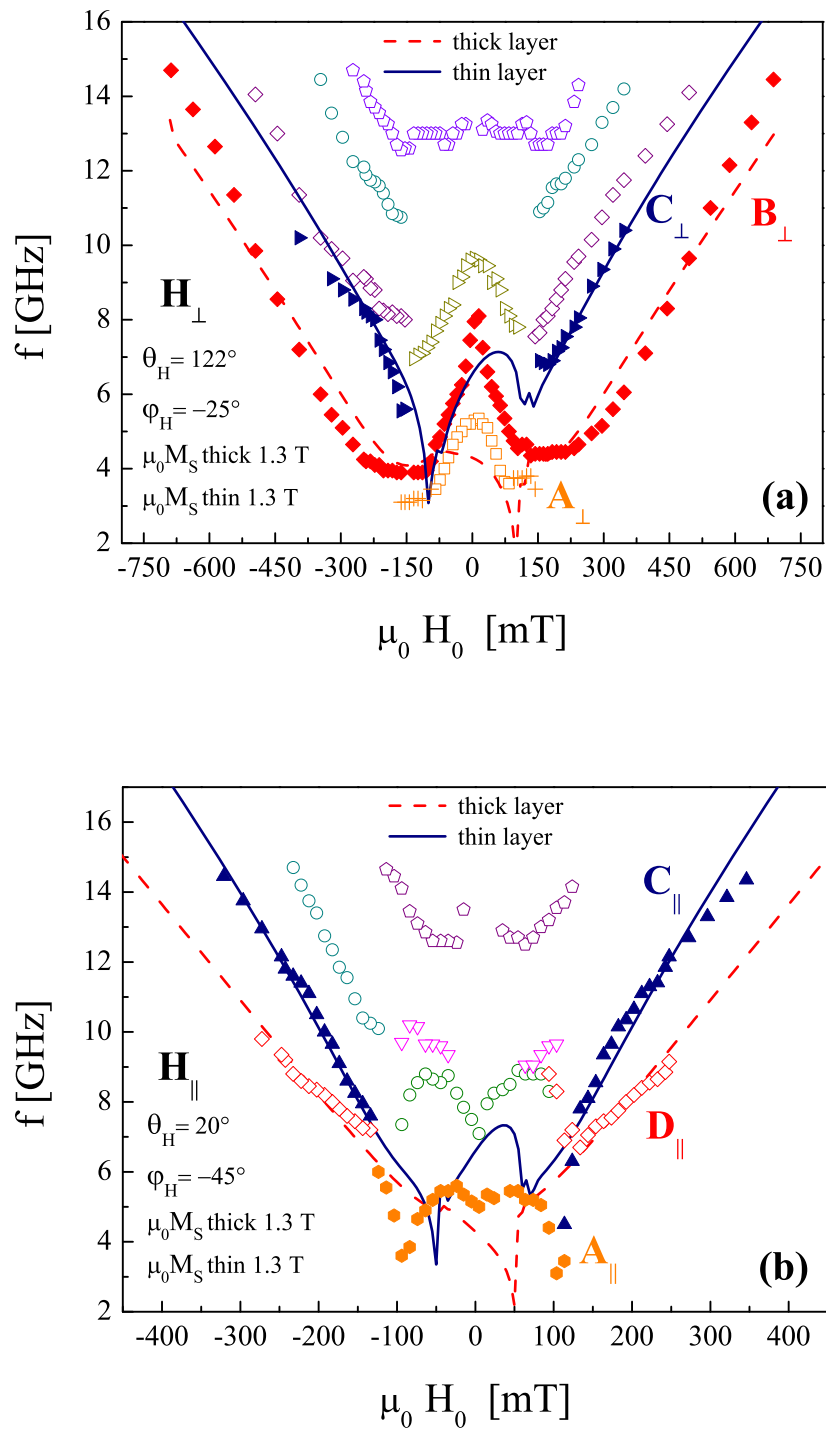


Figure 4.9 – Comparison of the macrospin simulation and experimental data for (a) \mathbf{H}_\perp and (b) \mathbf{H}_\parallel configurations. The fundamental modes calculated for the thin and the thick layer are represented by the blue solid line and red dashed line respectively. The experimental data are represented by the scatter points. The more intense excitations are indicated by solid dots and the other modes by open symbols.

The agreement between the simulations and the experimental data is not perfect but it reproduces most of the characteristic features of the experimental spectra. The values of the resonant frequencies and the slope of the $f(H_0)$ curves are reproduced in a quite satisfactory way, especially in the case of the thin layer. We observe a better fit of the spectra at high magnetic field, as we could expect. Indeed, at higher H_0 the effect of the inhomogeneous internal field of the magnetic layer became less significant with respect to the strong uniform external field and the magnetization distribution is expected to be more uniform. The lower agreement of simulations in the case of the thick layer is not surprising as this bigger layer could present a less uniform magnetization and more complex dynamics. The simulations account for the main differences between the two field configurations. First of all the frequencies of the resonances are considerably higher for \mathbf{H}_0 in-plane than for \mathbf{H}_0 out-of-plane. For in-plane field, it seems that the thin layer modes are out of the bandwidth when the applied field is about 350 mT , in good agreement with the experimental data (mode C_{\parallel} in fig.4.9 (b)). The field regions of inversion of the $f(H_0)$ curves are also well fitted (i.e. the region of switching of the magnetic layers). Moreover, in the out-of-plane configuration the simulation reproduces the smooth rotation of the thick layer evidenced by the plateau in its $f(H_0)$ curve.

We note that mode D_{\parallel} , interpreted as the fundamental excitation of the thick layer, disappears at a field of about 250 mT . This is probably due to the vanishing amplitude of the STT torque as soon as the layers align with each other. It is reasonable to observe an earlier disappearance of the thick layer excitation with respect to that of the thin layer (mode C_{\parallel}) as the STT is supposed to be more effective in smaller magnetic volumes ($\mathbf{t}_{STT} \propto V_m^{-1}$).

In the out-of-plane configuration the fundamental mode of the thin layer is in part superposed on mode A_{\perp} and then follows mode C_{\perp} (fig.4.9 (a)). We remark that our experimental data do not show a direct link between modes A_{\perp} and C_{\perp} (see fig.4.4 (e)-(c) and (f)-(d)). We attribute this discrepancy to the simultaneous precession of the two magnetic layers which makes it difficult to interpret the V_{DC} signal. Indeed, in the field range $60 - 150\text{ mT}$ mode A_{\perp} is almost superposed on the fundamental mode of the thick layer (mode B_{\perp}). The V_{DC} signal depends on the relative phase and amplitude of the simultaneous oscillations of the two magnetizations. This can result in V_{DC} peaks with a complex structure and therefore, in the region of superposition of the two excitations, our labeling of the modes is not pertinent (i.e. from 3 to 5 – 6 GHz, depending on the value of the magnetic field). Finally, it is important to point out that in our macrospin model we considered the oscillations of the magnetic layers as independent while they could couple through the dynamical dipolar coupling or other possible effects. This locking could dephase the oscillation of the two magnetizations and thus distort the V_{DC} signal (presumably to a higher degree in the thin layer, which is subjected to a higher dipolar field). Moreover, it is not clear if this coupling

could shift the frequency of the excitations leading to a displacement of the modes in the $f(H)$ diagram. All these hypotheses need to be supported by a study of the dynamical coupling between the layers. In conclusion we interpret the mode A_{\perp} as the fundamental mode of the thin layer. We attribute the discrepancies in our spectra to the simultaneous detection of the precession of the two layers and to the possible interaction of the two oscillating magnetizations.

4.2.2 Higher order spin wave eigenmodes

Due to the small volume of our sample we expect the spin wave spectrum to be quantized. The high frequency modes detected in our experiment seem to fit the characteristics of high order spin waves. Indeed, they present roughly the same frequency dependence than the uniform precessions and they are shifted to higher frequency. A detailed description of the spin wave excitations with $n > 0$ is a particularly complex problem due to the inhomogeneous dipolar-exchange interactions at the edges of the nanoelement. We have already seen that in the case of a nanodot this problem does not have an exact analytical solution [10]. Here we limit the interpretation of these high order modes to a qualitative discussion about their symmetry. Our detection technique is sensitive only to dynamical modes which induce a net change of the value of average resistance. The variation of the magnetoresistance is due certainly to the amplitude of the precession, but also to its phase. Indeed we have:

$$\begin{aligned}\Delta R(t) &\propto \mathbf{M}_1(t) \cdot \mathbf{M}_2 \propto e^{-i\omega t} e^{-i\Delta\phi} \\ \Delta R(t) I_{AC}(t) &\propto e^{-i\Delta\phi} \Rightarrow V_{DC}\end{aligned}\quad (4.4)$$

where $\mathbf{M}_1(t)$ is the the magnetization vector of the precessing layer and \mathbf{M}_2 represents the other layer, $I_{AC}(t)$ is the resonant microwave current which excites the precession and $\Delta\phi$ the possible dephasing between the precession of $\mathbf{M}_1(t)$ and the oscillating STT. In the case of a uniform precession this dephasing $\Delta\phi$ is expected to be zero and the V_{DC} is then a maximum. In a spatially non-uniform excitation the precessing spins are dephased with respect to each other and $\Delta\phi$ is non-zero and becomes a function of the spatial coordinates. The dynamic magnetization is then inhomogeneous, we assume the spatial dependence to be due only to the dephasing and we write:

$$\mathbf{M}_1(t, \mathbf{r}) = \mathbf{M}_1(t) e^{-i\Delta\phi(\mathbf{r})}$$

where \mathbf{r} is a vector spanning the whole volume of the layer and centered on the axis of the nanowire. If we consider \mathbf{M}_2 as uniform in the whole layer, we obtain:

$$\Delta R(t) \propto \mathbf{M}_1(t) \cdot \mathbf{M}_2 \frac{1}{V_m} \int_{V_m} e^{-i\Delta\phi(\mathbf{r})} d\mathbf{r}\quad (4.5)$$

where V_m is the volume of the layer associated to $\mathbf{M}_1(t)$. In the case of spin waves of even symmetry $\Delta\phi$ is an even function of \mathbf{r} and then the integral in equation 4.5 is zero. Therefore, we can exclude the possibility of detecting spin waves of even symmetry and we interpret the high frequency modes in our spectra as spin wave excitations with an even number of nodes (thus with an odd symmetry).

Montocello *et al.* have studied by Brillouin Light Spectroscopy (BLS) the dynamical spectrum of an array of 15 nm thick Py cylindrical dots [74] (dots of cross-section: $200 \times 500 \text{ nm}^2$). The authors detect several high frequency modes and, thanks to a numerical calculation based on micromagnetic simulations, they identify these modes with high order spin waves of different symmetry (Damon-Eshbach modes with wave-vector perpendicular to the applied field and backward-like modes with wave-vector parallel to the applied field). We observe a few interesting analogies with our spectra, especially in the case of the magnetic field applied out-of-plane. Fundamental and Damon-Eshbach modes have almost the same field dependence and present a dispersion relation similar to that observed in our experiment. The first backward-like mode ($n=2$) presents a different field-dependence at low magnetic field (frequency almost constant), as observed for mode F_{\perp} in fig.4.6.

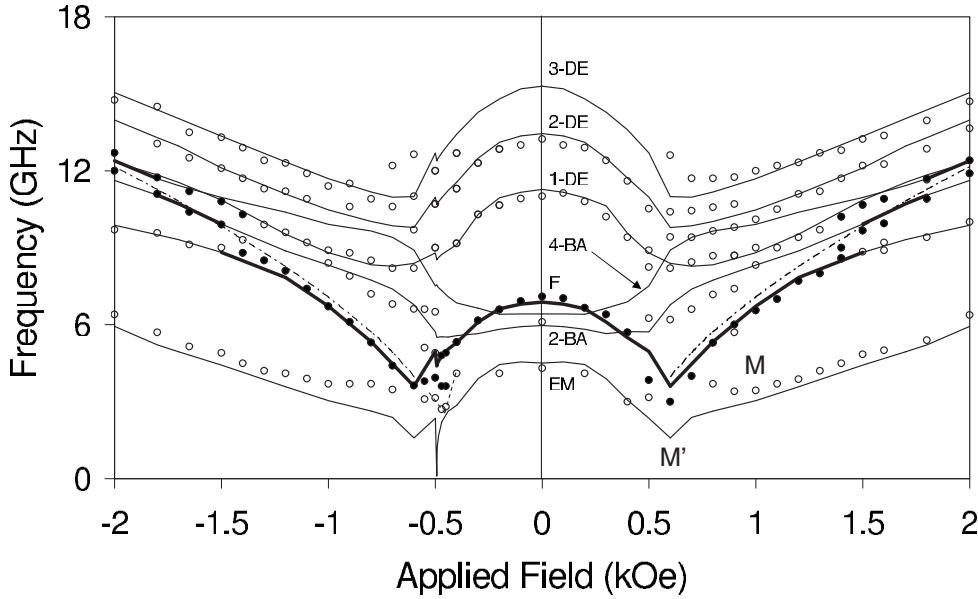


Figure 4.10 – Dynamical spectra for field out-of-plane of an array of Py cylindrical dots (15 nm thick dots of cross-section: $200 \times 500 \text{ nm}^2$). Symbols: experimental data from Brillouin Light Spectroscopy (BLS). The solid symbols represent the most intense excitations in the BLS spectrum. Solid lines: results of micromagnetic simulations evidencing several high order spin wave excitations of different symmetry and order n : Damon-Eshbach modes (n -DE) and backward-like modes (n -BA). The dash-dotted line represents the calculated FMR fundamental mode. Both experimental data and micromagnetic calculations evidenced the presence of a localized end mode (EM) (after [74]).

4.2.3 Role of the Oersted field

We discuss here the possible role of the Oersted field ($\mathbf{h}_{ind}(\omega)$) induced by the microwave current. Simple geometrical and symmetry considerations and a rough estimate of the amplitude of \mathbf{h}_{ind} lead to the conclusion that it cannot excite the fundamental modes of our layers. However, it is not evident whether the Oersted field can participate in the excitation of higher order spin waves. Moreover, this induced field tends to distort the uniform magnetization distribution. We suggest that through this distortion the Oersted field could influence the magnetization dynamics.

In our samples the magnetic structure is embedded in a $6\mu m$ long nanowire. All the parts of the circuit such as the massive gold layer on the bottom of the template and the Cu bumps on the top of the nanowire are at a few μm from the Co layers. A wire traversed by a current of $100\mu A$ induces a field of $0.2 Oe$ at the radial distance $|\mathbf{r}| \sim 1\mu m$. This value is small compared to the STT which, for the same current of $100\mu A$ and reasonable parameters, can be compared to a field of a few hundreds of Oe (the STT effect cannot be compared directly to a field effect as it does not correspond to any variation of the energy landscape, this estimation is only indicative of its effectiveness in exciting the magnetization precession). Moreover we have to consider that our estimation of \mathbf{h}_{ind} is done in the most favorable geometry ($\mathbf{h}_{ind} \propto \int \mathbf{r} \times d\mathbf{l}$ with $d\mathbf{l}$ an infinitesimal element traversed by the current). In the specific geometry of our system the Oersted field induced by all the elements outside the membrane is even smaller and then certainly negligible.

The discussion is reduced to the Oersted field induced by the current circulating in the nanowire itself (for a nanowire of $30nm$ in diameter and $I_{AC} \sim 100\mu A$, $\|\mathbf{h}_{ind}\| \sim 7Oe$). Such a field is inefficient in exciting spatially uniform modes. Indeed, the inhomogeneity of \mathbf{h}_{ind} and notably its poloidal symmetry exclude its possible role in inducing a coherent rotation of the magnetization of the whole layer. It is more difficult to make statement about its possible role in the excitation of higher order modes. In order to treat properly the effect of \mathbf{h}_{ind} on the magnetization dynamics we should abandon the macrospin approximation and adopt a micromagnetic description.

McMichael *et al.* have done micromagnetic simulations to describe the dynamical response of a small elliptical nanomagnet to rf fields of variable symmetry [18] (simulations done on Py elements of $350 \times 160 \times 15 nm^3$). The authors declare that field pulses of a certain spatial symmetry are able to excite spin waves of a corresponding symmetry. Therefore, it could be that in our experiment the induced field participates in the excitation of higher order spin waves. On the other hand, it is evident how \mathbf{h}_{ind} tends to break the magnetization uniformity in the layer. Notably, its higher value at the edges of the layer could distort the magnetization on the borders. This distortion of the magnetic configuration

could enhance the efficiency of the STT effect, especially in the proximity of a parallel or antiparallel alignment. In this case the role of the Oersted field would not be to excite the precession but simply to induce a magnetization misalignment which acts as a trigger of the STT excitation. This hypothesis is supported by the results of Carpentieri *et al.* on a micromagnetic study of STT-induced switching in sub-100 *nm* Co and Py nanoelements [75]. The authors observed a crucial role of the induced Oersted field in triggering the STT-induced magnetization dynamics.

4.3 Further discussions

Our data show that excitations can result in V_{DC} signals of variable shape. If the V_{DC} arises from a uniform oscillation of the magnetization its shape is described by eq.3.6 (see previous chapter, sec.3.6 on page 53). However, a dephasing between the precessing magnetization and I_{AC} would imply a distortion of the V_{DC} signal. In the following we discuss the possible role of this dephasing in the case of uniform and non-uniform excitations. We analyze the shape of the V_{DC} signal in the case of a uniform excitation and we identify some features which are consistent with our experimental data. Finally, we discuss the systematic distortion induced by the inversion of the field in some of the modes (e.g. mode B_{\perp} in fig.4.4 (a) and (b) and mode E_{\perp} in panels (c) and (d)).

4.3.1 Peaks amplitude and shape

It has been shown that the magnetization precession induced by a direct current I_{DC} in the presence of a small resonant current ($I_{AC} \sim 1\% I_{DC}$) can adjust its oscillation at a dephased angle $\Delta\phi$ with respect to the phase of I_{AC} [76]. However, there is no indication nor apparent reason that this could occur in the case of a precession induced by a pure microwave current. In the absence of other oscillating interactions we expect the magnetization to be in phase with I_{AC} . The case of spatially non-uniform excitations is more complex. Indeed, the spins are precessing with different phases in the different spatial areas of the layer and a dephasing with respect to the current is clearly present. It is not obvious what is the average value of this dephasing factor (see eq.4.5 and its discussion in sec.4.2.2). In order to make a statement about the shape of the V_{DC} signal we would need a map of the spatial distribution of the excitation and a good knowledge of the mechanism of interlocking between spins and microwave current. Here we limit our conclusion to the fact that it is sufficient to have in the magnetic layer a higher number of "areas" oscillating out-of-phase to obtain a negative peak in the V_{DC} spectrum. However, we do not find surprising the presence of negative or highly dephased peaks corresponding to spatially non-uniform excitations.

Spatially uniform excitations

The shape of the V_{DC} signal arising from a coherent rotation of the magnetization can be described by equation 3.6 (see previous chapter on page 53). We analyze here the shape of this signal and how it evolves when increasing the value of the external magnetic field (fig.4.11). We find that the increase of the field implies a change in the shape of the V_{DC} , in agreement with some of the features of our spectra (e.g. mode B_{\perp} in fig.4.4 (a) and (b)).

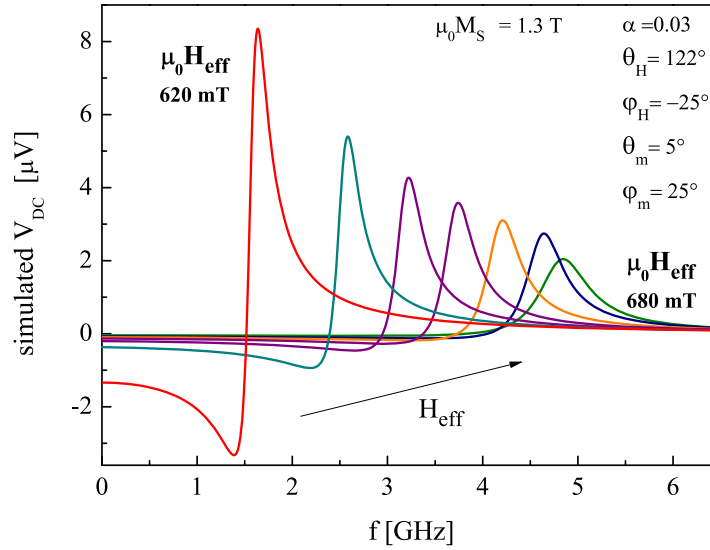


Figure 4.11 – Evolution of the V_{DC} signal at increasing effective field (H_{eff}). All the geometrical and physical parameters are fixed and only the value of H_{eff} is varied. We observe that the peak evolves toward higher frequencies and at the same time decreases its amplitude. We remark a considerably higher distortion of the signal at lower H_{eff} .

The V_{DC} signal is composed of two curves having respectively a Lorentzian and a dispersive shape (see eq.3.6). The relative weight of these two components depends on some geometrical aspects. Notably, each element of asymmetry such as the ellipticity of the layer ($a \neq b$) and the canted orientation of \mathbf{H}_0 contribute to the distortion of the V_{DC} signal. We fix all the geometrical parameters according to the results of our simulations and we analyze how the V_{DC} signal evolves when we increase the magnetic field. Note that we do not perform a real simulation of the shape of the peak as we just fix "by hand" the effective field in the layer. We calculate the V_{DC} signal for the thin layer in the out-of-plane configuration (i.e. $\theta_H = 122^\circ$ and $\varphi_H = -45^\circ$). The degree of ellipticity of the layer is the same adopted for the FMR simulations. The angles θ_m and φ_m indicate the direction of the thick layer (see fig.3.3 on page 53). In fig 4.11 we plot several V_{DC} curves calculated by varying the value of the effective field between 620 and 670 mT. We observe that the V_{DC} signal is

highly distorted at $\mu_0 H_{eff} = 620 \text{ mT}$. The increase of the field determines a significant change of the peak shape. The intensity is reduced as well as the degree of distortion and at $\mu_0 H_{eff} = 670 \text{ mT}$ the signal is close to a Lorentzian curve. These features reproduce quite well what was observed for peak B_{\perp} in the region of high field, fig.4.4 (a) and (b). We note that the vanishing intensity of the V_{DC} at high magnetic field is also explained by the lower efficiency of the STT effect in the near saturated regime ($\mathbf{t}_{STT} \propto \mathbf{m}_1 \times \mathbf{m}_2$). This is also assumed as the explanation of the general higher intensity of the excitations in the region of strongly misaligned magnetizations (H_0 at about the switching field).

In conclusion we can affirm that a the possible asymmetry of the peaks associated to the fundamental modes can be easily reproduced. Moreover, the shape of the signals can evolve and change when varying the external magnetic field. However, we do not expect the peaks to invert their sign and the only explanation that we find for the dips in the spectra is an out-of-phase oscillation of the magnetization with respect to the STT effect.

4.3.2 Comparison of the spectra at $H > 0$ and $H < 0$

From the comparison of the spectra recorded at positive and negative fields we observe an inversion of symmetry of a few of the V_{DC} peaks (fig.4.4, modes C_{\perp} and E_{\perp} in the whole field scan and B_{\perp} at high field). This apparent dephasing linked to the inversion of the field is not explained by our simple macrospin model, which presumes a "pure" STT excitation of the resonances. We make here some symmetry considerations to build up a hypothesis which could account for this effect.

In fig.4.4 and 4.5 we can easily observe the effect of the inversion of the field on the V_{DC} traces (data for positive and negative fields displayed in adjacent panels). We remark that in the out-of-plane configuration the inversion of the magnetic field seems to induce a systematic dephasing of some of the dynamical modes (see modes C_{\perp} , E_{\perp} and B_{\perp} in fig.4.4). The presence of small discrepancies between the two sides of the spectra is not surprising and can be attributed to different values of the effective field (e.g. due to a non-identical magnetic configuration or defects in the deposited layers). However, a different effective field could distort the shape of the peaks, but its predominant effect would be to shift their frequencies. The most reasonable hypothesis for the systematic distortion of the signals is the introduction of a dephasing between the magnetization precession and the microwave current, with the inversion of the field H_0 . We propose the Oersted field induced by I_{AC} to be the cause of this effect of dephasing.

All the equations describing our system are invariant under a simultaneous inversion of the magnetic field and the magnetizations. Therefore, with the inversion of H_0 the temporal

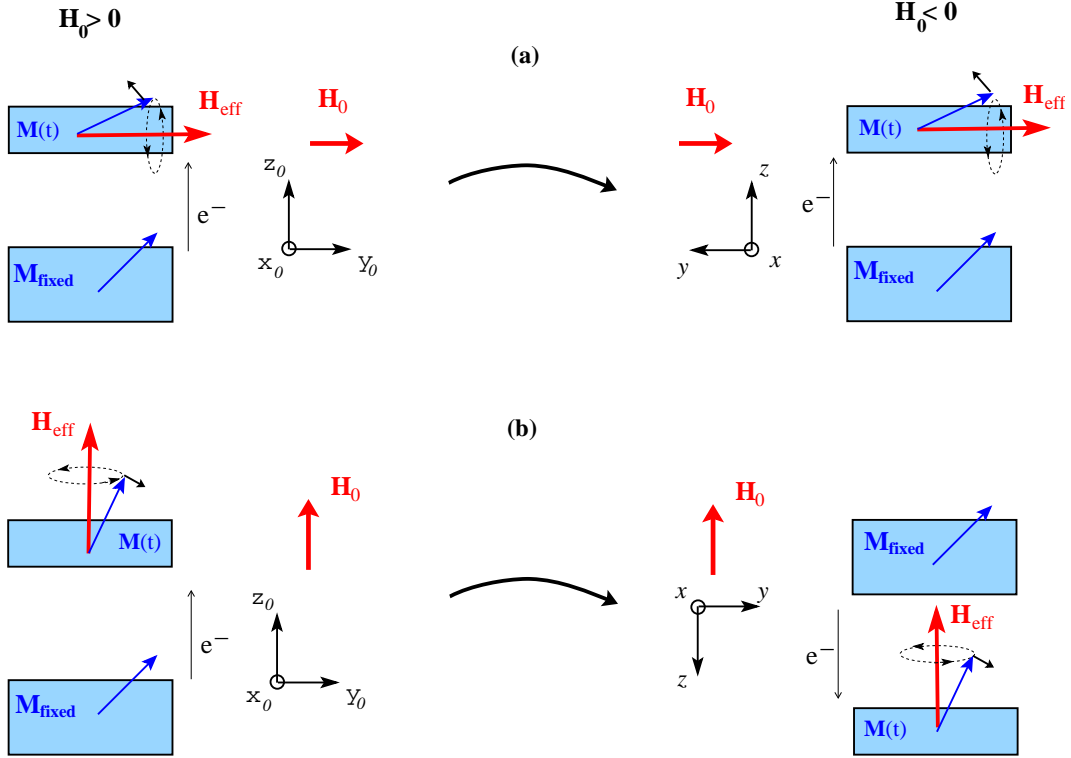


Figure 4.12 – Effect of the field inversion on the dynamical description of the spin-valve structure. The inversion of the field is viewed as an inversion of the spatial coordinate parallel to it. (a) \mathbf{H}_0 in-plane: the inversion of the field does not bring any visible change. (b) \mathbf{H}_0 out-of-plane: the inversion of the field results in the inversion of the position of the layers. The relative sign of the STT effect and of the current is inverted.

evolution of the magnetization and the V_{DC} response should be unchanged. This can be easily shown by writing the main equations governing our problem. It is convenient to treat the field inversion as an inversion of spatial coordinates, as depicted in fig.4.12. We analyze the case of field applied out-of-plane and thus parallel to the current flow (fig.4.12 (b)). We consider one magnetic layer as fixed (\mathbf{M}_{fixed}) and we write the magnetization of the precessing layer in the form: $\mathbf{M}(t) = \mathbf{M}_{eq} + \mathbf{m}(t)$.

We obtain:

$$\begin{array}{ll}
 O_{x_0, y_0, z_0} & O_{x, y, z} \quad z = -z_0 \\
 I_{AC}(t) = I_0 e^{-i\omega t} & I'_{AC}(t) = I_0 e^{-i\omega t} e^{-i\pi} = -I_{AC}(t) \\
 \mathbf{M}_{fixed}, \mathbf{M}_{eq} & \mathbf{M}_{fixed}, \mathbf{M}_{eq} \\
 \mathbf{m}(t) = I_{AC} \bar{\chi}_I (\mathbf{M}_{fixed} \times \mathbf{M}_{eq}) & \mathbf{m}'(t) = -e^{-i\pi} I_{AC} \bar{\chi}_I (\mathbf{M}_{fixed} \times \mathbf{M}_{eq}) = \mathbf{m}(t) \\
 \mathbf{h}_{ind} & \mathbf{h}'_{ind} = e^{-i\pi} \mathbf{h}_{ind}
 \end{array} \tag{4.6}$$

We note that $\mathbf{m}'(t) = \mathbf{m}(t)$ is unchanged, due to the simultaneous inversion of the electron flow and of the position of the thin and thick layers in the frame O_{xyz} . This invariance contradicts what is observed in our spectra.

A possible explanation for this phenomenon could be the presence of a further interaction which breaks the invariance of the system under simultaneous inversion of field and magnetizations. The Oersted field \mathbf{h}_{ind} induced by the microwave current fits this requirement. A magnetization precession triggered by \mathbf{h}_{ind} would be of the form:

$$\frac{d\mathbf{M}(t)}{dt} \propto \mathbf{M} \times \mathbf{h}_{ind}$$

With the inversion of \mathbf{H}_0 we have:

$$\begin{array}{ll} O_{x_0,y_0,z_0} & O_{x,y,z} \\ I_{AC}(t) & I'_{AC}(t) = -I_{AC}(t) \\ \mathbf{h}_{ind} & \mathbf{h}_{ind} = \mathbf{h}_{ind} e^{i\pi} \\ \mathbf{m}(t) & \mathbf{m}'(t) = e^{i\pi} \mathbf{m}(t) \end{array} \quad (4.7)$$

Therefore, if the precession of the magnetization is somehow "locked" to \mathbf{h}_{ind} we can expect a visible dephasing between the V_{DC} traces at positive and negative field.

We have to evaluate the relevance of our hypothesis considering the specific excitations which invert their symmetry under the inversion of \mathbf{H}_0 . First of all, we observe that this "dephasing" effect is visible only in the case of \mathbf{H}_\perp (modes C_\perp^0 , \mathbf{E}_\perp and \mathbf{B}_\perp). Therefore, this configuration is where the magnetic field has a stronger out-of-plane component, in agreement with what is expected. Mode \mathbf{B}_\perp is the fundamental mode of the thick layer and this "dephasing effect" is observed even at high magnetic field. The amplitude of $\mathbf{h}_{ind}(t)$ is here about 1% of the static field H_0 . Thirion *et al.* showed that transverse field pulses of a few mT can induce large angle precessions of the magnetization even in the presence of a static field of $\sim 100 - 200 mT$ [77] (measurements of microwave assisted switching done on Co nanoparticles, $\varnothing = 20nm$). Therefore we can imagine that the oscillating Oersted field in our nanowire is strong enough to induce the precession of the magnetization at the edges of the sample. We do not expect this effect to be significant if compared to the STT induced precession but we suggest that it triggers the STT-induced precession of the magnetization. Mode C_\perp^0 is located in the region of antiparallel alignment of the magnetizations, therefore in a region of low efficiency of the STT and we can imagine the same mechanism of triggering described for mode \mathbf{B}_\perp . In the case of mode \mathbf{E}_\perp we are already in a field region where the STT is particularly efficient. However, this excitation is probably spatially non-uniform and we have already discussed the possible role of the Oersted field in triggering high order

spin waves or, possibly, in their excitation. Micromagnetic simulations would be needed to verify our hypothesis of the Oersted field as a "trigger" of magnetization excitations and to check the validity of our qualitative description.

4.4 Comparison of alternative detections

The measurements shown in this section have been performed on sample PSV1. The dynamical behavior observed in this sample is comparable to those of sample PSV2 in the two field configurations (sec.4.1-4.3). For the detailed description of the V_{DC} spectra and their field-dispersion we refer to Ref.[78].

4.4.1 $V_{2\omega}$

In fig.4.13 is shown the $V_{2\omega}$ recorded simultaneously to the V_{DC} signal. The acquisition is made at a fixed field $\mu_0 H_0 = 110 \text{ mT}$. The two voltages are almost superposed showing the good agreement of the two detection techniques. We note the small amplitude of the 2ω signal is due to the set-up mismatch.

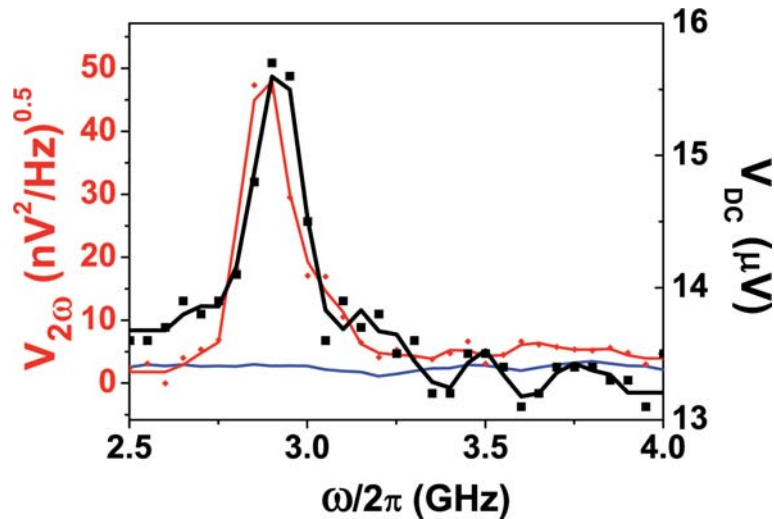


Figure 4.13 – PSV1: AC STT induced precession. Microwave current of about $450 \mu\text{A}$, external field fixed at the value $\mu_0 H_0 = 110 \text{ mT}$. **Red rhombuses:** $V_{2\omega}$ detection performed with the spectrum analyzer. Data refer to the red scale on the left. **Black squares:** V_{DC} detection, data referring to the black scale on the right. The two spectra evidence a magnetization excitation at the frequency of 2.8 GHz .

4.4.2 V_{DC}/I_{DC} measurement

An example of data recorded with the V_{DC}/I_{DC} detection is shown in fig.4.14 (a). The V_{DC} voltage is acquired under the injection of the currents:

$$\begin{aligned} I_{\sim DC} &= 10\mu A & \omega/2\pi &= 413\text{ Hz} \\ I_{AC}(\omega) &\simeq 450\mu A & \omega/2\pi &= 4\text{ GHz} \end{aligned}$$

The position ($\mu_0 H_0 = 60\text{ mT}$) and the amplitude of the peak ($\Delta V_{DC} = 0.8\mu\text{V}$) are in good agreement with what is observed in the corresponding $V_{DC}(\omega)$ spectrum (data shown in fig.4.14 (b)). We note that this simple detection technique without any lock-in demodulation permits the resonance of about 10^6 Bohr magneton to be detected with a reasonable signal-to-noise ratio.

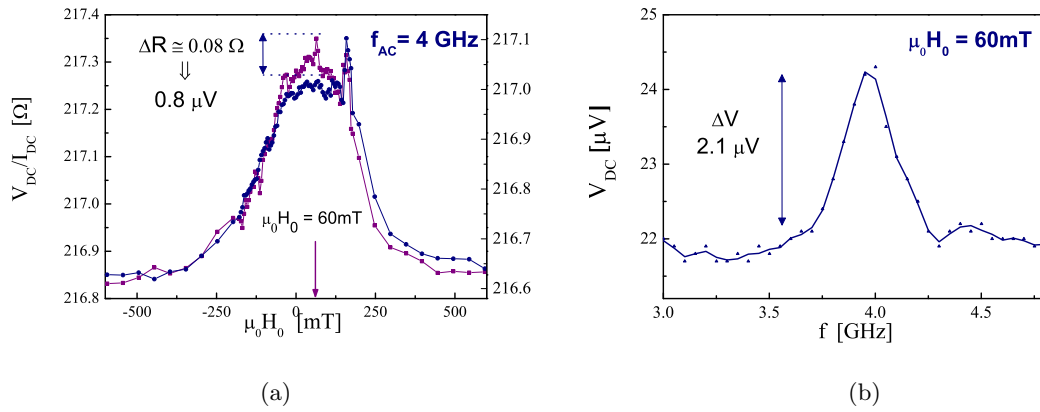


Figure 4.14 – PSV1: V_{DC}/I_{DC} detection of magnetization precession. (a) Superposition of the V_{DC}/I_{DC} signal detected in the absence of microwave current (blue circles) and in the presence of a current of about $400\mu\text{A}$ at the frequency $\omega/2\pi = 4\text{ GHz}$ (purple squares). (b) V_{DC} trace recorded at $\mu_0 H_0 = 60\text{ mT}$. The spectrum evidences a peak at $f = 4\text{ GHz}$ which corresponds to the excitation detected in the V_{DC}/I_{DC} measurement.

4.5 Conclusions

As a general result of this dynamical study we can mention the complex spin dynamics observed in an individual nanomagnet of particularly reduced dimensions. The main features evidenced in our experiment are:

- **Uniform modes of both magnetic layers** We identify the fundamental modes of both magnetic layers and we evidence the different evolution of these eigenmodes in the two field configurations \mathbf{H}_\perp and \mathbf{H}_\parallel . Our assumptions about the nature of these excitations are supported by macrospin simulations of the FMR eigenmodes of both magnetic layers.
- **Higher order modes** We distinguish dynamical modes at higher frequency which present the same frequency dependence of lower uniform modes. These excitations are interpreted as higher order spin waves characterized by a spatial non-uniformity. With the support of some simple symmetry consideration we conclude that these spin wave excitations are of even index (i.e. they have a odd symmetry).

The signals identified as uniform excitations were analyzed in more detail and their shape is discussed in details and compared with what is expected from the analytical expression of the V_{DC} signal. Moreover, with the support of our macrospin simulations we identified some anomalies in the spectra (negative sign of peak A_\perp) and we suggest a possible mechanism of dynamic coupling between the layers which could account for these unexpected features. Finally, starting from the asymmetry observed between $H_0 > 0$ and $H_0 < 0$ for some selected excitations, we suggest a possible role of the rf Oersted field in triggering the STT excitations.

Switching field modulation by means of an AC current

This chapter is devoted to the study of microwave current-assisted switching in SV-like devices. A microwave current is used to induce the non linear dynamics in an electrodeposited pseudo spin valve structure. Room temperature measurements show the effectiveness of this technique in tuning the static switching field of both magnetic layers independently. It is shown that the injection of a continuous microwave current of about $100\ \mu A$ permits a shift of the switching field of a few tens of mT . The resonant character of the phenomenon is evidenced by a strong frequency-dependence of the efficiency of the current. The results of this experiment look particularly interesting for the prospect of technological applications such as devices for magnetic sensing. Indeed the possibility to adjust the value of switching field would permit us to tune the range of sensitivity of magnetic sensors or in general the working region of systems exploiting the static magnetic properties of nanomagnets (eg. MRAM and other storage devices).

5.1 State of the art and motivations

In recent years the use of non-linear excitations to trigger magnetization reversal has been the subject of numerous theoretical and experimental studies [77, 79–81]. The experimental implementation of microwave assisted switching can be realized by adding to a static magnetic field a radio frequency (rf) field with a defined frequency and geometry. It has been shown that a small amplitude rf field at a frequency resonant with the precessional mode of magnetization can significantly lower the static field needed to reverse the magnetization. Thirion *et al.* observed a reduction of the switching field as large as $100\ mT$ by applying short rf field pulses of the order of a few mT [77]. The mechanism behind

microwave assisted switching is not trivial and is still under discussion. In a simple double well system the effect of the static field can be viewed as a reduction of the potential barrier which traps the magnetization in its metastable state. The additional rf field does not modify the energy wells, but under some specific conditions, it can act as an energy source and give to the magnetic moment the energy necessary to overcome the potential barrier and escape from its local minimum. The switching happens through a mechanism of *nucleation-propagation-relaxation* of a large angle precession of the magnetization. The reversal is possible when the energy transfer between the rf field and the magnetization is enough to balance and overcome the energy dissipation (i.e. to balance the damping). The efficiency of this energy transfer depends on the resonant character of the rf field and on its specific geometry (i.e. circular or linear polarization and orientation with respect to the static field).

Microwave assisted switching presents several advantages with respect to quasistatic switching [29]. First, the magnetization reversal becomes faster and less power consuming (as we lower the static switching field). Secondly, it gives the possibility to tune the switching field of magnetoresistive (MR) devices. All these aspects are extremely important for the prospect of applications such as magnetic memories, magnetic field sensors and logic devices. One of the critical aspects of this switching mechanism is the possibility of ringing and switching back of the magnetization. In order to perform an efficient reversal and avoid multiple subsequent switchings it becomes crucial to tune the pulse duration [77]. An added difficulty is the technological implementation due to the need for rf field pulses of well defined duration and geometry.

Microwave current as trigger of precessional switching The possibility to drive magnetization dynamics and/or switching by means of a high density current (i.e. via STT) constitutes an interesting alternative to field-induced processes. One of the advantages of STT is the lower power consumption associated with the use of electrical currents compared to field-induced excitations. Recent experimental works have shown that a resonant microwave current can significantly alter the process of magnetization switching driven by a high density current [82, 83]. The STT is known to induce the magnetization reversal via *precessional switching* [42, 84, 85]. In the pre-switching region the gradual increase of the DC current amplitude implies a progressive amplification of the precession angle and, above a certain critical amplitude of the current (I_{crit}), the switching of the magnetization. A resonant microwave current has been proven to be more efficient than a DC current in enlarging the precession angle and then in triggering the magnetization reversal [83]. If, for example, we fix the direction of the DC current as in fig.5.1 (a), the STT on the magnetization of the thin magnetic layer always acts to push it closer to the magnetization of the thick layer. If the angle of precession is smaller than the offset angle between the two magnetizations the action of the STT is to increase the precession angle when the magnetization is traveling in the half orbit closer to \mathbf{M}_{Thick} and to decrease it for the other half

period of oscillation (fig.5.1 (a)). The STT induced by a resonant microwave current, on the contrary, reverses its sign every half period of precession, acting always to enlarge the orbit of oscillation (fig.5.1 (b)). This simplified picture can explain the higher efficiency of AC STT in triggering the precessional switching. It has been shown that by applying microwave current pulses the critical current of STT-induced switching can be significantly reduced and the switching can be performed with a significantly lower power consumption [82, 83].

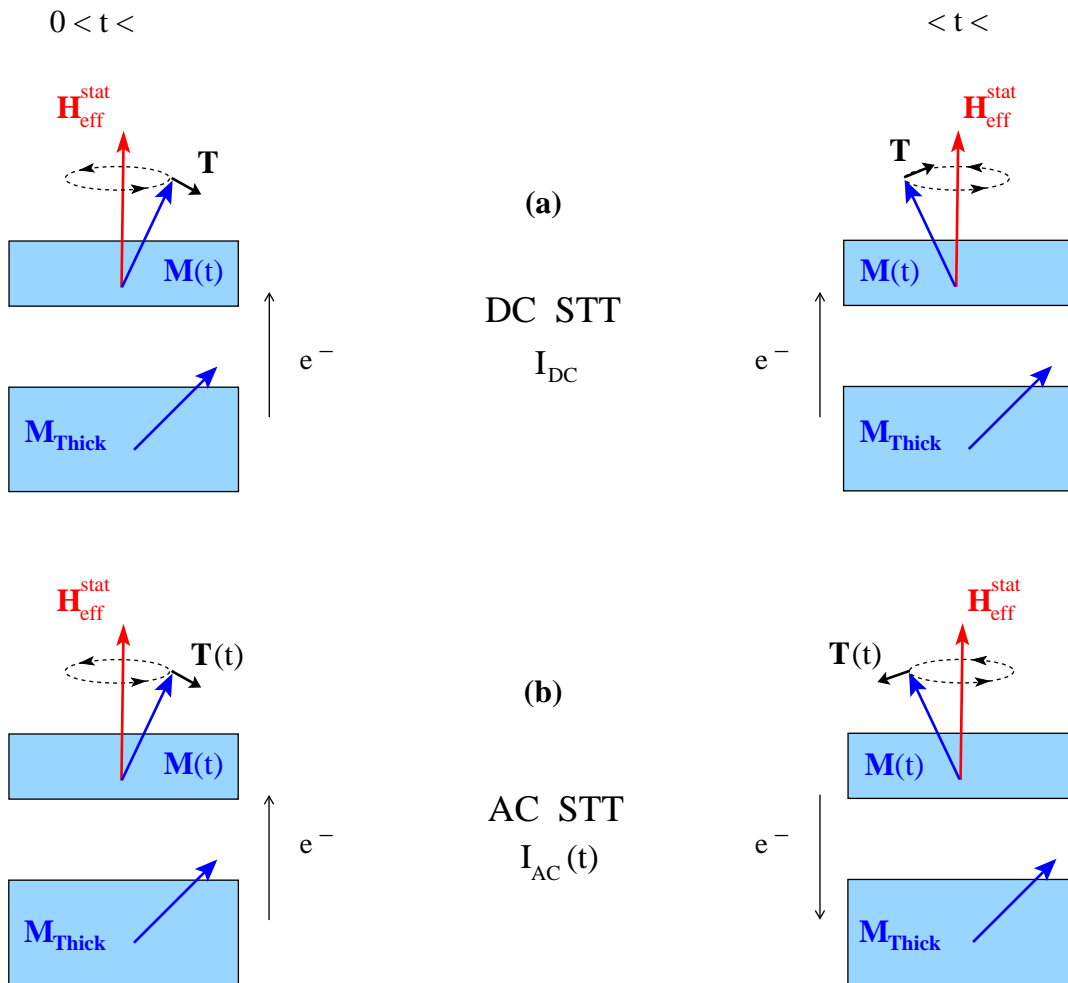


Figure 5.1 – AC STT vs DC STT: Simple schematic comparing the effect of a DC and an AC current on a spin valve device (panel (a) and (b) respectively). Note that the sign of the DC STT is constant over the period (τ) of the magnetization precession. The AC STT reverses its sign as soon as the magnetization moves from one half orbit to the other half. Therefore the AC STT always acts to enlarge the precession angle and is then more efficient as a trigger of precessional switching.

Objectives of the experiments Knowing all the advantages of STT over field induced-processes we want to perform microwave assisted switching by substituting the rf magnetic field with a microwave current. We profit from the AC STT to induce the non-linear dynamics of the magnetization and then to lower the static switching field H^{SW} of the magnetic layers of a pseudo spin valve device. The low power consumption typical of the STT effect and the ease of technological implementation make the use of a microwave current more attractive than classical microwave assisted switching (i.e. induced by an rf magnetic field).

5.2 Experimental protocol

The switching field of our samples is determined by a GMR measurement with the experimental set-up described in chapter 3 sec.3.3 (a schematic of the set-up is shown in fig.3.4 on page 55). The sample resistance is measured with a standard lock-in technique by injecting a square wave current at 413 Hz with a peak to peak amplitude of $20\ \mu\text{A}$. The magnetic field is scanned by steps of 2.4 mT taken every 10 s , hence in a quasistatic regime. The high frequency channel of a T-bias permits a microwave current (I_{AC}) to be injected simultaneously. The GMR is recorded alternately with and without I_{AC} , in order to verify that all the effects observed are reversible and not attributable to an alteration of the sample (possibly due to thermal effects or displacement of the electrical contact). The reproducibility of the GMR curves is verified by repeating ten times any pair of scans (GMR with and without I_{AC}). The complete set of measurements is repeated varying the frequency (f_{AC}) of the microwave current, in order to check the possible role of the frequency in the magnetization excitation. The typical amplitude of I_{AC} is $100 - 200\ \mu\text{A}$ and its frequency is scanned between 1 and 18 GHz. In this range of amplitude of I_{AC} the Joule heating induces a non-negligible increase of the effective temperature in the nanowire, as showed by the rise of the DC resistance of the sample ($\Delta R_{Joule} \sim 1 - 2\ \Omega$). The quasistatic character of our measurement makes thermal effects relevant in the trigger of precessional switching ($\tau_{meas} \gg \tau_{th}$ with τ_{meas} interval of time of each measurement and $\tau_{th} \sim 1\text{ ns}$ the characteristic timescale of thermal effects). We expect the increase of thermal fluctuations due to the injection of I_{AC} to vary the thermal contribution to the assisted switching and hence to introduce an artefact in our measurements (see the following section for details about the "weight" of thermally assisted switching in our experiment). In order to discriminate between thermal and STT effects we perform all measurements at constant Joule heating. The power delivered by the microwave source is adjusted for each value of f_{AC} in order to maintain the same ΔR_{Joule} for the whole set of measurements. In that way thermal effects are kept constant for all GMR scans under I_{AC} . This procedure permits us to associate all

discrepancies between scans at different frequencies to the frequency-dependent efficiency of the spin torque effect. Note that in contrast to the V_{DC}/I_{DC} detection adopted for the study of FMR excitations here the lock-in detection permits a pure measurement of the resistance.

5.2.1 Role of thermal effects

At a temperature $T \neq 0$ thermal fluctuations help the magnetization to overcome the energy barrier between two metastable states and they assist the switching. A quantification of this thermally assisted phenomenon is given by the *Néel-Brown* model which defines a temperature-dependent switching probability [86]:

$$\begin{aligned} P(t) &= e^{-t/\tau} \\ \tau &= \tau_0 e^{E(H)/k_B T} \\ E(H) &= E_0 \left(1 - \frac{H}{H_0^{SW}} \right)^\alpha \end{aligned} \quad (5.1)$$

where H_0^{SW} is the switching field at $T_0 = 0K$, E_0 is the value of the energy barrier between the two metastable states extrapolated to zero temperature and $E(H)$ is its value in the presence of the static magnetic field H . The factor α is known to be 1.5, unless the magnetic field is applied along an anisotropy axis of the system [54]. τ_0 is the inverse of an attempt frequency and is of the order of 10^{-9} s, t is the time and T the temperature. We note that due to the stochastic nature of thermally activated phenomena it is more appropriate to speak of the *most probable* switching field. The effect of thermal fluctuations is to broaden the distribution of switching fields and to lower its most probable value. The residence time in a metastable state can be written in the form of the Néel-Brown law [54]:

$$\tau = \tau_0 \exp \left[\frac{E_0}{k_B T} \left(1 - \frac{H}{H_0^{SW}} \right)^\alpha \right] \quad (5.2)$$

We have already mentioned that we expect the Joule heating in our samples to induce a non-negligible variation of the switching probability $P(t)$. We want to give here an estimate of this effect, therefore we are interested in calculating the variation of the switching field (ΔH_{th}) induced by a certain increase of temperature ΔT . If the initial temperature of our sample is set to be T_1 from the expression 5.2 we obtain:

$$\Delta H_{th} = -H_0^{SW} \left(\frac{k_B (\ln \tau - \ln \tau_0)}{E_0} \right)^{\frac{1}{\alpha}} \left[(T_1 + \Delta T)^{\frac{1}{\alpha}} - T_1^{\frac{1}{\alpha}} \right] \quad (5.3)$$

where τ is determined by the characteristic time of our measurement ($\tau_{meas} \sim 60$ s). We have to estimate ΔT , the increase of temperature induced by the Joule heating in the magnetic layers of our spin valve structure. This can be done by relating the power dissipated in the Co layers to a temperature gradient. We note that, due to the higher resistivity of

the Co ($\rho_{Co} \simeq 10^{-7}\Omega m$ and $\rho_{Cu} \simeq 1.72 \cdot 10^{-8}\Omega m$) the effective increase of temperature in the Co layers (ΔT_{Co}) would be higher than the average ΔT in the nanowire. The energy is

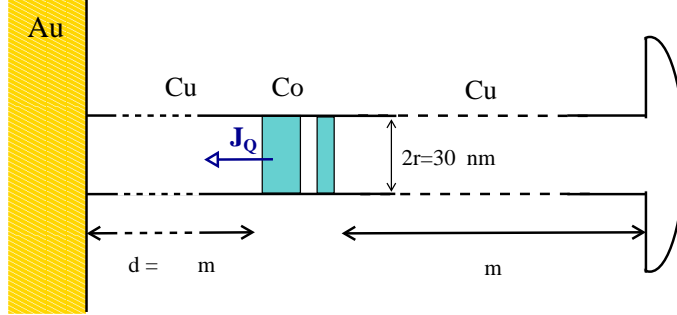


Figure 5.2 – Sketch of the Co/Cu nanowire. Due to the proximity of the massive Au layer to the Co layers it is reasonable to imagine that the heat current J_Q flows preferentially in this direction, as indicated by the arrow in the picture.

dissipated through a heat current J_Q generated by the gradient of temperature ∇T between the hot Co layer and the massive leads that can be considered anchored at the cryostat temperature. The heat is dissipated mostly through the copper nanowire to which the spin valve is connected. Hence:

$$\begin{aligned} J_Q \pi r^2 &= \rho_{Co} \frac{d}{\pi r^2} I_0^2 \\ &= K \nabla T \pi r^2 \end{aligned} \quad (5.4)$$

where $K = 10 W(mk)^{-1}$ is the heat conductivity, r is the radius of the nanowire and d is the thickness of the Co layer. I_0 is the amplitude of the current which induced the Joule heating (rms amplitude in the case of a microwave current). In our samples the magnetic structure is located at one extremity of the nanowire and it is reasonable to imagine that the dissipation is preferentially towards the massive Au layer sputtered on the bottom of the membrane (see sketch in fig.5.2). We have:

$$\Delta T_{Co} \simeq d \nabla T \quad (5.5)$$

where d indicates the distance between the Co layer and the massive Au, as depicted in fig.5.2. With these approximations we find an effective $\Delta T_{Co} \simeq 8K$ for the thick Co layer in the presence of $I_{AC} = 100\mu A$. With $E_0/k_B = 4000 K$, $H_0^{SW} = 140 mT$ and $T_1 = 300K$ we deduce a variation of the mean switching field $\Delta H^{SW} = 3.7 mT$ (E_0 and H_0^{SW} are deduced from a previous study in the group [87]).

5.3 Experimental results

We present the results obtained on two Pseudo Spin Valve (PSV) nanostructures electrodeposited in distinct templates. The samples have been measured in two different field configurations:

- PSV4: $\varnothing = 30 \text{ nm}$ $\text{Co}_{(20\text{nm})}/\text{Cu}_{(5\text{nm})}/\text{Co}_{(5\text{nm})}$, \mathbf{H}_0 applied out of the plane of the layers and scanned from negative to positive values;
- PSV5: $\varnothing = 30 \text{ nm}$ $\text{Co}_{(40\text{nm})}/\text{Cu}_{(5\text{nm})}/\text{Co}_{(10\text{nm})}$, \mathbf{H}_0 applied approximately in the plane of the layers and scanned from positive to negative values;

We recall that the uncertainty in the field orientation derives from two effects : the pores are uniformly distributed in direction within a cone of 30 degrees and furthermore, the layer itself may not be normal to the axis of the pore. A characterization of the magnetoresistance vs the orientation of the external field would allow us to determine the real plane of the layers. The instability of the electrical contact to a nanowire prevents from the realization of this set of measurements. Indeed the contact to a nanostructure is easily lost when turning the sample-holder into the poles of the magnet. Moreover, the short "life-time" of the contact prevents from an in-plane and out-of-plane characterization of the same nanowire. We will refer to the Co layer with the lower switching field as the *soft layer* and to the other one as the *hard layer*. We define H_1^{SW} and H_2^{SW} as the most probable switching fields of these two layers respectively.

5.3.1 PSV4 - \mathbf{H}_0 out of plane

The GMR of PSV4 is shown in fig.5.3 for H_0 scanned from negative to positive values (R_{up}) and backwards to negative saturation (R_{down}). The average resistance R_0 is 160.63Ω and the maximum ΔR is of about 0.51Ω ($\Delta R_{MAX} = R_{AP} - R_P$). In the following we will refer to the R_{up} curve as all GMR scans under I_{AC} have been recorded with this protocol. The GMR presents a first abrupt change at 52 mT corresponding to the switching of the softer magnetic layer from the parallel to the antiparallel configuration ($R_P \rightarrow R_{AP}$). Then the hard magnetic layer starts to rotate implying a gradual decrease of the resistance and it switches parallel to \mathbf{H}_0 at 115 mT ($R_{AP} \rightarrow R_P$). Due to its stronger in-plane anisotropy we assume the thin Co layer to be the magnetically harder in this field configuration. Therefore we identify the soft and hard layers with the thick and thin Co layers respectively. A switching field of 115 mT for the thin Co layer seems quite low. This value can be justified by considering that a canted angle could exist between \mathbf{H}_0 and the normal to the template.

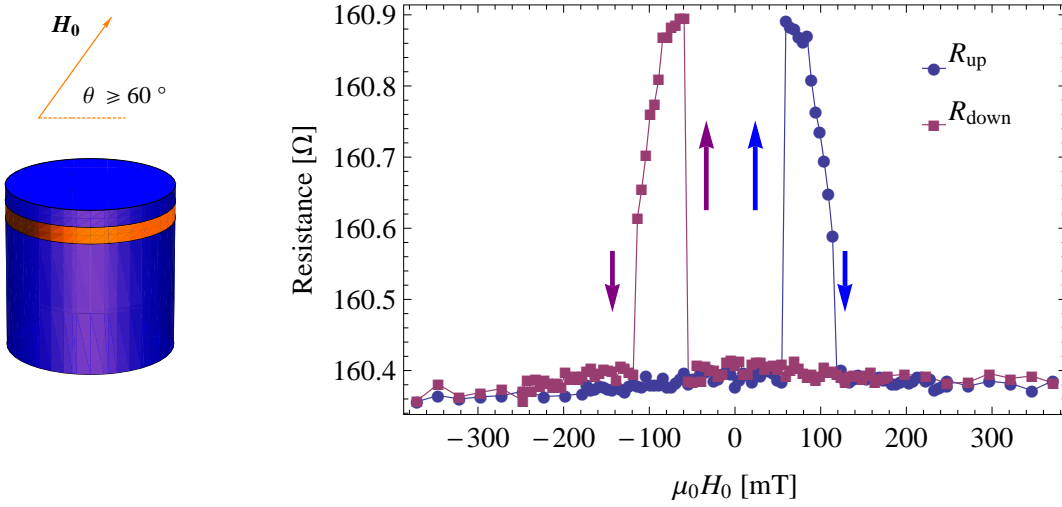


Figure 5.3 – PSV4: GMR curve recorded with \mathbf{H}_0 out of plane of the magnetic layers ($\theta > 60^\circ$). **(a)** cartoon of the sample structure and field configuration. **(b)** GMR curve recorded with a standard lock-in technique. H_0 is swept from negative to positive values (blue circles) and back to negative saturation (purple squares).

Macrospin simulations show that a canted angle of 60° can account for such a low switching field.

In figure 5.4 we show a set of GMR scans acquired with I_{AC} at a few different frequencies ranging from 1 to 16 GHz. In order to make the data more legible each GMR scan is re-scaled with respect to the value of the resistance at saturation field (R_S). The scan without any I_{AC} (GMR_0) is represented by black circles. The amplitude of I_{AC} is set at each frequency to obtain a $\Delta R_{\text{Joule}} \simeq 0.6 \Omega$. From a comparison with DC-induced Joule heating we deduce for I_{AC} an effective rms amplitude of about $100 \mu A$ (current transmitted into the nanowire). In our set of measurements (ten scans for each f_{AC}) we found evidence of non reproducible variations of both H_1^{SW} and H_2^{SW} of 5.8 mT and 2.4 mT respectively (i.e. two and one increments of the field sweep). The switching field reduction due to thermal fluctuations is assumed to explain these stochastic oscillations of the H^{SW} ($\Delta H_{th} \simeq 3.7 \text{ mT}$ and 1 mT for the thick and the thin layer respectively). Depending on the value of f_{AC} we observe significant changes of both switching fields, well above the uncertainty introduced by thermal effects. In particular for $f_{AC} = 1, 2, 3, 8$ and 11 GHz , H_2^{SW} is drastically reduced by a few tens of mT (data at 2 GHz not shown here). For some other frequencies (e.g. $f_{AC} = 16 \text{ GHz}$) the STT is totally inefficient on both layers and the GMR curve superposes on the GMR_0 .

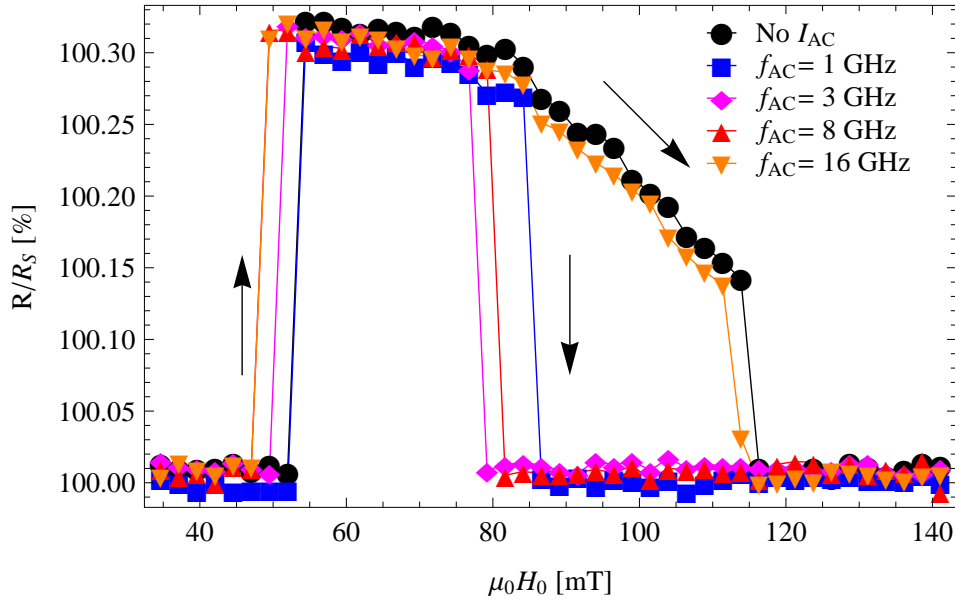


Figure 5.4 – PSV4: GMR scans with $I_{AC}(f)$ at several different frequencies. The direction of the field scan is indicated by the arrows. We observe big changes in the switching field of the thin Co layer for selected values of f_{AC} . All changes $< 4\text{ mT}$ are attributed to the effect of thermal fluctuations and can be neglected.

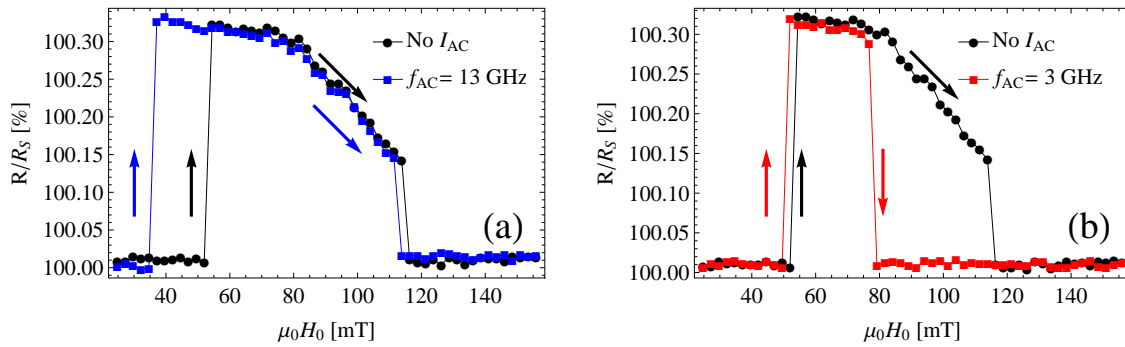


Figure 5.5 – PSV4: GMR scans with and without I_{AC} at 13 GHz (a) and 3 GHz (b). The arrows on the graphs indicate the direction of the field scan from negative to positive values. It is clear that the frequency plays a role in selecting which layer is assisted in the switching.

The frequency dependence of the effect is stressed in figure 5.5, where we show the GMR scans under I_{AC} at $f_{AC} = 13\text{ GHz}$ (a) and 3 GHz (b). At $f_{AC} = 13\text{ GHz}$ H_1^{SW} is decreased from 55 to 37 mT and H_2^{SW} does not change significantly. This suggests that at this

frequency the STT has a higher efficiency on the thick Co layer and it does not excite the dynamics of the thin layer. For $f_{AC} = 3\text{ GHz}$ H_1^{SW} is almost unchanged while H_2^{SW} is reduced from 115 to about 80 mT. We deduce that in this case the layer which is more sensitive to STT excitations is the thin one. A global overview of the switching field variation of the thin (black squares) and thick layers (red circles) is given in fig.5.10, panel (a). At $f_{AC} = 11\text{ GHz}$ we measured two different values of the switching field of the thin layer, indicated with two distinct points on the graph. Over the ten GMR scans done at this frequency we twice obtained $\Delta H_2^{SW} = 27 \pm 2\text{ mT}$ and eight times $\Delta H_2^{SW} = 45 \pm 2\text{ mT}$ (data shown in fig.5.6).

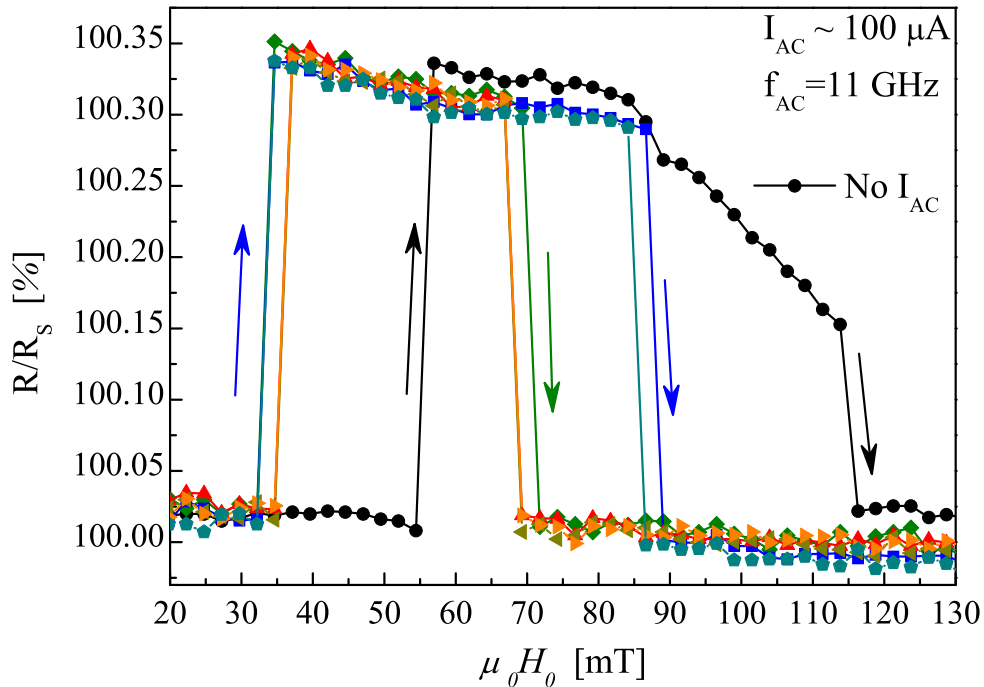


Figure 5.6 – PSV4: GMR scans with $f_{AC} = 11\text{ GHz}$ (we show here 4 representative examples over the 10 scans recorded). We observe that at this frequency the STT assists the reversal of both magnetic layers. H_1^{SW} is reduced to about 32 mT while H_2^{SW} is 70 or 88 mT depending on the specific GMR scan.

Comparison with the effect of a DC current

In order to compare the effect of a DC and a microwave current we recorded the GMR under a high density DC current. We injected a current $I_{DC} = \pm 190\mu\text{A}$, where the minus sign corresponds to a flow of electrons from the thick to the thin layer, favoring an alignment of the thin magnetic layer parallel to the magnetization of the thick one. This current

amplitude induces a $\Delta R_{Joule} \simeq 2\Omega$ which is more than twice the Joule heating induced by the I_{AC} used in the experiment. This confirms the higher amplitude of I_{DC} with respect to I_{AC} (estimated as $\sim 100\mu A$ rms). In fig.5.7 we show the GMR recorded with $\pm I_{DC}$

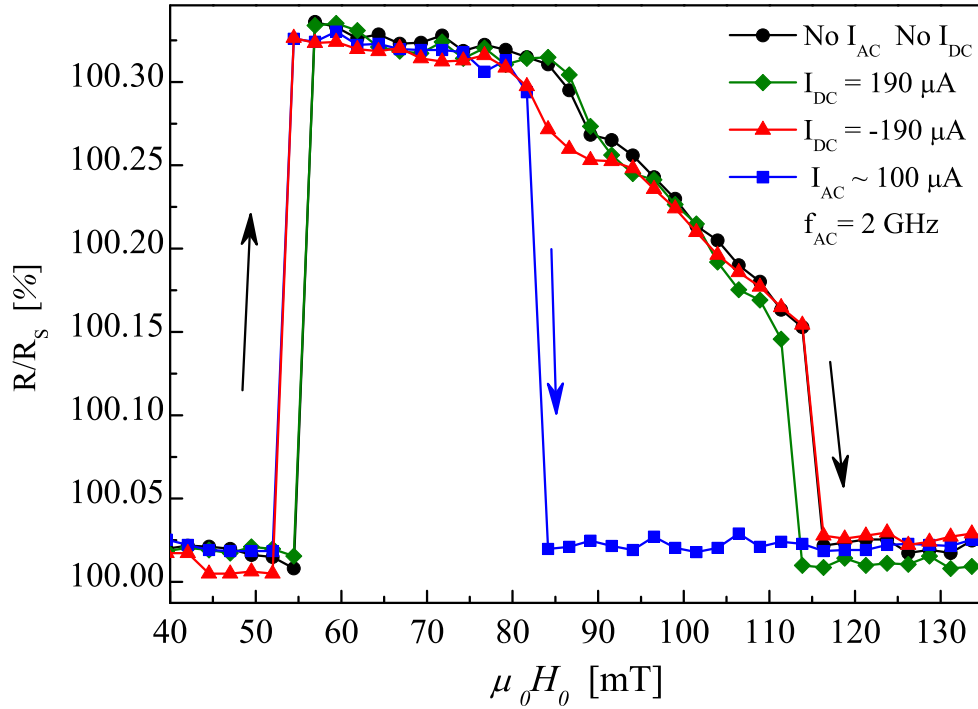


Figure 5.7 – PSV4: GMR scans with and without an additional AC or DC current. The arrows indicate the direction of the field scan. The scan under $I_{AC} \sim 100\mu A$ evidences a strong reduction of the switching field of the thin layer. The two scans realized at positive and negative I_{DC} at $190\mu A$ do not show any significant change in the switching fields.

compared with the GMR_0 scan (black circles). Apart from small discrepancies consistent with the uncertainty introduced by thermal fluctuations, I_{DC} does not imply any change in the switching field of any of the magnetic layers. For a direct comparison, in the same plot is shown the GMR recorded for I_{AC} at 2 GHz (blue squares). This measurement brings a direct evidence of the better efficiency of AC STT in triggering the switching and reducing the static switching field.

5.3.2 PSV5 - H_0 in plane

The GMR of PSV5 recorded without any additional I_{AC} (GMR_0) is shown in fig.5.8 and the arrows indicate the direction of the field scan of each curve. The sample presents an average resistance $R_0 = 157.6\Omega$ and a $\Delta R_{MAX} \simeq 0.5\Omega$. The acquisitions under I_{AC} have

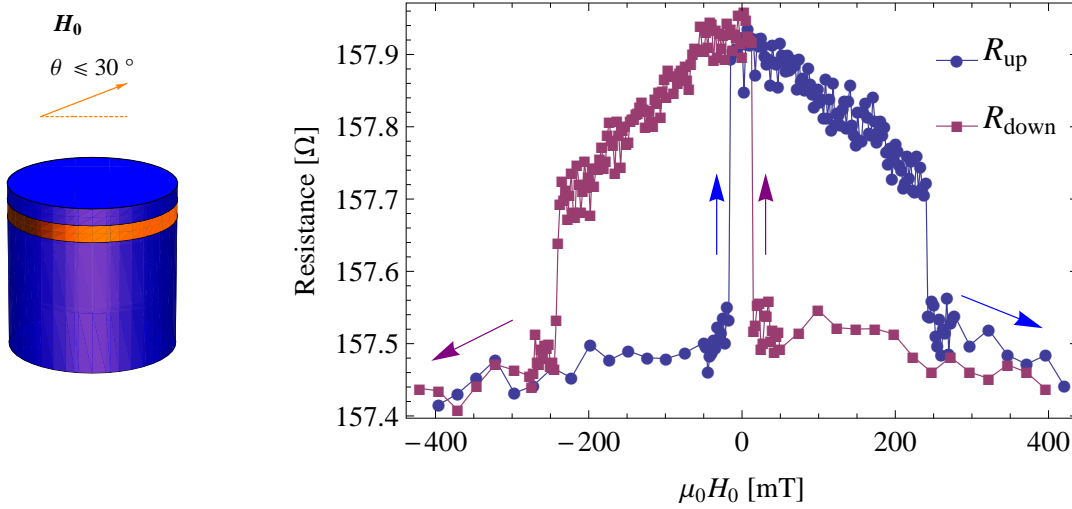


Figure 5.8 – PSV5: GMR curve recorded with \mathbf{H}_0 approximately in the plane of magnetic layers. **(a)** cartoon of the sample structure and field configuration. **(b)** GMR curve recorded with a standard lock-in technique. The arrows indicate the direction of the field scan: from negative to positive values (blue circles) and back to negative saturation (purple squares).

been done for H_0 swept from positive to negative values. Therefore in the description of GMR_0 we will refer to the R_{down} scan (purple squares in fig.5.8). We note that the soft magnetic layer switches slightly before the inversion of the magnetic field, hence the effective field must be antiparallel to \mathbf{H}_0 ($H_1^{SW} = 14 \text{ mT}$). This reflects the effect of the dipolar coupling between layers. When the effect of the dipolar coupling becomes predominant over the external field \mathbf{H}_0 , the effective field reverses its sign (\mathbf{H}_{eff} almost antiparallel to \mathbf{H}_0) and the magnetization of the soft layer switches antiparallel to \mathbf{H}_0 . We expect the thin layer to be subjected to stronger dipolar coupling hence we identify it with the soft magnetic layer. After the jump at H_1^{SW} the GMR decreases smoothly, indicating a gradual variation of the magnetic configuration. At $H_2^{SW} = -230 \text{ mT}$ the hard layer, identified here with the thick one, switches along the field direction. In fig.5.9 we show some GMR curves acquired under I_{AC} excitation (data re-scaled to R_S). The AC current induces a ΔR_{Joule} of about 2Ω corresponding to an effective rms amplitude of about $200 \mu A$ (data relative to the calibration not shown here). The amplitude of the current was increased to $200 \mu A$ because for the same rms amplitude used in the previous sample we did not observe any reproducible effect of assisted switching. This current amplitude induces an effective ΔT of about 8.4 K and 32 K for the thin and the thick Co layer respectively. Therefore, independent of the frequency of I_{AC} , we could observe a reduction of the switching field of about 4 mT for the thin layer and up to 15 mT for the thick one. The GMR scans indicate

a dramatic decrease of H_1^{SW} for $f_{AC} = 2$ and 11 GHz, while the switching field of the thick layer is unchanged (ΔH_2^{SW} is below the variations expected due to thermal fluctuations). This reflects the lower efficiency of STT on the thick Co layer. In fig.5.10 (b) is shown

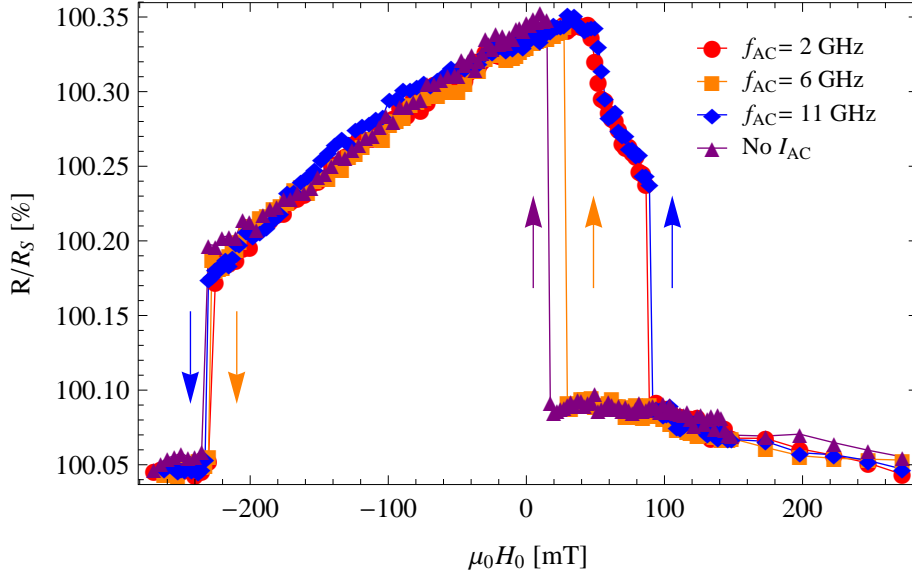


Figure 5.9 – PSV5: GMR with and without I_{AC} at different frequencies. Scan with \mathbf{H}_0 approximately in the plane of the magnetic layers and swept from positive to negative values.

the trend of the switching field variations as a function of the frequency of I_{AC} (data for to the thin layer). The large error bars correspond to the spread of ΔH^{SW} measured at each frequency. These big fluctuations of the switching field are only in part explained by thermal fluctuations ($\Delta H_{th} \simeq 4$ mT). The two points at $f_{AC} = 11$ GHz indicate the two different values of ΔH_1^{SW} observed at that frequency. Three scans out of ten gave a $\Delta H_1^{SW} = 15$ mT and in the other seven scans we measured $\Delta H_1^{SW} = 80$ mT.

5.4 Discussion of the results

We summarize here the effects observed in our experiment and we interpret the strong frequency dependence of our data as the signature of a resonant effect. The large changes of the switching field are associated with the excitation of uniform precessional modes of the magnetization. Moreover, we suggest that higher order spin waves could explain the

stochastic behavior of the switching observed in both samples at $f_{AC} = 11 \text{ GHz}$. Finally we analyze the different parameters influencing the efficiency of the STT assisted switching.

5.4.1 ΔH^{SW} vs f_{AC} diagram

The variations of the switching field observed in the two samples are summarized by plotting the most probable value of ΔH_1^{SW} and ΔH_2^{SW} as a function of the frequency of the exciting current (fig.5.10). For the sample PSV5 only ΔH_1^{SW} is shown as it is the only switching field presenting significant changes. We recall that the thick magnetic layer corresponds to the soft layer (\mathbf{H}_1^{SW}) in the out-of-plane configuration (PSV4) and to the hard layer (\mathbf{H}_2^{SW}) in the in-plane configuration (PSV5). In the graphs of fig.5.10 we can identify some

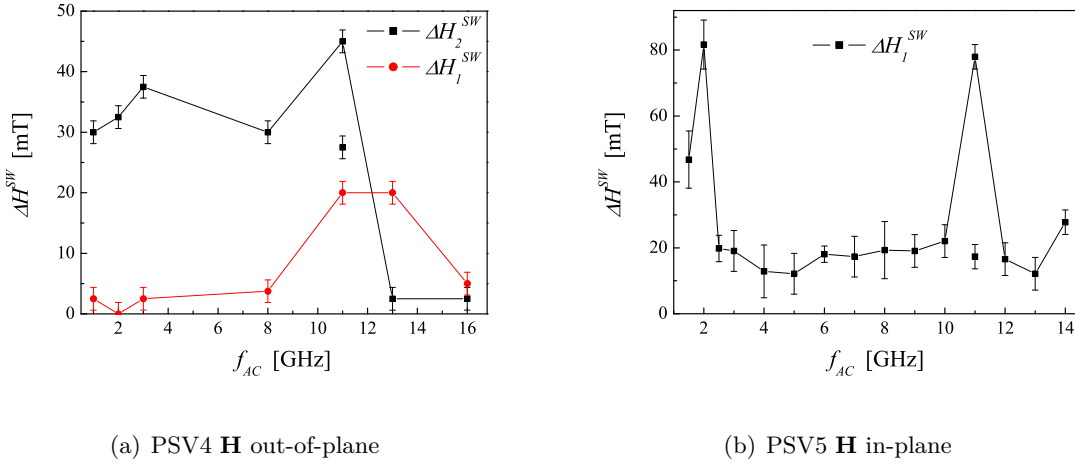


Figure 5.10 – ΔH^{SW} vs f_{AC} : diagram summarizing the behavior of (a) PSV4 and (b) PSV5. The error bars are fixed according to the width of the switching field distribution at each frequency (data deduced from ten GMR scans for each value of f_{AC}). Both graphs (a) and (b) indicate a strong frequency dependence of the switching field modulation. In panel (b) is shown only the variation of H_1^{SW} , as in this sample (PSV5) H_2^{SW} does not present significant variations.

selected frequencies for which the reduction of the switching field is more important. This is particularly evident in PSV5 where we observe a sharp increase of ΔH_1^{SW} for $f_{AC} = 1.5, 2$ and 11 GHz . In both samples we notice a significant difference in the behavior of the two magnetic layers. The switching field of the thinner layer presents strong variations for several different values of f_{AC} . The thick layer seems less sensitive to the effect of the microwave current and only in the case of PSV4 we observe relevant changes of its switching field. We can conclude that in both samples the microwave current is more effective in manipulating the switching field of the thin layer. Without entering into the discussion of the intrinsic precessional modes of the two layers this result can be explained by the nature of the STT excitation. Indeed, due to its larger volume, the thick layer is expected to be less affected by the STT effect than the thin one ($\mathbf{t}_{STT} \propto V_m^{-1}$). Our

results suggest that the spectrum of possible values of the switching field is discrete, i.e. the switching field can take some defined values, corresponding to magnetization reversals through different paths.

5.4.2 Nature of the excitations

Our results show that for some selected frequencies the microwave current is particularly efficient in assisting the switching of a specific magnetic layer. We expect these frequencies to correspond to spin wave eigenmodes of the layer. In the following section we compare the results of the assisted switching experiment on sample PSV5 to the dynamical spectrum of the nanostructure. We suggest that the most efficient frequencies in the trigger of the switching (i.e. $f_{AC} = 1.5, 2 \text{ GHz}$, see fig.5.10 (b)) correspond to a uniform excitation of the thin layer. Finally, we propose a possible explanation of the stochastic behavior observed for the switching field at $f_{AC} = 11 \text{ GHz}$, in both samples PSV4 and PSV5.

Comparison with the dynamical spectrum: uniform excitations

In fig.5.11 we show the dynamical modes of sample PSV5 as a function of the applied field (data deduced from $V_{DC}(\omega)$ spectra not shown here). The amplitude of the microwave current used to excite the magnetization precession is about $150 \mu A$. In the same graph we plot the GMR of the sample, acquired in the absence of a microwave current.

In the region prior to the switching of the thin magnetic layer ($H_0 \sim 100 - 40 \text{ mT}$) we detect several spin wave excitations. The more intense V_{DC} peaks correspond to the dots circled and indicated by the arrow. We expect this excitation to correspond to a uniform mode (U) of the thin layer. We observe that around 50 mT this mode changes dramatically its frequency dependence. This could indicate that the magnetization switches, due to the current induced precession. This indicates that at this amplitude of the current ($\sim 150 \mu A$) we are already in a non linear regime of excitation. We observe that the mode U is above the most efficient frequencies identified in the switching field experiment (i.e. $f_{AC} = 1.5, 2 \text{ GHz}$). Unfortunately the data below 3 GHz are missing, due to an arbitrary choice at the moment of the spectra acquisition. The reduced lifetime of the samples did not give the possibility to repeat the V_{DC} measurements with more relevant experimental parameters. When we compare the dynamical spectrum of the sample to the results of the assisted switching experiment we have to consider that as we move from small angle precessions to large angle precessions the dynamics of the system can change significantly. In particular precessional modes are not supposed to present the same characteristic frequencies of FMR eigenmodes. Indeed FMR frequencies are derived by the linearization of the LLG equation, assuming a small oscillating component of the magnetization. This assumption is clearly false in the case of large angle precessions and the LLG equation presents different solutions. Nonetheless, analytical calculations show that precessional modes present the same field

dependence of FMR excitations [88, 89]. In particular, the proportionality factor between the pulsation ω_p of the precessional modes and the FMR eigenmodes has been calculated to be inferior to one:

$$\omega_p \simeq 0.847\omega_{FMR} \quad (5.6)$$

The dynamical modes of fig.5.11 have been excited under a microwave current lower than the one used in the switching field experiment. Therefore we could expect a lower degree of non-linearity. It could be necessary to slightly rescale the frequencies of these dynamical excitations before comparing them to the most efficient frequencies in the assisted switching experiment. Finally, we observe that in the region of switching of the thick layer ($H_0 \sim -230mT$) we do not detect any spin wave excitation. This result confirms the lower efficiency of the STT on the thick layer and is in good agreement with what is observed in the switching field experiment.

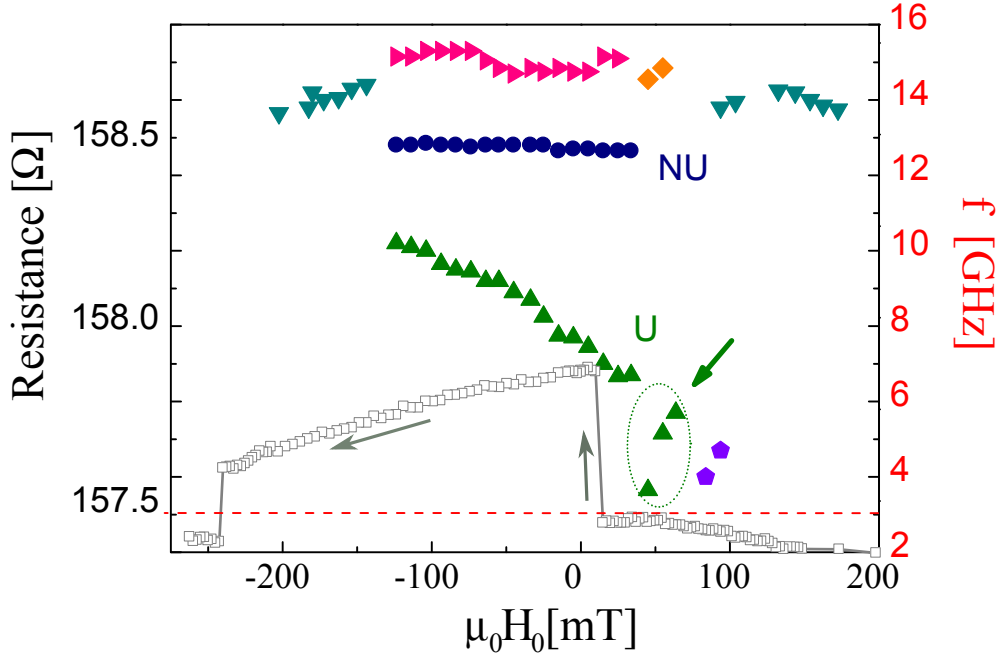


Figure 5.11 – PSV5: diagram of $f(H_0)$ Solid symbols: non uniform (N-U) and uniform (U) dynamical modes of the PSV detected via V_{DC} spectra. The data are recorded for a field swept from positive to negative saturation, under $I_{AC} \sim 150\mu A$. Gray open symbols: GMR scan without any additional microwave current.

Spatially non-uniform modes

Our results show that for some values of f_{AC} the reduction of the switching field seems to have a stochastic behavior ($f_{AC} = 11 GHz$ for both PSV4 and PSV5). A similar phe-

nomenon was observed by Tudosa *et al.* in the frame of an experiment on precessional switching induced by uniform rf field pulses[90]. The authors attribute the stochastic behavior of the switching field to the onset of spin wave instabilities due to incoherent fluctuations of the magnetization (following from the coupling of thermal fluctuations with the strong field pulses). We assume the onset of spin wave instabilities to also be the explanation of the observations in our samples. We observe that the non-deterministic reversal is at $f_{AC} = 11\text{GHz}$, thus it is at a high frequency already associated with a non-uniform excitation of the magnetization (see previous chapter). This high frequency mode is identifiable with the mode "N-U" in fig.5.11. It is intuitive from an oversimplified picture that the efficiency of the AC STT in amplifying such non-uniform oscillations is lower than in the case of uniform precessions. Indeed, the dephasing between the magnetization oscillation in the different areas of the layer prevents the AC STT from synchronizing with all the precessing spins (see fig.5.12). The AC STT seems to favor a "distortion" of the precessional mode, as it amplifies the precession only in some areas of the sample. The analysis of the STT amplification of high order spin waves and of their role in assisting the magnetization reversal is far to be trivial. For a detailed analysis of our data we need first to identify the spatial distribution of the mode at $f_{AC} = 11\text{GHz}$. However, due to the non-uniformity of the excitation and to the possible distortion induced by the AC STT we can expect the onset of a particularly complex spin dynamics. We could imagine this complex dynamical processes to result in a stochastic behavior of the switching field, in analogy with what is observed and modeled in Ref.[90] and [91].

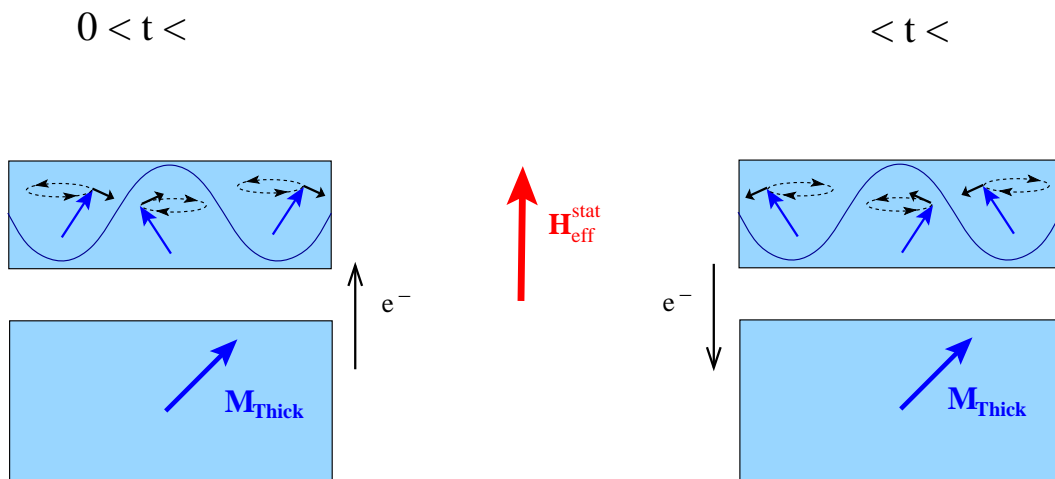


Figure 5.12 – Schematic of the AC STT effect on a non-uniform excitation of the magnetization. We observe that the torque acts to enlarge the angle of precession of only a portion of the spins.

5.4.3 STT efficiency

For the prospect of technological applications it is particularly important to evaluate the efficiency of STT-assisted switching. It is interesting to link the effectiveness of STT to a particular magnetic configuration or structure that can be mimicked in technological implementations. We have already pointed out the higher sensitivity of the thin magnetic layer to STT assisted switching. Therefore the first crucial point is the volume of the magnetic element. The smaller the volume, the smaller the current amplitude needed to switch it and therefore the smaller the associated power cost. We observe that the switching field of the thick magnetic layer is modified only in the case of sample PSV4. We can deduce that the magnetic configuration adopted for this sample is more favorable to the STT assisted switching. This result probably reflects the importance of the relative orientation of the magnetic layers in the efficiency of the assisted switching. In the case of the sample PSV4 the magnetic field is perpendicular to the plane of the layers, thus along an hard axis for the magnetization of the thin layer. We can imagine that as soon as we decrease the value of the field the thin layer tends to rotate in-plane while the thick layer maintains an higher out of plane component. This induces a misalignment of the magnetizations in the zone prior to the switching and enhances the efficiency of the STT. There is another important point to consider. Even if the STT is able to induce the magnetization precession if the angle of the precession is larger than the offset angle between the two magnetizations, the resonant amplification does not take place (see fig.5.13). Therefore an offset angle large

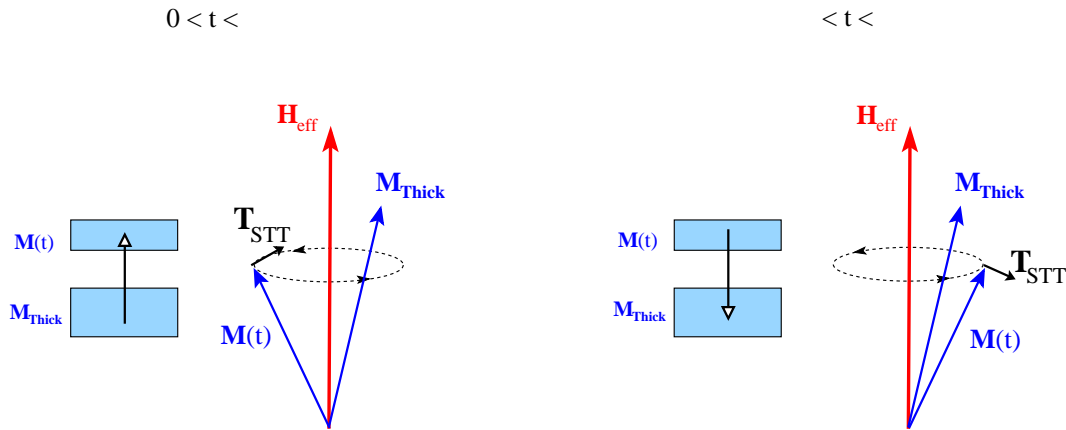


Figure 5.13 – Schematic of the AC STT effect in presence of a small offset angle between the two magnetizations. As the angle of the precession becomes larger than the angle of offset the resonant amplification of the precession is not possible anymore.

enough to permit the AC STT to excite the magnetization dynamics could preclude the efficient amplification of the precession and thus the assisted switching. If the magnetic field

is applied in-plane (case of sample PSV5) we expect the magnetizations to be closer to the antiparallel configuration and the STT to be less efficient. The importance of the relative orientation of the layers is confirmed by the numerical integration of the LLG equation including the STT term. We study the temporal evolution of the magnetization of the thin magnetic layer under a microwave current spin-polarized along the direction of the thick layer magnetization. This is described by the equation:

$$\begin{aligned} \frac{\partial \mathbf{M}(t)}{\partial t} = & -\mu_0 \gamma \mathbf{M}(t) \times \mathbf{H}_{eff} - \alpha \mathbf{M}(t) \times [\mu_0 \gamma \mathbf{M}(t) \times \mathbf{H}_{eff}] + \\ & + \frac{\gamma \hbar}{2eV_m} \frac{\mathcal{P}}{M_s} I_{AC} \mathbf{M}(t) \times (\mathbf{M}_{Thick} \times \mathbf{M}(t)) \end{aligned} \quad (5.7)$$

$$\begin{aligned} \mathbf{H}_{eff} &= H_0 \hat{y} + \overline{\overline{N}} \mathbf{M} \\ \mathcal{P} &= \left[(1 + P)^3 \frac{3 + \mathbf{m} \cdot \mathbf{p}}{4P^{3/2}} - 4 \right]^{-1} \\ P &= 0.4 \\ \mathbf{M}(t) &= -M_y \hat{y} \end{aligned}$$

$\mathbf{M}(t)$ indicates the magnetization of the thin layer and \mathbf{M}_{Thick} that of the thick layer which polarizes the current. \mathbf{H}_0 is the external static field and I_{AC} is the microwave current injected into the spin valve. We solve equation 5.7 by fixing the initial positions of \mathbf{M} and \mathbf{H}_0 as depicted in fig.5.15 (a) and varying the orientation of the thick layer. In fig.5.14 (a) we show the temporal evolution of the y component of the magnetization with and without I_{AC} for several values of H_0 . In fig.5.14 (b) we compare the magnetization evolution with and without the STT contribution. We observe that at $H_0 = 500 \text{ mT}$ the switching happens thanks to the effect of the AC STT and the magnetization evolution is almost equivalent to the effect of $H_0 = 512 \text{ mT}$ without microwave current. The STT assisted switching is then studied as a function of the offset angle between the two magnetizations (fig.5.15). The results confirm a strong dependence of the switching time on the relative orientation of the layers.

All these elements can help in the design of a magnetic sensor with a tunable range of sensitivity. We can conclude that it is convenient to have magnetic layers of particularly small volume and with a strong offset angle between their magnetizations. For example, the thick layer could be exchange coupled to an antiferromagnetic layer and fixed at a canted angle to the easy axis of the thin layer. From our simplified simulations we deduce that an offset angle of 65° is more convenient than a 90° angle.

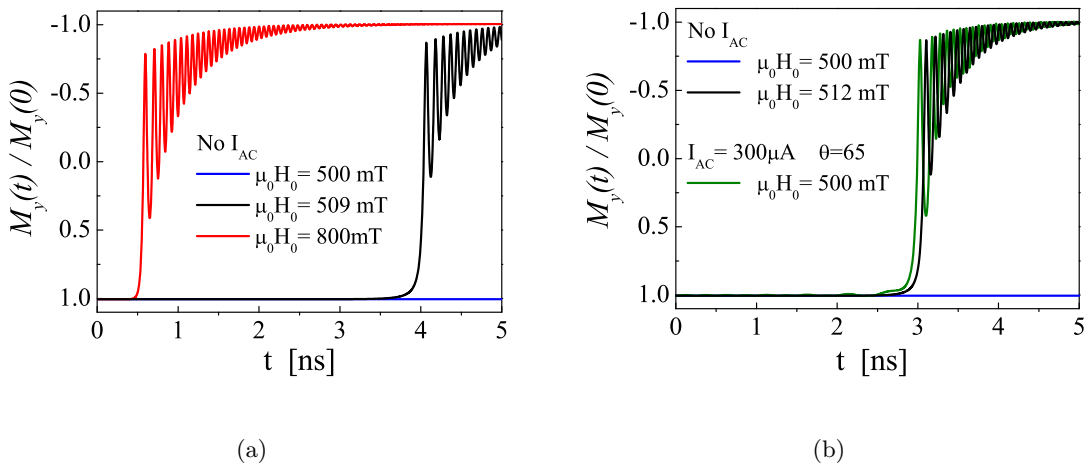


Figure 5.14 – Temporal evolution of the magnetization of a thin Co layer without (a) and with (b) the injection of a high density microwave current. We observe the role of the current in assisting the switching of the magnetization at magnetic fields inferior to the static switching field. In absence of a microwave current a field of 509 mT is needed to induce the magnetization switching within the temporal window of our simulation (panel (a)). When we add a microwave current of 300 mT the switching occurs at a lower value of the static magnetic field. The effect of this microwave current is similar to that of an additional field of 12 mT (see green and black curve in panel (a)). Data deduced by numerical integration of the modified LLG equation.

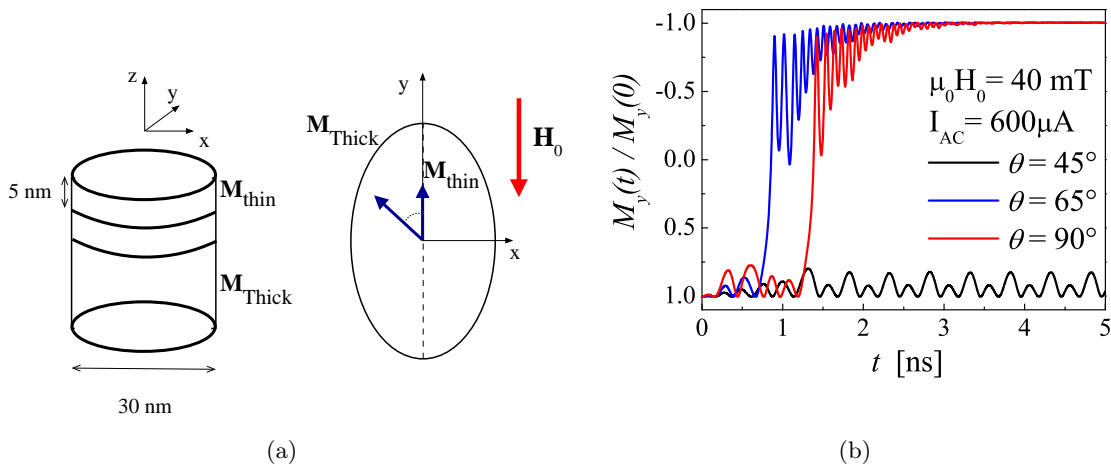


Figure 5.15 – (a) schematic of the thin Co layer, representing the orientation of the two magnetizations and of the magnetic field. (b) Temporal evolution of the thin layer magnetization under a microwave current. The data stress the dependence of the switching field on the relative orientation of the magnetic layers (angle θ).

5.5 Conclusions

The efficiency of a microwave current in assisting the magnetization reversal at room temperature is shown by recording the GMR of pseudo spin valve samples with and without an additional high density microwave current. Changes in the switching field of each layer are observed and attributed to the resonant coupling of precessional modes of the magnetic layer with the AC spin transfer torque. Our results prove the role of the excitation frequency f_{AC} , showing a strong frequency dependence of the switching field. Moreover, it is shown how the choice of the frequency can determine which layer is assisted in the switching. This permits each magnetic layer to be manipulated independently, yielding a further "degree of freedom", which can be useful in technological applications. Our experiments confirm the relevance of the relative orientation of the layers and of their magnetic volume in the efficiency of the STT assisted switching. These results contribute to defining the ideal design for the technological implementation of this form of assisted switching.

Conclusions and future perspectives

In this thesis we presented a study of spin dynamics in an individual pseudo spin valve device of particularly reduced dimensions ($\varnothing = 30\text{ nm}$). Our experiment focused on two different aspects of the dynamics: the intrinsic eigenmodes of the magnetization precession and the excitation of highly non-linear precessional modes which can assist the magnetization reversal.

We make use of a continuous microwave current to excite the spin dynamics of a pseudo spin valve structure. The precession of the magnetization is detected electrically. The magnetoresistance of the sample acts as a signal demodulator and converts the resonance of the magnetization into a continuous voltage. Therefore, part of the issue of circuit matching at high frequency can be avoided. The first characteristic of this technique is that it constitutes a local probe of the magnetization dynamics as it permits us to address a single nanostructure through the establishment of the electrical contact. Secondly, the sensitivity of the detection is not linked to the magnetic volume of the nanostructure but rather to its magnetoresistive percentage. These points make this method (i.e. electrical excitation and detection) particularly suitable for the study of the spin dynamics at the nanoscale.

We want to stress that all our measurements were done with the use of low cost techniques and commercially available materials. The samples are electrodeposited nanostructures realized in our laboratories. The electrical contact to an individual nanowire is made without the use of any lithography technique and allows several examples of magnetic nanowires in the same template to be studied. This technique is particularly flexible as it permits us to vary easily the number and the thickness of layers in a nanostructure. However, the uncertainty about the exact geometrical configuration of the magnetic layers (degree of ellipticity and orientation with respect to the template) introduces an additional complication in our experiment.

Our results show the effectiveness of the AC STT in exciting numerous dynamical modes in extremely small nanomagnets. The electrical detection gives a precise picture of the field-dependence of these spin wave excitations. Moreover, the dynamical spectra of our nanomagnets are similar to what was observed by others in arrays of nanomagnets slightly bigger than our structures. With the support of macrospin simulations we show that the microwave current excites the fundamental modes of both the thick and thin layer of the pseudo spin valve.

Starting from some symmetry considerations we identify the higher frequency modes of the spectrum with spatially non-uniform spin waves of odd symmetry. Moreover, we suggest the possible role of the Oersted field induced by the microwave current in the excitation of such spatially non-uniform modes. Finally, for some of the modes we identify a distortion of the V_{DC} signal with the inversion of the magnetic field. We propose a mechanism of triggering of the spin precession by the Oersted field as a possible explanation of this distortion.

We studied the effect of a continuous microwave current on the static switching field of the magnetic layers in our nanostructures. Our work on magnetization reversal assisted by a pure microwave current is, to our knowledge, the only one documented in the literature. This experiment is particularly relevant for the prospect of technological applications. Indeed, our results suggest that a microwave current could be used to tune the switching field of magnetic sensors and then to adjust their range of sensitivity without implying any technical modification of the device.

By comparing our results with the typical FMR frequencies in our nanomagnets we propose that the current-assisted switching is more efficient when the microwave current resonates with the fundamental mode. This assumption is supported by the fact that the AC STT is expected to be more effective in the amplification of uniform excitations. In the end we discuss the importance of the relative orientation of the layers and we suggest a possible design for a device suitable for current-assisted switching.

This thesis proves the suitability of our technique (i.e. electrodeposition plus electrical excitation and detection of spin dynamics) for spin dynamical studies on extremely small nanomagnets. In the perspective of future developments of this work we identify several possible improvements of both the data analysis and the experimental technique. First of all, micromagnetic simulations would be necessary for the identification of the higher order

modes of the spectra. Moreover, an improvement of our contacting technique is certainly needed as its mechanical instability reduces the lifetime of contacted nanostructures. A stable contact would permit us to realize magnetoresistive measurements at variable angle and to reduce the uncertainty in the field orientation. Experimental solutions to this issue such as picoprobe contacting and a rotating support for the magnet are presently under evaluation.

Moreover, we suggest repeating the experiment on a "real" spin valve structure made of a pinned and a free layer. Indeed, we observe that both the thick and the thin magnetic layers in our structure are free to precess. Our experiment evidenced the FMR modes of both layers and the occurrence of simultaneous oscillations of the magnetizations. This implies an additional complexity of the dynamical spectrum and in some cases makes difficult to distinguish the contributions of the two layers to the V_{DC} signal. The pinning of the thick Co layer would simplify the spectrum and help in its interpretation. Such a device can be realized by biasing the Co thick layer with a CoO or NiO bottom layer. A further step would be the fabrication of a bias-free spin valve by the deposition of a stacked structure of the kind CoFe/IrMn/CoFe/Cu/Co. These improvements would permit us to repeat the experiment with a well-defined field orientation and to realize a complete study of spin dynamics which includes a mapping of all the spin wave excitations in the spectrum.

Finally, we propose a further investigation of the possible coupling between precessing magnetizations. In this prospect we envisage the study of structures made of three magnetic layers: a pinned layer which acts as "current polarizer", a thin free layer and a third layer of variable thickness. The role of this third layer would be to introduce in our structure a dynamical dipolar field. This would permit us to study the possible effect of the dynamical coupling to the dynamics of the thin free layer and to relate it to the strength of the dipolar interaction (i.e. the thickness of the third layer and of the non magnetic spacer which separates it from the thin free layer).

Analytical solution of the LLG modified equation under AC STT

In this appendix we give an approximated solution of the Landau-Lifshitz-Gilbert (LLG) equation in presence of an oscillating spin torque term:

$$\frac{\partial \mathbf{M}(t)}{\partial t} = -\mu_0 \gamma \mathbf{M}(t) \times \mathbf{H}_{eff} + \alpha \mathbf{M}(t) \times \frac{\partial \mathbf{M}(t)}{\partial t} + \frac{\gamma \hbar}{2eV_m} \frac{\mathcal{P}}{M_S^2} I_0 e^{-i\omega t} \mathbf{M}(t) \times (\mathbf{p} \times \mathbf{M}(t)) \quad (\text{A.1})$$

where α is the damping coefficient, γ is the gyromagnetic ratio and \mathcal{P} is the *polarization function*. $\mathbf{M}(t)$ is the precessing magnetization and M_S is its value at the saturation, \mathbf{H}_{eff} is the effective magnetic field. \mathbf{p} is the direction of the polarizing magnetic layer (i.e. the spin polarization of the current) and I_0 is the amplitude of the injected microwave current of pulsation ω . The eq.A.1 is solved following the approach of Kisilev *et al.* [6]. We look for the harmonic response of the magnetization to the torque induced by a spin polarized current $\mathbf{I}_{SP}(\omega)$:

$$\mathbf{m}(t) = \overline{\overline{\chi}}_{\mathbf{I}_{SP}}(\omega) \mathbf{I}_{SP}(\omega, t) \quad (\text{A.2})$$

$$\mathbf{I}_{SP}(\omega, t) = I_0 e^{-i\omega t} \mathbf{p} \times \frac{\mathbf{M}_{eq}}{M_S}$$

$$\mathbf{M}(t) = \mathbf{M}_{eq} + \mathbf{m}(t)$$

with \mathbf{M}_{eq} we indicate the equilibrium component of the oscillating magnetization. The approximation of small angle precession ($|\mathbf{m}(t)| \ll |\mathbf{M}_{eq}|$) permits us to linearize the LLG equation and to deduce a general expression for the "current-susceptibility" $\overline{\overline{\chi}}_{\mathbf{I}_{SP}}$. In the calculation of the free energy we consider the contributions of an external static field \mathbf{H}_0 and of the magnetostatic energy.

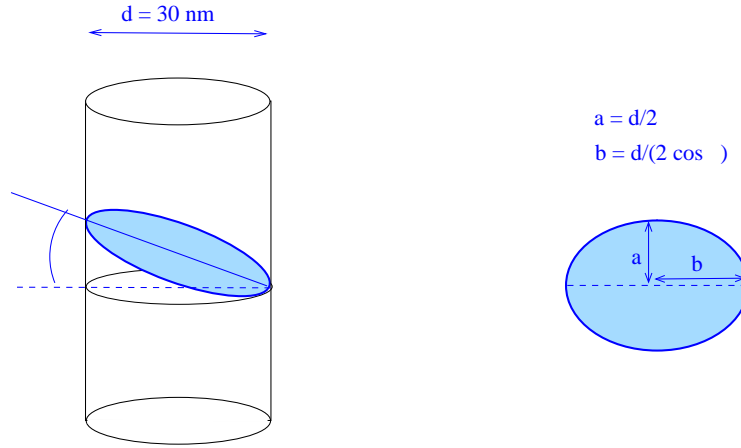


Figure A.1 – Orientation of the magnetic layers in the pore. The possible angle ψ implies the in-plane ellipticity of the magnetic layers. This ellipticity determines the value of the demagnetizing factor.

Shape of the magnetic layers and coordinate system

The magnetic layers in our samples are cylindrical elements embedded in Cu nanowires. These layers can deviate from the perpendicular to the pore axis, as shown in fig.A.1. The angle of inclination ψ has a maximum value of 30° degrees and determines a slight ellipticity of the layers. In the calculation of the LLG equation we consider magnetic elements of ellipsoidal shape of slight in-plane ellipticity, which can be considered a good approximation of the magnetic layers of our nanostructures. The demagnetizing tensor in the coordinate system $O_{x_0y_0z_0}$ parallel to the axes of the ellipsoid is of the form:

$$\overline{\overline{N}} = \begin{pmatrix} N_x^d & 0 & 0 \\ 0 & N_y^d & 0 \\ 0 & 0 & N_z^d \end{pmatrix} \quad (\text{A.3})$$

$$N_y^d < N_x^d < N_z^d$$

For the analytical solution of the LLG modified equation it is convenient to chose a coordinate system with one axis parallel to the equilibrium position of the oscillating magnetization, as shown in fig.A.2.

In this system of coordinate the demagnetizing tensor becomes:

$$\overline{\overline{N}}_d = \begin{pmatrix} N_x^d & 0 & 0 \\ 0 & N_y^d & 0 \\ 0 & 0 & N_z^d \end{pmatrix} \xrightarrow{R_{x'}(\theta) R_z(\varphi)} \begin{pmatrix} N_x & N_{xy} & N_{yz} \\ N_{xy} & N_y & N_{yz} \\ N_{xz} & N_{yz} & N_z \end{pmatrix} \quad (\text{A.4})$$

$$\begin{aligned} N_x &= N_x^d \cos^2 \varphi + N_y^d \sin^2 \varphi \\ N_y &= \left(N_x^d \sin^2 \varphi + N_y^d \cos^2 \varphi \right) \cos^2 \theta + N_z^d \sin^2 \theta \\ N_z &= \left(N_x^d \sin^2 \varphi + N_y^d \cos^2 \varphi \right) \sin^2 \theta + N_z^d \cos^2 \theta \\ N_{xy} &= \left(N_x^d - N_y^d \right) \sin \varphi \cos \varphi \cos \theta \end{aligned}$$

where θ and ϕ identify the equilibrium direction of $\mathbf{M}(t)$ in the system of coordinates $O_{x_0 y_0 z_0}$, as depicted in fig.A.2. We gave the analytical expression of the N_{ij} elements which will enter in our calculation.

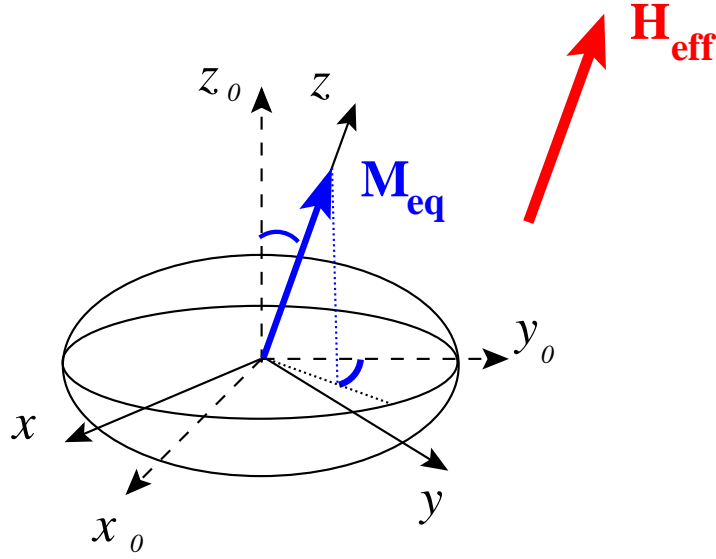


Figure A.2 – Coordinate system adopted for the analytical solution of LLG equation in presence of STT. The system of coordinates $O_{x_0 y_0 z_0}$ is oriented parallel to the axes of the ellipsoidal layer. The new frame O_{xyz} is fixed with the \hat{z} axis along the equilibrium position of the precessing magnetization ($\hat{z} \parallel \mathbf{M}_{eq} \parallel \mathbf{H}_{eq}$).

Temporal evolution of $\mathbf{M}(t)$

The expression of the tensor $\overline{\overline{\chi}}_{\mathbf{I}_{SP}}(\omega)$ is deduced by the linearization of eq.A.1. We consider an arbitrary orientation of the external field \mathbf{H}_0 . We obtain:

$$\overline{\overline{\chi}}_{\mathbf{I}_{SP}}(\omega) = \frac{\beta \mathcal{P}}{\omega_{res}^2 - \omega^2} \begin{pmatrix} \omega_y - i\alpha\omega & i\omega - \omega_m \\ -i\omega - \omega_m & \omega_x - i\alpha\omega \end{pmatrix} \quad (\text{A.5})$$

$$\beta = \frac{\gamma \hbar}{2eV_m M_S}$$

$$\omega_m = -\mu_0 \gamma M_s N_{xy}$$

$$\omega_{x,y} = -\mu_0 \gamma M_S \left(\frac{H_0^{(z)}}{M_S} - N_z + N_{x,y} \right)$$

$$\omega_{res} = \sqrt{(\omega_x - i\alpha\omega)(\omega_y - i\alpha\omega) - \omega_m^2}$$

with $H_0^{(z)}$ we indicate the projection of the external magnetic field on \hat{z} , i.e. the direction of the effective field. By inserting eq.A.5 in A.2 we deduce the temporal evolution of the magnetization:

$$m_x(t) = \beta \mathcal{P} I_0 e^{-i\omega t} \sin \theta_m \frac{\cos \phi_m (\omega_y - i\alpha\omega) + \sin \phi_m (\omega_m - i\omega)}{\omega_{res}^2 - \omega^2} \quad (\text{A.6})$$

$$m_y(t) = \beta \mathcal{P} I_0 e^{-i\omega t} \sin \theta_m \frac{-\sin \phi_m (\omega_x - i\alpha\omega) - \cos \phi_m (\omega_m - i\omega)}{\omega_{res}^2 - \omega^2} \quad (\text{A.7})$$

where the angle θ_m and φ_m identify the direction of the polarization vector \mathbf{p} and are defined as depicted in fig.3.3 on page53.

Bibliography

- [1] C. Chappert, A. Fert, and F. N. Van Dau, *The emergence of spin electronics in data storage*, Nat. Mater. **6**, 813 (2007). 1, 2, 19
- [2] M. Pannetier, C. Fermon, G. Le Goff, J. Simola, and E. Kerr, *Femtotesla Magnetic Field Measurement with Magnetoresistive Sensors*, Science **304**, 1648 (2004). 1, 2
- [3] J. Slonczewski, *Current-driven excitation of magnetic multilayers*, J. Magn. Magn. Mater. **159**, L1 (1996). 2, 20
- [4] L. Berger, *Emission of spin waves by a magnetic multilayer traversed by a current*, Phys. Rev. B **54**, 9353 (1996). 2, 20
- [5] S. S. P. Parkin, M. Hayashi, and L. Thomas, *Magnetic Domain-Wall Racetrack Memory*, Science **320**, 190 (2008). 2
- [6] S. I. Kiselev, J. C. Sankey, I. N. Krivorotov, N. C. Emley, R. J. Schoelkopf, R. A. Buhrman, and D. C. Ralph, *Microwave oscillations of a nanomagnet driven by a spin-polarized current*, Nature **425**, 380 (2003). 2, 25, 26, 27, 109
- [7] A. D. Kent, *Spintronics: A nanomagnet oscillator*, Nat. Mater **6**, 399 (2007). 2
- [8] R. P. Cowburn, *Property variation with shape in magnetic nanoelements*, J. Phys. D **33**, R1 (2000). 3
- [9] T. M. Crawford, M. Covington, and G. J. Parker, *Time-domain excitation of quantized magnetostatic spin-wave modes in patterned NiFe thin film ensembles*, Phys. Rev. B **67**, 024411 (2003). 3
- [10] K. Y. Guslienko and A. N. Slavin, *Boundary conditions for magnetization in magnetic nanoelements*, Phys. Rev. B **72**, 014463 (2005). 3, 13, 72
- [11] S. O. Demokritov, *Spin wave confinement* (Pan Stanford Publishing, 2009). 3, 12, 13

-
- [12] G. Gubbiotti, M. Kostylev, N. Sergeeva, M. Conti, G. Carlotti, T. Ono, A. N. Slavin, and A. Stashkevich, *Brillouin light scattering investigation of magnetostatic modes in symmetric and asymmetric NiFe/Cu/NiFe trilayered wires*, Phys. Rev. B **70**, 224422 (2004). 3, 47
- [13] J. Jorzick, S. O. Demokritov, B. Hillebrands, M. Bailleul, C. Fermon, K. Y. Guslienko, A. N. Slavin, D. V. Berkov, and N. L. Gorn, *Spin Wave Wells in Nonellipsoidal Micrometer Size Magnetic Elements*, Phys. Rev. Lett. **88**, 047204 (2002). 3, 47
- [14] N. Smith and P. Arnett, *White-noise magnetization fluctuations in magnetoresistive heads*, Appl. Phys. Lett. **78**, 1448 (2001). 3
- [15] J.-G. Zhu, *Thermal magnetic noise and spectra in spin valve heads*, J. Appl. Phys. **91**, 7273 (2002). 3
- [16] K. Y. Guslienko, R. W. Chantrell, and A. N. Slavin, *Dipolar localization of quantized spin-wave modes in thin rectangular magnetic elements*, Phys. Rev. B **68**, 024422 (2003). 3
- [17] S. O. Demokritov, B. Hillebrands, and A. Slavin, *Brillouin light scattering studies of confined spin waves: linear and non linear confinement*, Phys. Rep. **348**, 441 (2001). 3, 13
- [18] R. D. McMichael and M. D. Stiles, *Magnetic normal modes of nanoelements*, J. Appl. Phys. **97**, 10J901 (2005). 3, 15, 16, 74
- [19] D. D. Stancil and A. Prabhakar, *Spin Waves: Theory and Applications* (Springer, 2009). 4, 10
- [20] L. Landau and E. Lifshitz, *On the theory of the dispersion of magnetic permeability in ferromagnetic bodies*, Phys. Zeitsch. der Sow. **8**, 153 (1935). 6
- [21] A. G. Gurevich and G. A. Melkov, *Magnetization Oscillations and Waves* (CRC Press, 1996). 7
- [22] J. A. Osborn, *Demagnetizing factors of the general ellipsoid*, Phys. Rev. **67**, 351 (1945). 10, 54, 68
- [23] D. D. Stancil, *Theory of Magnetostatic Waves* (Springer-Verlag, 1993). 11
- [24] L. R. Walker, *Magnetostatic modes in ferromagnetic resonance*, Phys. Rev. **105**, 390 (1957). 11
- [25] J. Jorzick, S. O. Demokritov, B. Hillebrands, M. Bailleul, C. Fermon, K. Y. Guslienko, A. N. Slavin, D. V. Berkov, and N. L. Gorn, *Spin wave wells in nonellipsoidal micrometer size magnetic elements*, Phys. Rev. Lett. **88**, 047204 (2002). 13

-
- [26] C. Bayer, S. O. Demokritov, B. Hillebrands, and A. N. Slavin, *Spin-wave wells with multiple states created in small magnetic elements*, Appl. Phys. Lett. **82**, 607 (2003). 13
- [27] B. B. Maranville, R. D. McMichael, S. A. Kim, W. L. Johnson, C. A. Ross, and J. Y. Cheng, *Characterization of magnetic properties at edges by edge-mode dynamics*, J. Appl. Phys. **99**, 08C703 (2006). 13
- [28] A. Slavin and V. Tiberkevich, *Spin wave mode excited by spin-polarized current in a magnetic nanocontact is a standing self-localized wave bullet*, Phys. Rev. Lett. **95**, 237201 (2005). 13
- [29] B. Hillebrands and K. Ounadjela, eds., *Spin dynamics in confined magnetic structures I* (Springer, 2002). 13, 84
- [30] L. D. Buda, I. L. Prejbeanu, U. Ebels, and K. Ounadjela, *Investigation of 3D micro-magnetic configurations in circular nanoelements*, J. Magn. Magn. Mater. **242**, 996 (2002). 14, 58
- [31] N. F. Mott, *The electrical conductivity of transition metals*, Proc. R. Soc. **153**, 699 (1936). 16
- [32] V. L. Moruzzi, J. F. Janak, and A. R. Williams, *Calculated electronic properties of metals* (Pergamon Press, New York, 1978). 17
- [33] M. N. Baibich, J. M. Broto, A. Fert, F. N. Van Dau, F. Petroff, P. Etienne, G. Creuzet, A. Friederich, and J. Chazelas, *Giant Magnetoresistance of (001)Fe/(001)Cr Magnetic Superlattices*, Phys. Rev. Lett. **61**, 2472 (1988). 22
- [34] G. Binasch, P. Grünberg, F. Saurenbach, and W. Zinn, *Enhanced magnetoresistance in layered magnetic structures with antiferromagnetic interlayer exchange*, Phys. Rev. B **39**, 4828 (1989). 22
- [35] M. Tsoi, A. G. M. Jansen, J. Bass, W.-C. Chiang, M. Seck, V. Tsoi, and P. Wyder, *Excitation of a Magnetic Multilayer by an Electric Current*, Phys. Rev. Lett. **80**, 4281 (1998). 23, 24, 27, 58
- [36] J. A. Katine, F. J. Albert, R. A. Buhrman, E. B. Myers, and D. C. Ralph, *Current-Driven Magnetization Reversal and Spin-Wave Excitations in Co /Cu /Co Pillars*, Phys. Rev. Lett. **84**, 3149 (2000). 24, 41, 43
- [37] J. Grollier, V. Cros, A. Hamzic, J. M. George, H. Jaffrès, A. Fert, G. Faini, J. B. Youssef, and H. Legall, *Spin-polarized current induced switching in Co/Cu/Co pillars*, Appl. Phys. Lett. **78**, 3663 (2001). 24

-
- [38] M. Tsoi, V. Tsoi, J. Bass, A. G. M. Jansen, and P. Wyder, *Current-driven resonances in magnetic multilayers*, Phys. Rev. Lett. **89**, 246803 (2002). 25
- [39] W. H. Rippard, M. R. Pufall, S. Kaka, S. E. Russek, and T. J. Silva, *Direct-Current Induced Dynamics in $Co_{90}Fe_{10}/Ni_{80}Fe_{20}$ Point Contacts*, Phys. Rev. Lett. **92**, 027201 (2004). 26
- [40] D. Houssameddine, U. Ebels, B. Delaët, B. Rodmacq, I. Firastrau, F. Ponthenier, M. Brunet, C. Thirion, J.-P. Michel, L. Prejbeanu-Buda, M.-C. Cyrille, O. Redon, B. Dieny, *Spin-torque oscillator using a perpendicular polarizer and a planar free layer*, Nat. Mater. **6**, 447 (2007). 27
- [41] A. A. Tulapurkar, Y. Suzuki, A. Fukushima, H. Kubota, H. Maehara, K. Tsunekawa, D. D. Djayaprawira, N. Watanabe, and S. Yuasa, *Spin-torque diode effect in magnetic tunnel junctions*, Nature **438**, 339 (2005). 27, 45
- [42] T. Devolder, C. Chappert, J. A. Katine, M. J. Carey, and K. Ito, *Distribution of the magnetization reversal duration in subnanosecond spin-transfer switching*, Phys. Rev. B **75**, 064402 (2007). 27, 84
- [43] L. Piraux, K. Renard, R. Guillemet, S. Matefi-Tempfli, M. Matefi-Tempfli, V. A. Antohé, S. Fusil, K. Bouzehouane, and V. Cros, *Template-Grown NiFe/Cu/NiFe Nanowires for Spin Transfer Devices*, Nano Letters **7**, 2563 (2007). 27
- [44] E. Murè, N. Biziere, and J.-P. Ansermet, *Lithography-free study of spin torque*, J. Magn. Magn. Mat. doi:10.1016/j.jmmm.2009.05.012 (2009). 27, 43
- [45] J. Meier, B. Doudin, and J.-P. Ansermet, *Magnetic properties of nanosized wires*, J. Appl. Phys. **79**, 6010 (1996). 28
- [46] L. G. T. Ohgai, X. Hoffer and J.-P. Ansermet, *Electrochemical Surface Modification of Aluminium Sheets for Application to Nano-electronic Devices: Anodization Aluminium and Electrodeposition of Cobalt-Copper*, J. Appl. Electrochem. **34**, 1007 (2004). 28
- [47] W. Schwarzacher and D. Lashmore, *Giant magnetoresistance in electrodeposited films*, IEEE Trans. Magn. **32**, 3133 (1996). 29
- [48] B. Doudin, J. Wegrowe, S. Gilbert, V. Scarani, D. Kelly, J. Meier, and J.-P. Ansermet, *Magnetic and transport properties of electrodeposited nanostructured nanowires*, IEEE Trans. Magn. **34**, 968 (1998). 29
- [49] R. Ferré, K. Ounadjela, J. M. George, L. Piraux, and S. Dubois, *Magnetization processes in nickel and cobalt electrodeposited nanowires*, Phys. Rev. B **56**, 14066 (1997). 29

-
- [50] V. Scarani, B. Doudin, and J.-P. Ansermet, *The microstructure of electrodeposited cobalt-based nanowires and its effect on their magnetic and transport properties*, J. Magn. Mater. **205**, 241 (1999). 29
- [51] A. Rudolf, *Search for Nuclear Magnetic Resonance Evidence of Spin Accumulation*, Ph.D. thesis, EPFL (2009). 30, 31
- [52] P. Corp., livermore, CA 94550-9520. 31
- [53] D. Kelly, *Direct action of electric currents on the magnetization of nanometer sized electrodeposited wires*, Ph.D. thesis, EPFL (2001). 36
- [54] W. Wernsdorfer, E. B. Orozco, K. Hasselbach, A. Benoit, B. Barbara, N. Demoncy, A. Loiseau, H. Pascard, and D. Mailly, *Experimental Evidence of the Néel-Brown Model of Magnetization Reversal*, Phys. Rev. Lett. **78**, 1791 (1997). 40, 42, 87
- [55] J. C. Sankey, P. M. Braganca, A. G. F. Garcia, I. N. Krivorotov, R. A. Buhrman, and D. C. Ralph, *Spin-Transfer-Driven Ferromagnetic Resonance of Individual Nanomagnets*, Phys. Rev. Lett. **96**, 227601 (2006). 45
- [56] G. D. Fuchs, J. C. Sankey, V. S. Pribiag, L. Qian, P. M. Braganca, A. G. F. Garcia, E. M. Ryan, Z.-P. Li, O. Ozatay, D. C. Ralph, R. A. Buhrman, *Spin-torque ferromagnetic resonance measurements of damping in nanomagnets*, Appl. Phys. Lett. **91**, 062507 (2007). 45
- [57] W. Chen, J.-M. L. Beaujour, G. de Loubens, A. D. Kent, and J. Z. Sun, *Spin-torque driven ferromagnetic resonance of Co/Ni synthetic layers in spin valves*, Appl. Phys. Lett. **92**, 012507 (2008). 45
- [58] Z. Zhang, P. C. Hammel, and P. E. Wigen, *Observation of ferromagnetic resonance in a microscopic sample using magnetic resonance force microscopy*, Appl. Phys. Lett. **68**, 2005 (1996). 47
- [59] M. M. Midzor, P. E. Wigen, D. Pelekhov, W. Chen, P. C. Hammel, and M. L. Roukes, *Imaging mechanisms of force detected FMR microscopy*, J. Appl. Phys. **87**, 6493 (2000). 47
- [60] G. de Loubens, V. V. Naletov, O. Klein, J. B. Youssef, F. Boust, and N. Vukadinovic, *Magnetic Resonance Studies of the Fundamental Spin-Wave Modes in Individual Sub-micron Cu/NiFe/Cu Perpendicularly Magnetized Disks*, Phys. Rev. Lett. **98**, 127601 (2007). 47
- [61] R. Meckenstock, D. Spoddig, D. Dietzel, J. Pelzl, and J. P. Bucher, *Scanning thermal microwave resonance microscopy of Ni nanodots*, Rev. Sci. Instrum. **74**, 789 (2003). 47

-
- [62] V. E. Demidov, S. O. Demokritov, B. Hillebrands, M. Laufenberg, and P. P. Freitas, *Radiation of spin waves by a single micrometer-sized magnetic element*, Appl. Phys. Lett. **85**, 2866 (2004). 47
- [63] C. Bayer, J. Jorzick, B. Hillebrands, S. O. Demokritov, R. Kouba, R. Bozinoski, A. N. Slavin, K. Y. Guslienko, D. V. Berkov, N. L. Gorn, M. P. Kostylev, *Spin-wave excitations in finite rectangular elements of $Ni_{80}Fe_{20}$* , Phys. Rev. B **72**, 064427 (2005). 47
- [64] K. Perzlmaier, M. Buess, C. H. Back, V. E. Demidov, B. Hillebrands, and S. O. Demokritov, *Spin-Wave Eigenmodes of Permalloy Squares with a Closure Domain Structure*, Phys. Rev. Lett. **94**, 057202 (2005). 47
- [65] W. K. Hiebert, G. E. Ballentine, L. Lagae, R. W. Hunt, and M. R. Freeman, *Ultrafast imaging of incoherent rotation magnetic switching with experimental and numerical micromagnetic dynamics*, J. Appl. Phys. **92**, 392 (2002). 48
- [66] S. Tamaru, J. A. Bain, R. J. M. van de Veerdonk, T. M. Crawford, M. Covington, and M. H. Kryder, *Imaging of quantized magnetostatic modes using spatially resolved ferromagnetic resonance*, J. Appl. Phys. **91**, 8034 (2002). 48
- [67] R. Meckenstock, M. Möller, and D. Spoddig, *Kerr detected time average of magnetization precession in ferromagnetic resonance*, Appl. Phys. Lett. **86**, 112506 (2005). 48
- [68] G. Gubbiotti, M. Madami, S. Tacchi, G. Carlotti, and T. Okuno, *Normal mode splitting in interacting arrays of cylindrical permalloy dots*, J. Appl. Phys. **99**, 08C701 (2006). 48
- [69] J. Jorzick, S. O. Demokritov, C. Mathieu, B. Hillebrands, B. Bartenlian, C. Chappert, F. Rousseaux, and A. N. Slavin, *Brillouin light scattering from quantized spin waves in micron-size magnetic wires*, Phys. Rev. B **60**, 15194 (1999). 48
- [70] G. Boero, S. Rusponi, P. Bencok, R. S. Popovic, H. Brune, and P. Gambardella, *X-ray ferromagnetic resonance spectroscopy*, Appl. Phys. Lett. **87**, 152503 (2005). 48
- [71] A. Puzic, B. V. Waeyenberge, K. W. Chou, P. Fischer, H. Stoll, G. Schütz, T. Tyliczszak, K. Rott, H. Brückl, G. Reiss, I. Neudecker, T. Haug, M. Buess, C. H. Back, *Spatially resolved ferromagnetic resonance: Imaging of ferromagnetic eigenmodes*, J. Appl. Phys. **97**, 10E704 (2005). 48
- [72] A. A. Kovalev, G. E. W. Bauer, and A. Brataas, *Current-driven ferromagnetic resonance, mechanical torques, and rotary motion in magnetic nanostructures*, Phys. Rev. B **75**, 014430 (2007). 49

-
- [73] S. Vonsovskii, *Ferromagnetic Resonance* (Pergamon Press., 1966). 67
- [74] F. Montoncello, L. Giovannini, F. Nizzoli, P. Vavassori, M. Grimsditch, T. Ono, G. Gubbiotti, S. Tacchi, and G. Carlotti, *Soft spin waves and magnetization reversal in elliptical Permalloy nanodots: Experiments and dynamical matrix results*, Phys. Rev. B **76**, 024426 (2007). 73
- [75] M. Carpentieri, G. Finocchio, B. Azzerboni, L. Torres, L. Lopez-Diaz, and E. Martinez, *Effect of the classical ampere field in micromagnetic computations of spin polarized current-driven magnetization processes*, J. Appl. Phys. **97**, 10C713 (2005). 75
- [76] Y. Zhou, J. Persson, and J. A. Kerman, *Intrinsic phase shift between a spin torque oscillator and an alternating current*, J. Appl. Phys. **101**, 09A510 (2007). 75
- [77] C. Thirion, W. Wernsdorfer, and D. Maily, *Switching of magnetization by nonlinear resonance studied in single nanoparticles*, Nat. Mater. **2**, 524 (2003). 79, 83, 84
- [78] N. Biziere, E. Murè, and J.-P. Ansermet, *Microwave spin-torque excitation in a template-synthesized nanomagnet*, Phys. Rev. B **79**, 012404 (2009). 80
- [79] G. Bertotti, I. D. Mayergoyz, C. Serpico, M. d'Aquino, and R. Bonin, *Nonlinear-dynamical-system approach to microwave-assisted magnetization dynamics (invited)*, J. Appl. Phys. **105**, 07B712 (2009). 83
- [80] G. Bertotti, C. Serpico, I. D. Mayergoyz, A. Magni, M. d'Aquino, and R. Bonin, *Magnetization switching and microwave oscillations in nanomagnets driven by spin-polarized currents*, Phys. Rev. Lett. **94**, 127206 (2005). 83
- [81] W. Scholz and S. Batra, *Micromagnetic modeling of ferromagnetic resonance assisted switching*, Journal of Applied Physics **103**, 07F539 (2008). 83
- [82] S. H. Florez, J. A. Katine, M. Carey, L. Folks, O. Ozatay, and B. D. Terris, *Effects of radio-frequency current on spin-transfer-torque-induced dynamics*, Phys. Rev. B **78**, 184403 (2008). 84, 85
- [83] Y.-T. Cui, J. C. Sankey, C. Wang, K. V. Thadani, Z.-P. Li, R. A. Buhrman, and D. C. Ralph, *Resonant spin-transfer-driven switching of magnetic devices assisted by microwave current pulses*, Phys. Rev. B **77**, 214440 (2008). 84, 85
- [84] J. Z. Sun, *Spin-current interaction with a monodomain magnetic body: A model study*, Phys. Rev. B **62**, 570 (2000). 84
- [85] I. N. Krivorotov, D. V. Berkov, N. L. Gorn, N. C. Emley, J. C. Sankey, D. C. Ralph, and R. A. Buhrman, *Large-amplitude coherent spin waves excited by spin-polarized current in nanoscale spin valves*, Phys. Rev. B **76**, 024418 (2007). 84

- [86] W. F. Brown, *Thermal fluctuations of a single-domain particle*, Phys. Rev. **130**, 1677 (1963). 87
- [87] A. Fabian, C. Terrier, S. Serrano Guisan, P. Guittienne, L. Gravier, and J.-P. Ansermet, *Current-induced magnetization switching in pseudo spin-valves*, J. Phys.: Condens. Matter **18**, 1569 (2006). 88
- [88] T. Devolder and C. Chappert, *Spectral analysis of the precessional switching of the magnetization in an isotropic thin film*, Solid State Communications **129**, 97 (2004). 98
- [89] C. Serpico, I. D. Mayergoyz, and G. Bertotti, *Analytical solutions of landau-lifshitz equation for precessional switching*, J. Appl. Phys. **93**, 6909 (2003). 98
- [90] I. Tudosa, C. Stamm, A. B. Kashuba, F. King, H. C. Siegmann, J. Stöhr, G. Ju, B. Lu, and D. Weller, *The ultimate speed of magnetic switching in granular recording media*, Nature **428**, 831 (2004). 99
- [91] A. Kashuba, *Domain instability during magnetization precession*, Phys. Rev. Lett. **96**, 047601 (2006). 99

Curriculum Vitae

Elena Murè

Ecole Polytechnique Fédérale de Lausanne
Institut de Physique de la Matière Condensée
CH - 1015 Lausanne, Suisse
Tel: +41 (0)21 69 34 510
elena.mure@epfl.ch

Personal information

Date of birth January 1st 1982
Nationality Italian

Languages

Italian: mother tongue
French: fluent written and oral
English: fluent written and oral

Education

2006-2010 PhD in Physics at *Ecole Polytechnique Fédérale de Lausanne*.
2005-2006 Internship of the Pisa University in "Optical multidiagnostic for the nanoparticulate study in gas flame combustion", at the *Research Area of ENEL, italian industry leader in energy production*, Pisa.
2003-2005 *Laurea specialistica*, in Physical Sciences, at *Università di Pisa*, Italy
200-2003 *Laurea* in Physics at *Università di Pisa*, Italy
2000 *Diploma*, Liceo Scientifico G. Marconi, Carrara (MS) Italy.

Schools

September 2009 "Spin transport and dynamics in nanostructures", XVI International Summer School, Madrid.

October 2008 "Physica in Low Dimensions", INFN School, Lucca

Conference presentations

Joint European Magnetic Symposia, 2008: "New technique for spin torque applications" E. Murè, N. Biziere, JPh. Ansermet. Poster presentation.

Intermag Europe 2008-International Magnetism Conference: *Electrically detected ferromagnetic resonance in electrodeposited spin valve under AC excitation* E. Murè, N. Biziere, JPh. Ansermet. Oral presentation.

Teaching Experience

Physique du Solide I: prof. H. Brune

Physique du Solide II: prof. H. Brune

Publications

(in chronological order)

In the frame of the PhD thesis:

- Switching field modulation of a nanomagnet by resonant microwave spin torque

N. Bizière, E. Murè, J-Ph. Ansermet

Submitted to Journal of Magnetism and Magnetic Materials

- Microwave spin-torque excitation in a template-synthesized nanomagnet

N. Bizière, E. Murè, J-Ph. Ansermet

Phys. Rev. B **79**, 012404 (2009)

- Lithography-free study of spin torque

E. Murè, N. Bizière, JPh. Ansermet, *J. Magn. Magn. Mater.* (2009), proceedings of the Joint European Magnetism Symposium 2008 doi:10.1016/j.jmmm.2009.05.012

- Current-driven, electrically-detected ferromagnetic resonance in electrodeposited spin valves

N. Bizière, E. Murè, J-Ph. Ansermet

J. Magn. Magn. Mater. proceedings of the Joint European Magnetism Symposium 2008, accepted.

Not related to the PhD thesis:

- Detection of a two-photon transition by stimulated emission: Amplification and circular birefringence

S.Sanguinetti, **E. Murè**, P.Minguzzi.

Phys. Rev. A **75**,023408 (2007)